To the Graduate Council:

I am submitting herewith a dissertation written by Joseph G. Kreke entitled "Muon-Pion Discrimination Using a Sampling Calorimeter and Discriminant Analysis Techniques." I have examined the final copy of this dissertation for form and content and recommend that it be accepted in partial fulfillment of the requirements for the degree of Doctor of Philosophy, with a major in Physics.

Felix E. Obenshain

Felix E. Obenshain, Major Professor

We have read this dissertation
and recommend its acceptance:

Sole P. Solem

Carrol Bingham

Lawrence F Miller

Glenn R Young

Accepted for the Council:

C W Minkel

Associate Vice Chancellor
and Dean of The Graduate School

Muon-Pion Discrimination Using a Sampling Calorimeter and Discriminant Analysis Techniques

A Dissertation

Presented for the

Doctor of Philosophy

Degree

The University of Tennessee, Knoxville

Joseph G. Kreke

May, 1996

DEDICATION

For Pat

ACKNOWLEDGMENTS

Throughout the course of this project, many persons helped me who deserve acknowledgment and thanks. My advisor, Professor Felix E. Obenshain, provided much support over the years and I am deeply indebted to him, not only for the support, but for the opportunity to study great things. He made this complex process of the Doctorate Degree transform from purely imaginary to truly real. And as I move on to other ventures, I must say I will truly miss him, his family, and his boat. Great thanks also go to Professor Soren P. Sorensen, who gave much support and frequent discussions of physics, life, and religion. Special thanks also go to Dr. Glenn R. Young, Deputy Project Director of the PHENIX Experiment, who found time to pull cables, design and build the trigger, and chase down the many problems with the DAQ System. Dr. Xiaochun He helped tremendously in making sure many aspects worked smoothly and spent many weeks of long days with me at run time. The experiment was a success because of him. Sal Marino and Dave Dayton, staff at the AGS at BNL, solved endless technical problems we faced and deserve great thanks. Drs. Hee Kim, Surender Saini and Terry Awes also deserve many thanks for their help in teaching me experimentation and computation. Others who helped at the experiment are Dr. Ken Read, ORNL; Dr. Walter Kehoe, BNL; Edward J. Howell and William Lee, from Georgia State University, and Dr. Earl W. Cornell, from Vanderbilt University.

Also deserving of recognition are my undergraduate teachers at Duquesne University, Dr. Shih Chi Chang, Fr. Clifford Hill, Mr. Reginald Ney, Mrs. Ann Deramo, and Dr. Ted Weisman, all of whom taught me the broad fundamentals of science. I would also like to thank Brother Clement Smith, a counselor of mine at Central Catholic High School in Pittsburgh, Pa. who helped launch my college studies.

I would also like to thank the Department of Energy, who provided funding for this project and for me under contract number DOE PE-FG05-87ER40361. Also, the staff at the Physics Division at ORNL and the Joint Institute for Heavy Ion Research deserve thanks for personal support by providing a room for me when I needed to commute long distances.

Also deserving of thanks and acknowledgment are my families: the Fedewas, the Balloughs and the Krekes. My wife's parents, Vernon and Beverly Fedewa provided much support over the last few years. Some of my long trips were possible only because Bev and Vern helped at home. The Balloughs were my family in childhood and were some of the most generous and loving persons I have known. Many of my early school records name me as "Joseph Ballough" which always made me proud because I love them dearly. The Krekes, from whom I was separated at childhood due to my mother's illness, deserve special recognition. Each and every one of them helped make me who I am and I am thankful to all of them. In particular, my father, Dr. Cornelius W. Kreke, always encouraged learning of all things, not just the physical sciences. Also, my sister Susan A. B. Kreke-Rumbaugh, deserves special recognition because of her support and love over the years. Fifteen years ago she predicted I would write a book.

Last, but certainly not least, I thank my wife, to whom I dedicate this book, my work, and my life. The last six months of work on this project have been especially difficult for her for many reasons but she has made it through still liking me, still happy, and due in mid-June.

ABSTRACT

The separation of muons from pions in the momentum range of 1-9GeV/c poses a difficult technical problem when large areas of acceptance are required because of their similarity in mass. Through the use of a sampling calorimeter with uniformly distributed cell sizes, and discriminant analysis techniques, we show that separation can be achieved using their different natures (hadronic versus leptonic) to a level of about 2% at 2GeV/c when a real muon acceptance level of 97% is required. Separation is better at higher momenta (1%) and worse at lower momenta (10%) for the same real muon acceptance level. In addition, minimum segmentation requirements are reported for necessary levels of separation in the forthcoming PHENIX Experiment.

Preface

In the quest to understand physical nature, man uses tools to help him test theories of how certain event sequences occur. This is the basic technique of science and without advancing technology we risk limiting our understanding of nature. In the natural sciences, particularly physics, tools are constantly being invented and optimized to match the demands of frontier research. For instance, in the late 1970s, S. Van der Meer invented the $\bar{p}$ storage ring for the UA1 detector in the CERN $p\bar{p}$ collider experiment to assist in the production and detection of W and Z particles whose existence confirms the unification theory of the electromagnetic and weak forces. Also, the Hubble Space Telescope is indeed the epitome of the optimization of a tool. Already several important discoveries have been made with the HST, such as the recent confirmation of a Brown Dwarf. Naturally with large projects, such as the HST and the UA1 detector, come much development work for each of the detector subsystems. Each component must be precisely designed and rigorously tested, often requiring years of study of prototypes. This thesis reports the results of research and development (R&D) work done for the Muon Arm subdetector of the PHENIX Experiment, which is presently under construction at the Relativistic Heavy Ion Collider (RHIC), also under construction, at Brookhaven National Laboratory (BNL).

The project that this thesis discusses, denoted RD94, involves measuring the response of a prototype detector, the Muon Identifier (MuID), when particles of known type and energy strike it and using that information to distinguish two specific particle types, muons and pions. The prototype detector is based on an energy measuring device called a sampling calorimeter, yet its primary function is distinguishing these two particles, based not so much on the energy that each may deposit, but on other characteristics unique to each. The project can be classified somewhere between a low and a high energy particle physics experiment since the energy range studied, specifically 1-9GeV, is somewhat high for a low energy experiment and low for a high energy experiment. Low energy physics experiments rarely go much higher than about one GeV and high energy experiments are typically in the tens or hundreds of GeV. This "intermediate" energy range makes the project unique.

Chapter 1 discusses the basic physics background and motivations for such a project. Chapter 2 discusses all aspects of the RD94 Experiment, including goals, detector physics, and experimental layout, design, and operation. Chapter 3 discusses the data analysis, concentrating mainly on the discriminant analysis technique used to separate muons and pions, including the resultant muon-pion separation efficiency curves. Chapter 4 is a discussion of how well the project's goals were met with a few concluding remarks.

Contents

List of Tables

List of Figures

Chapter 1

Introduction

1.1 Overview of High Energy Nucleus-Nucleus Collisions

1.1.1 High Energy Physics

Historical Perspective

The field of high energy physics is said to have begun with the study of cosmic rays, high energy nuclei ranging from protons to uranium that permeate the galaxy[Perkins]. At sea level what is most often detected are secondary particles, those that emanate from collisions of the primary cosmic nuclei with the earth's atmosphere. Extremely high energy cosmics have been detected (on the order of 10^{12}GeV) but these are rare. Cosmic secondaries have a mean energy of about 2GeV at the surface of the earth and are most often muons and protons[PDG92]. The most significant discoveries made with cosmics were the positron in 1933 and the muon in 1937. The positron was postulated by Dirac several years beforehand as a negative energy solution to the relativistic quantum mechanical wave equation that bears his name. A positive confirmation of

Dirac's equation ushered in wide-spread acceptance of a new model for electromagnetic phenomena called Quantum Electrodynamics (QED). The discovery of the muon brought to the forefront Yukawa's postulate of linking the finite range of the nuclear force to the existence of a force carrier to account for the interaction between protons and neutrons. Although the muon did not fit the requirements of Yukawa's postulate (reacted too weakly with nuclear matter and lived too long[Dodd]), its discovery made Yukawa's idea of a mediating force carrier a fundamental concept in quantum field theory.

With the discovery of the neutron in 1932, it soon became obvious that some new force of nature must exist, strong enough to hold the nucleus together against the intense coulomb repulsion of protons. This force became known as the strong nuclear force and particles that reacted by it were known as *hadrons* (Greek for "strong"). The subsequent observance of spontaneous neutron decay lead to the discovery of yet another new force in nature. Since the free neutron decays after many minutes to a proton and an electron (β-decay), it was clear that neither the strong nuclear nor the electromagnetic forces could be responsible for the decay. The new force was termed the weak nuclear force and was assumed to be responsible for not only particle decay, but for the very weak reactions such as the reaction between muons and nuclei. Particles that did not react by the strong force (i.e. electrons, muons, light) were labeled *leptons* (Greek for "weak").

New particles continued to be discovered with the study of cosmic rays throughout the 1940s and 50s. Construction of machines, such as BNL's Cosmotron, soon began with the purpose to, in a sense, create cosmic rays in the laboratory; protons were accelerated and then directed toward a target to produce as violent a collision as possible. The particle energies could then be controlled and measurements of collision secondaries could be made in shorter periods with much higher statistics than previously possible.

Hadrons and The Quark Model

What perplexed physicists was that little sense could be made from the plethora of particles, or resonances, being discovered, all seemingly more elemental than the "elements". No broad pattern emerged that ordered the particles and pointed to missing pieces. Particles appeared to come in multiplets, such as the pion triplet: π^+, π^0, and π^-, but this sort of classification fell far short of a comprehensive scheme. The hope was to arrange the particles according to their properties just as Mendeleeff's periodic table ordered the chemical elements in columns and rows and left blanks where new, undiscovered elements should be. With literally scores of particles being found, some heavier than nucleons, it was felt that an even more fundamental group of particles should exist. In 1964, Gell-Mann and Zweig independently suggested that a group of three entities may account for all of the *hadronic* resonances known at the time. Gell-Mann named the entities *quarks* collectively, and *up*, *down*, and *strange* individually. The new quantum mechanical feature of these sub-nuclear particles was called *flavor*. The masses of the u and d quarks are approximately equal (about 5 and 10 MeV/c^2, respectively) and so they form a symmetric group, designated SU(2)[1] in group theory notation. The discovery of the s quark extends the symmetry to SU(3) even though it has a significantly heavier mass (approximately 150MeV/c^2).

Even though the group is not perfectly symmetric because the masses are unequal, the quarks could be combined in threes to derive baryons or in twos (particle-antiparticle pairs) to derive mesons. Predictions from this quark model were soon confirmed (Ω^-, and K^0_{long}[Adair87]) and with the discovery of more and heavier res-

[1]Special Unitary Representation of 2 objects.

Table 1.1: The Quarks.

Flavor	Charge(e)	Mass(MeV/c^2)
up(u)	+2/3	2-8
down(d)	-1/3	5-15
strange(s)	-1/3	100-300
charm(c)	+2/3	1000-1600
bottom(b)	-1/3	4000-4500
top(t)	+2/3	160000-220000

onances, more quarks (see table 1.1[2]) were successfully assimilated into the theory. The model now comprises six quarks.

QCD and The Standard Model

The way in which quarks interact has been most successfully described by the extension of QED to a new field theory for hadrons. This field theory describes the coupling of quarks within a hadron and how hadrons stick together to form bound states, such as a nucleus. The strength and range of the coupling are radically dissimilar from QED coupling. The strong force is not observed between hadrons until they are practically touching, thus giving the force a range of about 10^{-15}m (or 1fm), about the radius of a single nucleon. Since the force binds protons as well as neutrons, it is both independent of charge and strong enough to overcome the intense electric repulsion of protons in close proximity.

Another radical difference in the strong and electromagnetic forces is based on two facts. First is violation of the Pauli exclusion principle. Given that an up quark, for instance, can combine by threes to form a hyperon resonance (Δ^{++}), violates

[2]The t quark was reported March 2, 1995 to have been seen in the D0 (190±30 GeV/c^2) and CDF (176±16GeV/c^2) Experiments at Fermilab.

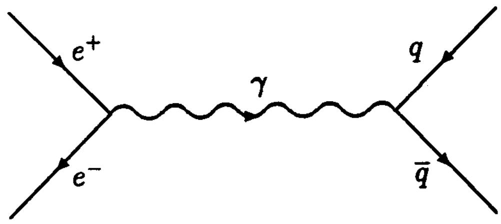

Figure 1-1: Feynman Diagram of Quark production from e^+e^- annihilation.

Pauli's exclusion principle since all three quarks have the same quantum numbers. The second fact comes from experiments of quark production from electron-positron annihilation (see figure 1-1) where hadron production was approximately 1/3 of that predicted. However, if we assume that the quarks have another quantum number, of which there are three possible values, we can account for both anomalies. This additional quantum mechanical property had the quality that when it came in certain groups of two or three it was not seen. By analogy, we can consider the pigments red, blue, and green which, when mixed in equal amounts, form white, which we can consider colorless. We may then imagine a second set of three anticolors which when mixed with their associated color, form white, or, again, colorlessness. The "new" quantum mechanical property appeared to work in a similar manner. It was neither seen in baryons (qqq), nor in mesons ($q\bar{q}$). Because of this analogous relationship with pigments, the field theory of hadrons was called Quantum Chromodynamics (QCD).

In addition, the strong force carriers, called gluons, in sharp contrast to the electromagnetic force carriers (photons), must come in eight varieties of color. The details of why there are eight instead of nine are consequences of the group theory of mixing color and anticolor so as to maintain colorlessness in the baryon. We assume that mesons are composed of two quarks with color and anticolor to, again, maintain the analogy with colorlessness.

The last significant contrast between the electromagnetic force and the hadronic force is its strength versus range. The electromagnetic potential is inversely proportional to distance and it extends to infinity.

$$V^{QED} = -\frac{\alpha_e}{r}$$

The QCD potential is similar in that it has the repulsive but it has a second intensely attractive term, similar to the spring potential.

$$V^{QCD} = -\frac{\alpha_s}{r} + kr.$$

The result is that the hadron is held together by the linear kr term. As two bound quarks begin to separate, the gluon field between them intensifies and forms a "flux tube". Farther separation means higher energy must be deposited which shows up in a more intense flux tube. When the flux tube reaches an energy threshold, high enough to form a $q\bar{q}$ pair, then the tube will break and the pair will form at the break site, with each of the newly formed quarks associating itself with one of the original quarks. Hence, new hadrons will form instead of releasing the quark. If a quark receives a very hard hit, jets of hadrons, primarily mesons, will shoot out of the reaction site. Hence, it appears that the quarks are eternally bound.

The Standard Model is the generally accepted mathematical formulation of our understanding of all known fundamental forces. Up until 1983, with the discovery of the $W^{\pm}$ and Z particles, we generally considered there to be four forces in nature. The discovery of the $W^{\pm}$ and Z lent credence to the Glashow-Weinberg-Salam model which unifies the electromagnetic and weak forces and is generally accepted today as the backbone of the Standard Model. The Model contains six quarks and six leptons that are grouped in three families, ordered primarily according to the quark masses

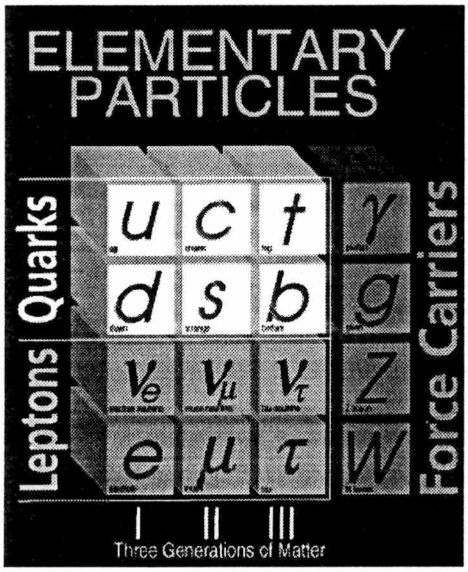

Figure 1-2: A diagram of the fundamental particles in the Standard Model[FNAL].

and known weak-decay relationships, along with 3 force carrier types, more commonly referred to as gauge bosons (see figure 1-2).

The first family of quarks and leptons, along with the γ force carrier constitute most all of the matter that we are commonly familiar with. The second family of massive particles can be seen in cosmic ray collisions of very high energy and the third family is generally seen only in experiments at high energy accelerators.

Although the discovery of the neutron led to questions of what holds the nucleus together, subsequent research led to the strong nuclear force and what binds hadrons, the force that holds the nucleons themselves together. The original query into what holds the nucleus together is still an active area of investigation. However, the force is assumed to be a residual effect of the strong force, much like the Van der Waals force is a residual effect of the electromagnetic force that holds molecules together[Guidry].

1.1.2 Nucleus-Nucleus Collisions

From the early Rutherford experiments of nudging gold nuclei with alpha particles to the more recent experiments at CERN where lead is blasted by lead, the study of nuclear phenomena is certainly broad. In 1973, W. Swiatecki[Swiatecki] attempted to classify all nuclear collisions according to total mass and center-of-mass energy (see figure 1-3) scheme where the energy scale was divided into four regimes: subsonic, supersonic, mesonic, and relativistic; and the mass was divided into two regimes: microscopic and macroscopic.

At subsonic energies, nuclei are just beginning to stick to each other and compression effects can be ignored. At supersonic energies, colliding nuclei produce shock waves through the nuclear matter ($0.2c$) and the compression can fracture the nucleus and, at the high end of the range, with high multiplicity. With higher energies,

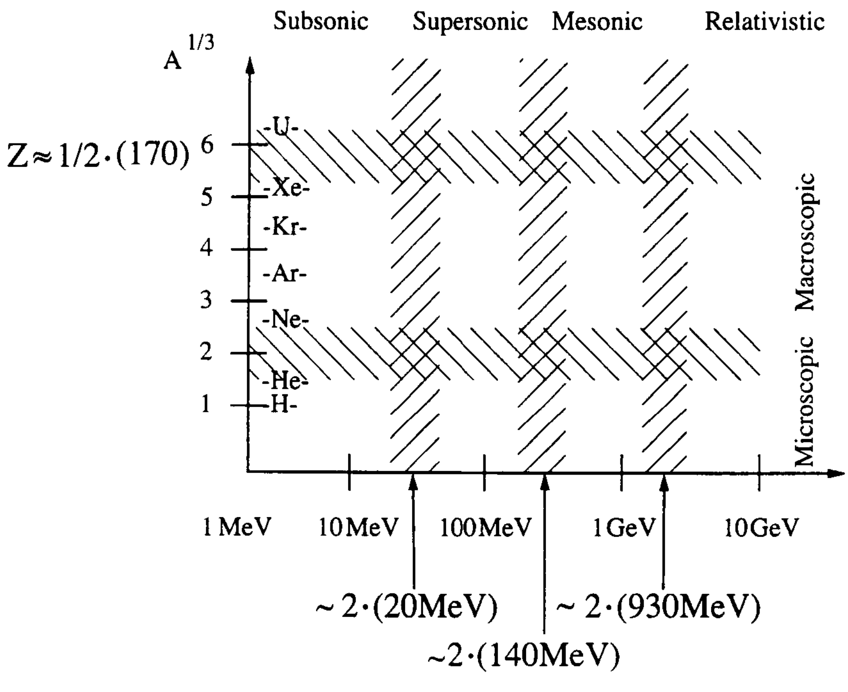

Figure 1-3: A classification scheme of NN collisions.

we move into the mesonic range where the collision is violent enough and nuclear densities are high enough that sub-nuclear processes begin to dominate, such as the production of mesons. The somewhat new area of study is the ultrarelativistic energy range where collisions are so violent, that the nucleons themselves begin to overlap and baryon densities reach many times that of cold nuclear matter.

1.1.3 Heavy Ion Physics

Motivations

In contrast to the bombardment of light particles (primarily H and He) at high energies to probe the inner structure of hadrons, heavy ion reactions deal with colliding nuclei, normally of 40amu or greater, to study the more global properties of large systems of nucleons. The dynamics of nucleon-nucleon (nn) collisions is well understood, as evidenced by the success of Monte Carlo codes, but extrapolating that understanding to heavier mass systems, such as nucleus-nucleus (NN) collisions, may not be adequate. Can we express heavy ion collisions as simply a large number of nucleon-nucleon collisions, or do heavy nuclei behave qualitatively different? Are there fundamental differences in large collections of nucleons from binary nucleon-nucleon systems? These collective effects include such items as transverse and longitudinal flow, transparency, and stopping power. It appears that collisions of heavy nuclei can be described in terms of many nucleon-nucleon collisions, but the complexities of colliding hundreds on hundreds of nucleons have so far prevented a clear description.

In addition to the study of collective effects, collisions of heavy ions provide us with the means to study phenomena such as high spin and angular momentum states; or high electromagnetic fields; or exploring the possibility of extending the periodic system[Greiner]. Heavy ion collisions also provide us with the only possible means of creating and studying super-dense material that may only exist at present in large celestial objects, such as neutron stars. Undoubtedly, the most significant aspect of the so-called collective effects of heavy ion collisions is the access to understanding the nuclear matter equation of state.

Because the nucleus is a large system of many objects, several of its characteristics can be described it terms of thermodynamics. The force that holds it together may be interpreted as pressure; the average motion of the nucleons with respect to one another may be expressed in terms of a temperature; and the nucleons themselves can be discussed as a condensates of some highly energetic system with a chemical potential.

Relativistic/Ultra-relativistic Energies

At very extreme temperature and energy density, conditions exist that are largely unexplored and may shed light on some of the fundamentals of physical nature. For instance, the Standard Model appears to be complete. It successfully predicted the existence of the t quark, whose recent discovery filled the last empty position on the chart (figure 1-2). But the next logical question to ask is are there any more empty places on the chart? or Are the number of families limited the three? Ultra-relativistic nuclear collisions may provide answers that either bolster or modify the Standard Model.

Also, the present standard cosmological theory poses that the universe exploded from a primordial big bang and several pieces of observational and computational data lend great credibility to it[Guidry]. Nuclear collisions at very high energies may extend the credibility by providing experimental evidence from creations of "little bangs" in a laboratory setting. Raising the energy essentially allows access to the study of earlier times in the development of the universe.

1.2 Quark-Gluon Plasma

1.2.1 Overview

In order to give the reader a broad base for the motivation of our experiment, RD94, we next discuss some of the basic physics that guides much of the pioneering work in the field of relativistic heavy ion collisions: the quark-gluon plasma. If the plasma can be formed, how can we make it? and What are the necessary conditions? Moreover, if the plasma does form, certain tell-tale signatures ought to manifest themselves. What are these signatures? and How can they be detected? and How will they differ from non-plasma conditions? An lastly, we anticipate that the plasma will form under very extreme temperature or energy density conditions where the particles released from the collision site will number in the tens of thousands, of which a significant fraction must be tracked and identified. How can this be done in the most efficient and cost-effective manner?

The remainder of this chapter discusses the basic physics of the QGP, the signatures by which it may be detected if it forms, and one of the experiments whose goal is to find it.

1.2.2 Physics

One of the most surprising and significant predictions of lattice QCD calculations is that at very high temperatures or energy densities, ordinary nuclear matter will dissolve into a quark-gluon plasma. In normal, or low temperature nuclear matter, nucleons have a radius of about 0.8fm and have a volume on the order of $2\mathrm{fm}^3$. The gluon field does not extend far beyond the quarks and attempts to release the quarks from the field have so far been futile. The quarks are said to be confined within the hadron. QCD predicts that if many hadrons could be compressed tightly enough that the quark constituents invade each other, then the quarks will effectively become deconfined within the macroscopic volume of the overlapping nuclei. The density needed for such a compression will be on the order of five to ten times that of normal nuclear matter according to QCD estimates. Figure 1-4 shows two large, equal-mass, nuclei just before and just after a high energy collision. Both nuclei are disk-like in the center-of-mass frame due to Lorentz contraction. The centrality of colliding nuclei can be categorized into central collisions, where the nuclei meet head-on, or peripheral collisions, where the nuclei hit each other off-center. The centrality of a particular collision can be determined after the collision by how much energy is emitted in the forward and transverse directions and can be quantified by an impact parameter which is basically the transverse distance between the two centers of the colliding nuclei. Figure 1-4 shows a very central collision. Very peripheral collisions send almost the full beam energy in the forward direction, while very central collisions send about half of the beam energy in the transverse direction (given equal mass nuclei)[Sorensen].

At the point in the collision when the nuclei are overlapped, the energy density might be high enough over the entire overlapping region of the nuclei that the nucleons dissolve into each other and form a plasma of quarks and gluons. The plasma begins to expand and cool, most rapidly in the forward directions where the expansion is aided by the large forward momentum of the nucleon constituents.

To create a QGP, we then must have conditions of very high energy density or very high temperature. The equation of state suggested by QCD shows that the critical temperature is reached at about 150MeV and the critical density is reached at about 5-10 times that of normal nuclear matter (see figure 1-5). These conditions do not normally exist on Earth, or in our solar system, or even in most solar systems, but it is suggested that it may be the state of matter at the core of neutron stars where the density may be sufficiently high if the temperature is not. Also, it has been

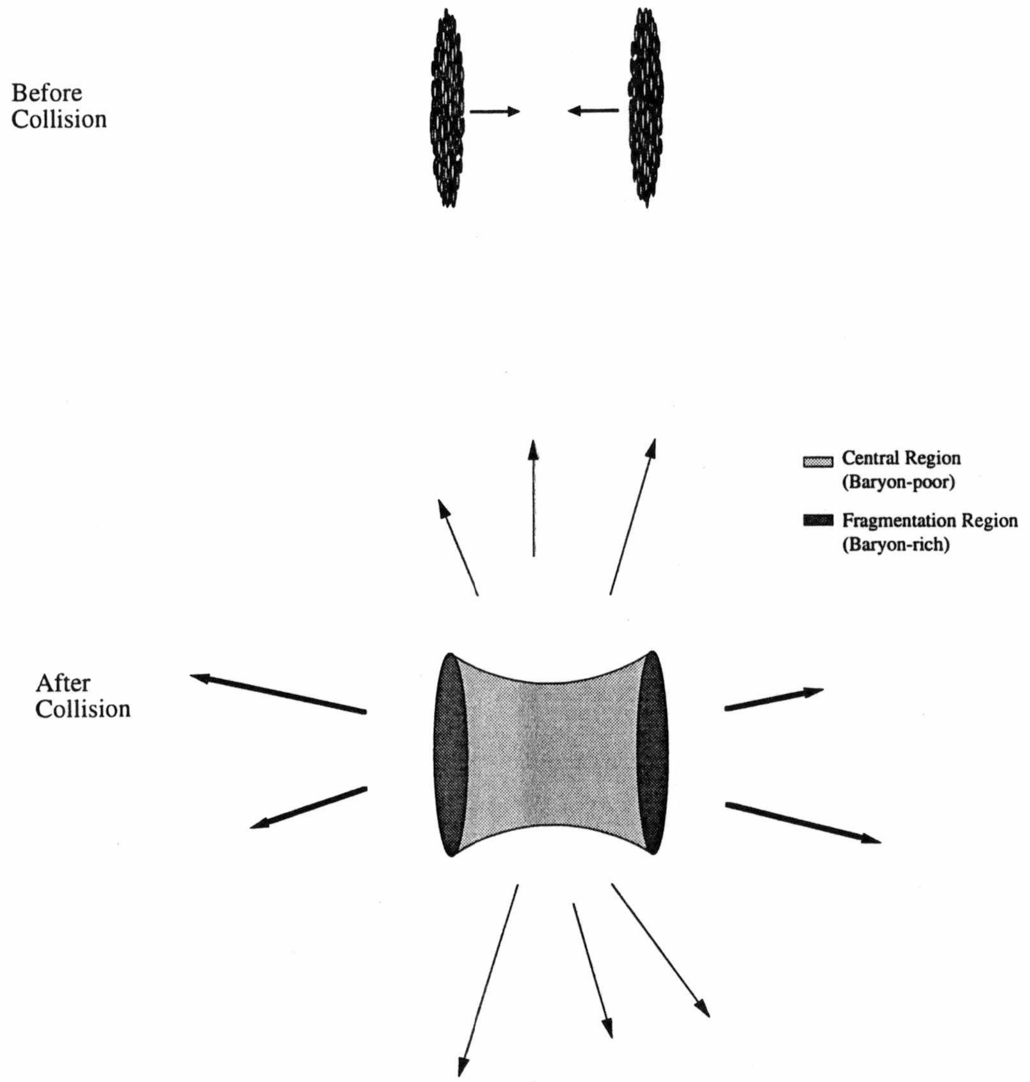

Figure 1-4: Heavy ions before and after a high energy collision where a quark-gluon plasma forms.

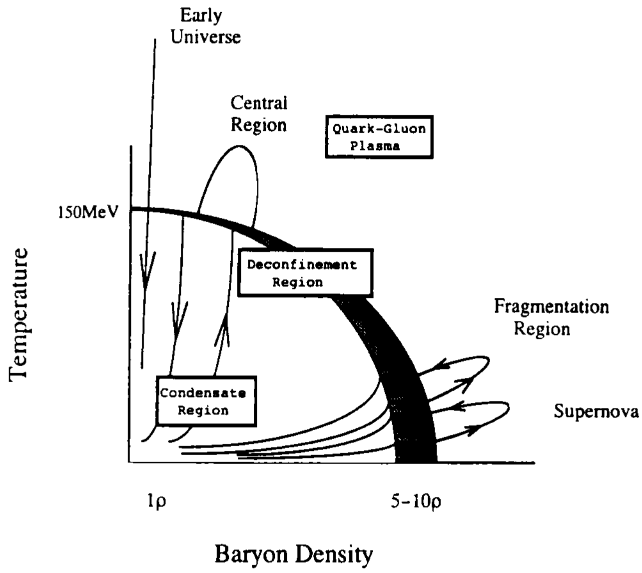

Figure 1-5: Temperature vs. Baryon Density.

proposed that the universe existed as a plasma of quarks and gluons very early in its development ($\approx 10^{-6}$s) after the Big Bang. We may soon, here on earth, have the capability to create these conditions at a new particle accelerator/collider called the Relativistic Heavy Ion Collider (RHIC).

RHIC is presently scheduled to come on-line in the third quarter of 1999[Thomas95] and provide up to 100AGeV counter-circulating ion beams, from protons to gold, yielding center-of-mass energies up to 200AGeV. Its primary purpose is to provide the conditions necessary to create a QGP, given current estimates, by colliding heavy nuclei at very high, ultrarelativistic, energies. Nucleons individually account for about a third of the volume in a nucleus. When collision energies are high enough to squeeze the nucleons to three times the normal density, we begin to see reactions that proceed via the strong force. It is estimated that the QGP forms at between five and ten times the normal nuclear density. At CERN energy densities, about twenty times the normal nuclear density is achieved[Nagamiya] and recent results from S-W collisions[HEIOS3] indicate that a QGP may be forming but the results are not definitive[Tserruya]. RHIC energy densities expect to reach significantly higher densities so that QGP formation is definitively defined or not.

1.2.3 Signatures

Although the QGP will not be directly detectable, it should be characterized by radiations and residues and how certain physical trends or signatures change. Many signatures of the plasma have been proposed and studied in the heavy ion experiments; some of the more "promising" signatures are

- Dileptons
- J/ψ Suppression
- P_t Distributions
- Large Fluctuations
- Direct Photons
- Strangeness Production

Dileptons

Dileptons (oppositely charged, same-family leptons, i.e. e^+ and e^-) are primarily generated from two sources: decay of vector mesons (ω, ϕ, and J/ψ) and the Drell-Yan process. Dileptons are not signatures themselves of the plasma but may carry information out of the plasma from other signature processes since they do not interact via the strong force. One of the predictions that has come from several authors is that the there may be a shift in the current masses of the quarks due to chiral symmetry restoration in the plasma. If left-handed and right-handed quarks (as defined by the scalar product of spin and momentum within the hadron) are mixed equally, the quarks become essentially massless. If there is mixing in the plasma, the quark masses will decrease and resonance masses should decrease accordingly. Since the u and d quarks are already light, the effect should be more pronounced in heavier quark resonances, such as ϕ ($s\bar{s}$), J/ψ ($c\bar{c}$). Once the lepton mass and energy can be measured, the dilepton mass can be reconstructed (against a large combinatoric background) and the mass of the parent vector meson can be established. The mass, width, and branching ratios are all expected to be affected by the shift in mass.

J/ψ Suppression

Of all the signatures that may signal the existence of the QGP, J/ψ suppression might be the most telling. The suppression of the production of the J/ψ was first predicted by Matsui and Satz[MatSat] using an argument akin to the Debye-Hückel theory of conduction. If we consider an ion surrounded by oppositely charged ions, its potential is

$$\phi(r) = \frac{Ze}{r} e^{-\frac{r}{r_d}}$$

where r_d is the screening radius of the surrounding ions. At small distances ($r \ll r_d$), the potential is the familiar coulomb potential of a bare charge and there is no screening. At large distances ($r \gg r_d$), the potential goes to zero, indicating full screening. At intermediate distances ($r \approx r_d$), the bare ion is partially screened.

With J/ψ screening, we may equate the ions with the quarks $c\bar{c}$ which compose the J/ψ and the coulomb potential with the color potential. In a densely packed hadronic plasma, a c quark may be shielded by non-$\bar{c}$ quarks and its color field may then not extend to a $\bar{c}$ quark beyond the screening radius. Hence, a $c\bar{c}$ pair is less likely to be formed in a plasma. Results of the NA38 experiment (200AGeV) show J/ψ suppression which can not be fully accounted for by hadronic collision dynamics[Salmeron89].

Of critical importance to J/ψ suppression are several interdependent parameters including the screening radius (r_d), the formation and production times (t_f, t_p) of the c and $\bar{c}$ quarks, the distance (r) between them, and their momentum (P_c) with respect to the plasma momentum. The model suggests that the c and $\bar{c}$ quarks must be within the radius of the J/ψ ($\approx$0.5fm) inside the plasma and have time to form a J/ψ resonance before they leave the plasma. We thus expect suppression to increase with a larger volume of plasma, a higher plasma density of quarks, and lower J/ψ transverse momentum.

P_t Distributions

Cosmic ray measurements of very high energy collisions have shown that average transverse momentum of charged particles is significantly higher than the average P_t measured in lower energy collisions. Van Hove[Van Hove] and also Shuryak and Zhirov[Shuryak] have suggested that the rapid rise in the average P_t may be due to the formation of the QGP. This effect is related to the number of degrees of freedom the system has as the temperature increases. We can draw an analogy here to phase changes in ordinary matter. A liquid may have several degrees of freedom, such as rotational, vibrational, and translational modes of motion each mode accounting for $\frac{1}{2}kT$ of the total internal energy. At a higher temperature we reach a transition point where the onset of a vapor phase sets in. At this point the temperature of the system does not change even though the system energy has increased. After all of the material is converted to the vapor phase, the temperature begins to rise again, but not necessarily at the same rate. The number of degrees of freedom may have changed: fewer would yield a higher rate, more would yield a lower rate. If the

QGP forms, tracking the P_t distribution over total energy of the system (center-of-mass energy) may signal the presence of the plasma and its slope may reveal important characteristics about the number of degrees of freedom within the plasma.

Fluctuations

In any set of measurements, large fluctuations may signal the onset of new or unforeseen physical phenomena or they may be statistical variations. Cosmic experiments such as [JACEE] have seen large fluctuations in average P_t measurements but statistics have been too low to unequivocally relegate them to the category of physical phenomena. Large variations in any of the measured signatures may indicate the formation of the QGP.

Direct Photons

Photons created within the plasma have a low probability of reacting with either the quarks or gluons and so have a very good probability of leaving the reaction site unscathed. These "direct" photons may then be an excellent source of direct information about the plasma and its evolution. They will be emitted according to the Stefan-Boltzman law, which implies a strong dependence on temperature:

$$N_\gamma \propto T^4$$

$$< E_\gamma > \propto T$$

Because the mean free path of photons is so much greater than the source size, all stages of plasma development can be observed with them. Low energy photons (0.5-2GeV/c) may provide information about the order of the transition. If the transition from hadronic matter to the plasma is long (the mixed phase), the transition will be first order. Medium energy (2-5GeV/c) photons may provide information about equilibration times, absorption of mini-jets and the transition from perturbative to non-perturbative phenomena[CDR]. High energy photons (>5GeV/c) may provide information about the first collisions and may test our understanding of the plasma's initial phase.

Strange Particle Production

Since the colliding nucleons are composed of u and d quarks and they are the lightest, we can safely assume the plasma will be rich in u, $\overline{u}$, d, and $\overline{d}$ quarks. However, in regions of phase-space where we expect the baryon content to be high, such as the mid-rapidity region, we can expect the production of higher-mass quarks (s, c) to be favored over low-mass quarks (u, d) due to the Pauli exclusion principle. The production of higher mass quarks should be even further enhanced because of the higher temperature. This effect can most efficiently be checked by comparing the number of detected strange particles (i.e. mesons and baryons that contain at least one s or $\overline{s}$ quark) to the number of particles that contain only light quarks, primarily antibaryons such as the antiproton since they are less likely to have been produced by secondary collisions.

1.3 The PHENIX and Muon Identification

The PHENIX Experiment (Pioneering High Energy Nuclear Interaction eXperiment) will measure photons, electrons, and hadrons from relativistic collisions of heavy ions with the primary goal to detect and characterize the QGP (see figure 1-6). PHENIX is one of four experiments located at the Relativistic Heavy Ion Collider (RHIC) presently under construction at Brookhaven National Laboratory (BNL). All of the experiments

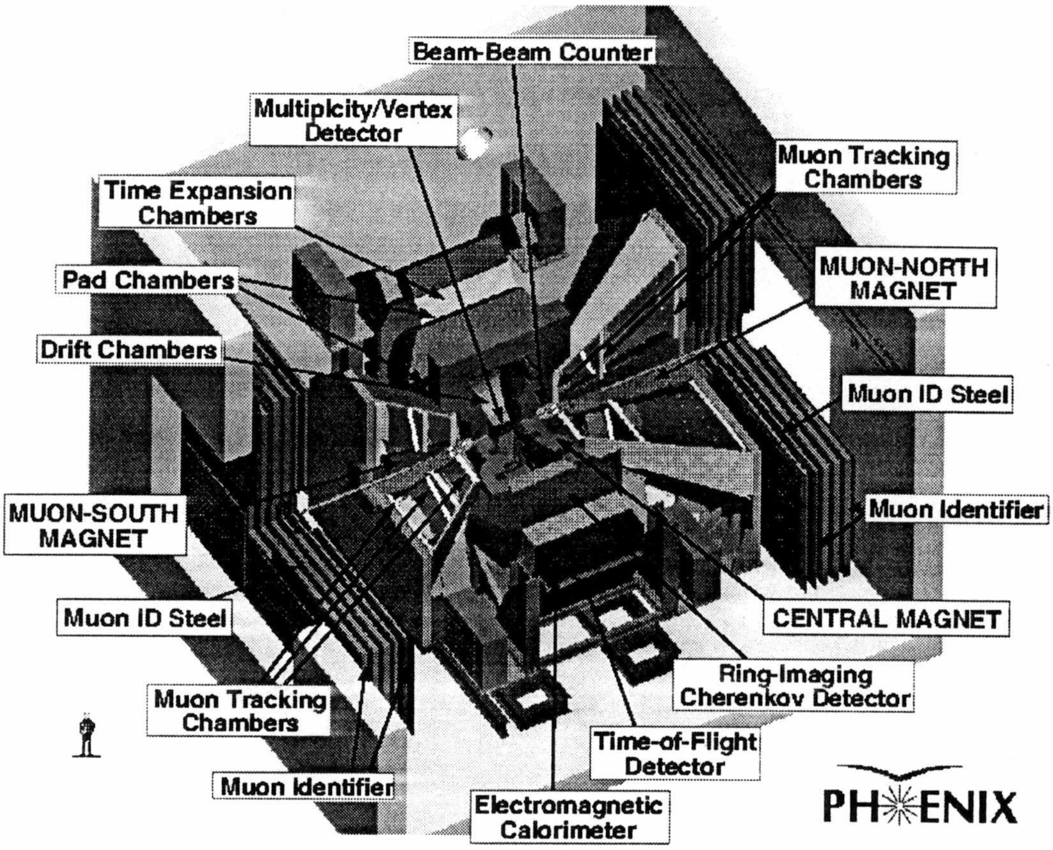

Figure 1-6: The PHENIX Detector.

at RHIC have as their primary objective detection and characterization of the plasma and they too, are all presently under construction at RHIC. PHENIX intends to measure as many of the signature probes as is possible and compatible with a data rate of about 20Megabytes per second[3]. The probes will be measured with respect to a single variable closely related to the energy density of the collision to observe coherent changes in the signatures.

1.3.1 Goals

PHENIX has three spectrometers it will use to study plasma formation from two different perspectives. The central spectrometer comprises a central dipole magnet with equivalent arms of detector subsystems at mid-rapidity that cover 90° in ϕ each and are separated by 67.5° in ϕ. Each arm covers about ± 0.35 units in rapidity. The subsystems individually provide particle identification and hadron/electron rejection of about 10^{-2} to 10^{-4} from several MeV to several GeV which is quite adequate in the mid-rapidity region where particle momenta on the order of 2GeV/c is considered high. The primary purpose of the central spectrometer is measurement of dielectrons (two opposite-sign electrons emanating from the same region of space) for vector meson reconstruction and measurement of direct photons against a large background of neutral meson decays ($\pi^0, \eta \rightarrow \gamma\gamma$).

The other two spectrometers are similar to each other and extend out along the direction of the incident beams. Their primary purpose is detection and identification of muons for reconstruction of vector mesons that decay into dimuons. Each arm is designed to have a mass resolution sufficient to resolve the ϕ from the $\rho + \omega$, the ψ' from the J/ψ, and the Υ(2S and 3S) from the Υ(1S)[CDR]. Moreover, each arm is designed to separate pions from muons to 3% at 1GeV/c and to 1% at 2GeV/c so

[3] The text of this thesis is approximately 2Megabytes; with figures, it is about 25Megabytes.

that pions which may get identified as muons (fake muons) constitute less than 10% of the combinatorial pairs.

1.3.2 Muon Arm Design

Both muon spectrometers in PHENIX have two sections: the tracking section and the muon identifier (see figure 1-7). The tracking section comprises a radial magnet and three stations of multiwire proportional wire chambers. The magnet field is generated by two solenoidal coils positioned at the end away from the vertex region and supplies the magnetic field to the Piston portion and radiates outward to the Lamp Shade. The Lamp Shade is fastened to the first layer of steel for the muon

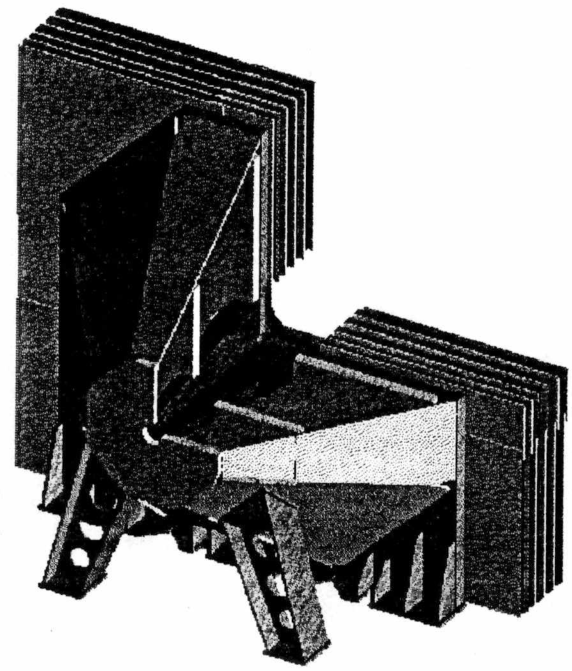

Figure 1-7: Cut-away view of one of the two opposing arms of the Muon Subdetector of the PHENIX Detector. The cone-shaped portion is the tracking section and the vertical plates are the absorbers of the Muon Identifier which cover an area of about 10m x 10m.

identifier which then shunts the magnetic flux back to the coils. The Muon Magnet is basically conical in geometry and opens in θ from 10° to 35°. Since the magnetic field extends approximately radially from the beam axis, particles passing through it experience an axial kick and take a helicoidal path through the tracking section. The integral of the field $\int \vec{B} \cdot d\vec{\ell}$ at 15° provides a kick of 0.72T·m[CDR]. The position and momentum resolution of the cathode strip chambers and the magnetic field provide the necessary mass resolution.

The muon identifier section is a large hadron sampling calorimeter whose primary function is to identify muons against a large background of pions over a large range of momentum. The device consists of six cells, each containing a thick passive iron plate to absorb a portion of the energy of a penetrating charged particle and an active detector layer to detect the presence of that particle or its shower secondaries or its decay products. The method of separating muons from pions with such a device, in a very general sense, is to allow the pion to deposit most or all of its energy via hadronic shower and allow the muon to penetrate. The basic difference in the response will be that pions distribute their energy over a broad area and relatively short depth while muons distribute their energy over a narrow cylinder that extends deeply into or completely through the device.

The advantage of such a device to identify muons is that it is relatively cheap while providing a large area ($\approx$10x10m^2) of coverage. The disadvantage of the device is that statistical fluctuations make particle identification inherently inaccurate at a small, yet significant level. This level of inaccuracy must be kept below about the 1% level in order to achieve the necessary hadron rejection and muon identification efficiencies needed for meson reconstruction. Optimization of the detector in conjunction with muon-pion discrimination techniques provide the primary motivation for the RD94 Experiment.

Chapter 2

The RD94 Experiment

2.1 Experimental Overview

The RD94 Experiment is a research and development (R&D) project aimed at optimizing muon identification in the 1.0-9.0GeV/c momentum range with the goal of separating muons from pions to the 1% level. As the basis for its design, the prototype muon identifier (MuID) used a large-area acceptance sampling calorimeter, finely segmented transverse to the beam axis, to identify charged particles by their unique shower profiles within and their penetration through the calorimeter. Other detector systems were employed in RD94 to locate and identify particles independently of the MuID so as to measure its response. The particle types of interest are protons p, pions $\pi^{\pm}$, muons $\mu^{\pm}$, and electrons $e^{\pm}$.

Figure 2-1 illustrates the arrangement of the detectors along the centerline of the particle beam. This chapter describes all aspects of the experiment including the theoretical basis for muon identification with a sampling calorimeter; all of the goals of the experiment; the detectors and their support systems; the event trigger, data acquisition system, data runs and the simulation program used to help design the

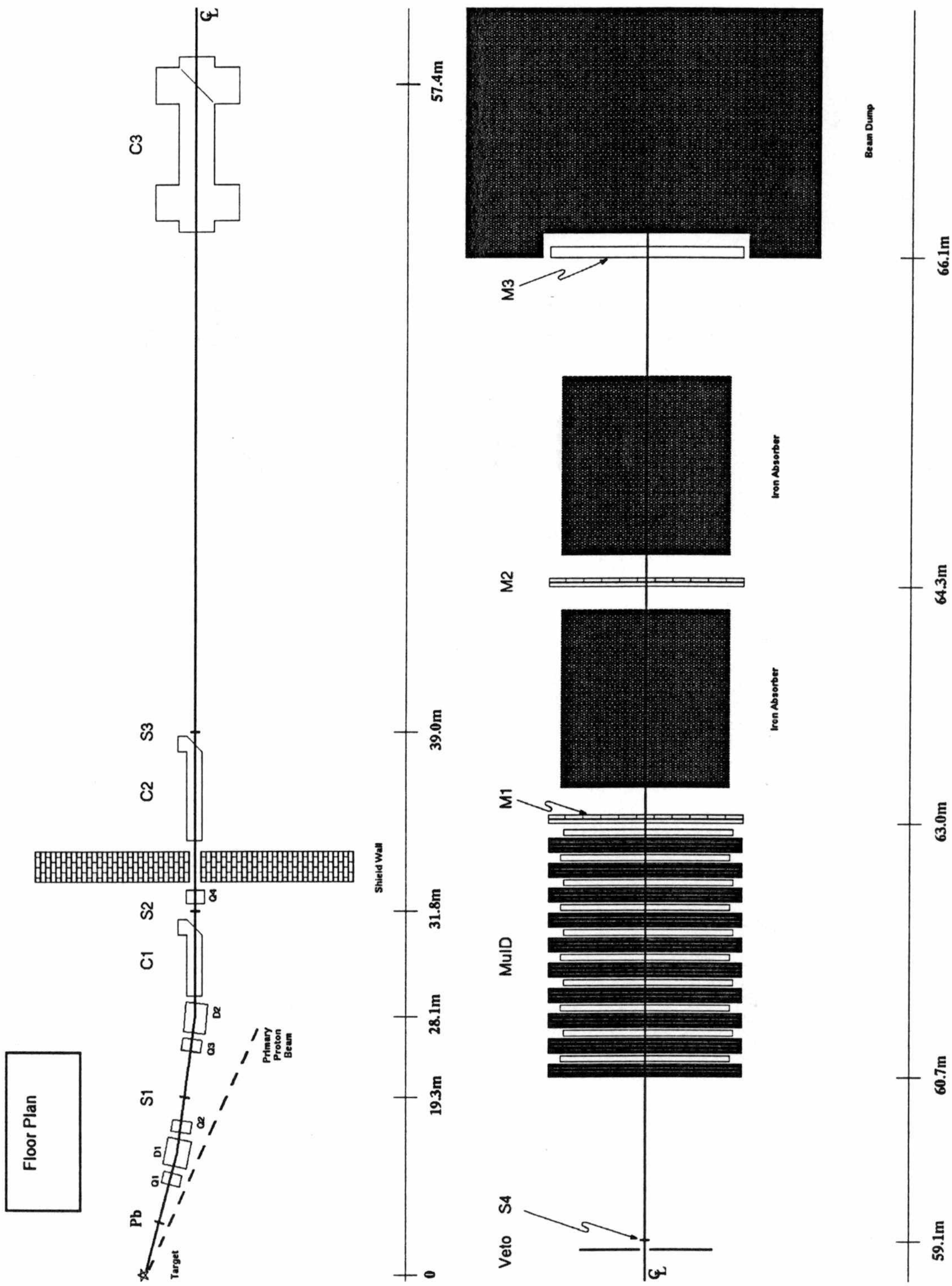

Figure 2-1: Plan View of the RD94 Experiment.

experiment.

2.1.1 Calorimetry

Sampling calorimeters consist of several cells, each of which contain a passive energy-absorbing layer and an active particle-detection layer by which the total deposited energy is "sampled". The number and thickness of cells (sampling frequency), the material types, the total absorber thickness and the particle detection technologies are all design considerations based on considerations such as the range of the energy measurement, incident particle type(s), and cost and availability of materials. For instance, the higher the incident particle energy, the thicker the calorimeter would have to be in order to contain the deposited energy. (Note the use of plurals in the preceding list of considerations: mixtures of materials, their thicknesses, and detector technologies are certainly allowed and often employed[Cornell94].) As an incident particle passes through the calorimeter, it deposits its energy through a variety of mechanisms until it is either fully absorbed or partially absorbed and leaks out in some form (intact, decay products, shower secondaries). Conventionally, an "energy envelope" is defined as the physical volume within the calorimeter where 99% of the incident particle energy is deposited[Sessoms79]. Each detector layer then samples the longitudinal and lateral extents of this envelope from which we may, when the device is properly calibrated, derive the total energy absorbed.

Calorimeters

Sampling calorimeters used in high energy experiments generally come in one of two flavors: electromagnetic and hadronic. Their differences lie in the interaction mechanisms obtained with a given incident particle type, absorber, and energy range combination. These different mechanism groups, hadronic and electromagnetic, determine two scales for all materials, the nuclear interaction length (λ_I) for hadronic and the radiation length (X_0) for electromagnetic. Both scales vary linearly with the atomic mass number (A) of a given material but λ_I varies inversely with the absorption cross section (σ_{abs}) and X_0 varies inversely with the square of the atomic number (Z), resulting in both scales generally decreasing with increasing A, specifically

$$\begin{aligned} \lambda_I &= \frac{A}{N_A \sigma_{abs}} \\ X_0 &= 180\frac{A}{Z^2}. \end{aligned}$$

The dominant mechanisms of energy deposition in electromagnetic calorimeters are bremsstrahlung and pair-production[Fabjan82]. In hadronic calorimeters, fissioning, nuclear excitation and other nuclear effects make energy deposition much more complicated. Moreover, the hadronic shower contains an electromagnetic component arising largely from the creation of π^0s. In either calorimeter, particle production increases geometrically with penetration depth (λ_I, X_0) up to some maximum which is logarithmically dependent on incident energy and predominantly develops in the forward direction. At the point of maximum particle production, the average energy has fallen to such a low level that production ceases and further energy deposition is mostly through collision processes and multiple scattering. A hadronic shower abruptly ceases at this maximum but electromagnetic processes started earlier in the shower likewise continue depositing energy. If a fissionable material is used as the absorber, such as uranium, some of the energy lost to neutron evaporation may become detected through photons and electrons released in the fission process. Fast neutrons also emitted during fission may also be detected by the recoil protons released from elastic collisions.

One of the more striking differences between the two shower types is their lateral developments. Electromagnetic showers tend to develop geometrically and after the point of maximum particle development ($2X_0$) the lateral extent is largely contained within a cylinder of approximately twice the Moliere radius[1]. Hadronic showers do not scale with λ_I, however, they do reach a maximum width of about $1\lambda_I$ occuring at about $2\lambda_I$ deep.

Uncertainty in the energy measurement arises from several sources. One obvious source is the inherent design: only a portion of the deposited energy is measured and since particle production mechanisms are statistical in nature, uncertainty then increases with decreasing sampling frequency. The portion of the deposited energy that is not measured goes into the absorbers and scales with the square root of the absorber thickness. A major source of uncertainty in hadronic showers comes from the nearly 30% of the deposited energy that goes into forms that can not be detected, such as nuclear excitation, nuclear binding energy, neutrino energy, and low energy neutrons. Uncertainty also arises from leakage, both from the back (the more dominant source) and from the sides and from particle detection inefficiency. These last two non-intrinsic sources of uncertainty should be the overriding consideration in the design of a calorimeter. Without proper containment of the energy envelope and efficient sampling, measurements may not be very meaningful.

In experiments leading up to the RD93/RD94 Experiment, a particularly interesting problem arose due to the strong interest in tracking particles that leak out the back of the calorimeter. In general, when designing a calorimeter, one maximizes either the hadronic or electromagnetic showering properties. Both λ_I and X_0 decrease with increasing Z but at different rates. Heavy (large Z) materials tend to be better hadronic absorbers and light (small Z) materials tend to be better electromagnetic absorbers. In either case, the energy envelope generally expands longitudinally with

[1]The Moliere radius is approximately 7A/Z g/cm^2.

lighter materials. In the RD10/RD45 case, a low Z material was forced to be chosen so as to minimize multiple scattering ($\theta_{scat} \propto Z$) of muons (for later tracking). With the choice of a lower Z material, the calorimeter became a less efficient hadron absorber forcing deeper penetration of the hadron shower and subsequent deeper penetration of the accompanying electromagnetic shower. The result was that a relatively large electron flux leaked out of the back of the calorimeter and impinged on the sensitive tracking detectors (multiwire proportional chambers). The solution was to add four inches of lead ($18X_0$) to attenuate the electron flux.

Muon Identification with a Sampling Calorimeter

Because muons have several unique characteristics (mass, rigidity, half-life), one may devise several methods with which to identify them: for example, time-of-flight, or Cerenkov light. However, the single largest impediment to identifying a muon is distinguishing it from its closest-mass neighbor, the pion. A muon's mass is about 75% that of a pion and at 1GeV/c their velocities (with respect to the speed of light) are equivalent to the third decimal place. A time-of-flight system would need timing resolution of about 10ps over 1m at 1GeV/c to distinguish them, assuming equal momentum. Differential Cerenkov counters existthat can distinguish muons from pions but their area of coverage is usually small. Constraints such as large areas of acceptance, and large momentum range and uncertainty, along with requirements of low misidentification rates, make the sampling calorimeter one of the best candidates for a muon identifier.

A sampling calorimeter appears to be the best candidate because it uses the very natures of muons and pions to distinguish them, rather than a mass-related quality, such as time-of-flight or cerenkov light. Muons are by nature leptons, reacting with matter only via the weak or electromagnetic forces. Pions, on the other hand, are hadrons and can react by both the strong (hadronic), weak, or electromagnetic forces. Muons are heavy enough that the dominant mode of energy loss is through elastic collisions with atomic electrons rather than by bremsstrahlung. This quality gives muons high penetration power through matter. The average energy lost by muons penetrating matter is quite linear in the range of 1-10GeV but Landau fluctuations in the elastic scattering processes yield a small fraction of muons that have significantly less penetration power. By contrast, pions have a probability P of reacting hadronically within a depth x of the calorimeter according to the relation

$$P(x) = 1 - e^{-\frac{x}{\lambda_I}}.$$

The fact that muons have high probability of passing through a thick stack of material intact and that pions have a high probability of showering hadronically makes the sampling calorimeter a suitable detector system for identifying muons and distinguishing them from pions. Other, more practical considerations such as large areas of coverage at relatively low cost, wide range of momentum acceptance, and simplicity of design and operation, clearly make the sampling calorimeter the best choice for a muon identifier in the PHENIX Experiment. However, since muons are penetrating, the calorimeter is no longer a total absorption device and so the range of energy measurement of muons is rather limited.

2.2 Goals of the RD94 Experiment

2.2.1 Overall Goal

Historically, the RD94 Experiment comes from a long line of R&D projects that began in 1989 with relatively small tests of sampling calorimeters that varied in depth, coverage, segmentation, signal generation/readout/measurement technology, and absorber material. The ORNL High Energy Reaction Group had gained, prior to these tests, several years experience in sampling calorimetry with the Mid-Rapidity[MIRAC89] and Zero-Degree[ZDC89] Calorimeters used in the WA80 Experiment at CERN and this expertise lead to further studies for a Calorimeter/Absorber for the proposed DIMUON Experiment at RHIC[Cornell94]. Several collaborations, including DIMUON, eventually merged to form a new, single collaboration, out of which arose the PHENIX Experiment. Ultimately, PHENIX's goal, like DIMUON's, is detection and study of the QGP, but the method PHENIX offers differs from DIMUON's and the emphasis of the Calorimeter/Absorber R&D projects shifted toward muon identification. The earlier projects emphasized leakage and particle penetration studies whereas the Muon Identification projects emphasized particle showering by shifting the segmentation of the sampling calorimeter. Now the device is more finely segmented transverse to the beam (4cm as opposed to 10cm) and less finely segmented longitudinally (cell thickness $0.83\lambda_I$ as opposed to $0.23\lambda_I$). Thus, the RD93/RD94 Projects' goal was to identify muons in the environment and under the conditions that PHENIX expects to face. More specifically,

- *the primary goal of the R&D projects was to establish the levels of identification and misidentification of muons in a hadronic environment, with wide ranging momenta, over a large detection area.*

Muon identification can be a relatively easy goal given any one of the constraints that a large experiment such as PHENIX might face. These constraints include a significant pion background, large areas of coverage, a medium energy range, long path lengths between the signal generation site and the digitizer, and passive signal processing (no amplification). What makes the goal quite difficult is the sum of the constraints. These constraints not only begin to define certain aspects of the detector, but they establish secondary goals of the experiment as well.

2.2.2 Secondary Goals

Hardware Goals

One of our hardware goals was

- *to implement Iarocci-type Limited Streamer Mode Tubes (*LST*s) as the primary component of the detection layer in the* MuID.

Iarocci tubes are essentially gas counters that operate in the Limited Streamer Region on the Geiger-Müller Curve (see section 2.4.2). Each of these particular LSTs consists of eight 9mm by 9mm chambers of a specified length (here, 1.5m) separated by a 1mm PVC wall with an anode wire running along the center of each chamber. The gas used was a mixture of Argon and iso-Butane in a 1:3 ratio and the detection efficiency has been measured at 96% not including geometrical efficiency[Battistoni80]. Our intent was to gain experience operating LSTs in an experimental environment and to verify their durability, reliability, and efficiency.

The attractive features of LSTs over other gas counters are low cost, durability, large signal strengths, and a resistive cathode that allows external capacitive pickup of a streamer pulse. External pickups are particularly attractive because the signal electronics need not deal with coupling capacitors to the high voltage anode which tend to breakdown and fail over long periods of operation. Also, the geometry of the external pickup is free to take whatever 2-dimensional shape the user deems appropriate within signal to noise limitations. Our goal was

- *to compare "strip"-like geometry pickups (thin and long) to "pad"-like geometry pickups (square) for signal strength and* MuID *response.*

Design Goals

Although the earlier RD10/RD45 Experiments required the study of calorimeters of various thicknesses, RD94 did not. This meant that the MuID kept a fixed thickness throughout the run period so restacking the iron plates was not necessary. However, the study of the two geometries of capacitive pickups meant that the detector arrays would have to come out of the stack for replacement. This lead to another goal with two points:

- *to design a frame or some housing method*

  1. *that protects the* LST *arrays from the large compression pressures of the absorber plates*, and
  2. *that would allow installation of the arrays without having to restack the iron plates.*

The MuID was deliberately overly segmented in the both lateral (orthogonal to the beam axis) and longitudinal (parallel to the beam axis) directions in order to establish minimum segmentation requirements to identify muons to about the 1% level[2]. Hence, the RD94 MuID was designed

- *to establish minimum segmentation requirements*, and

In measuring the signals produced by the LSTs in the MuID, one has several choices in what parameter of the signal to measure, such as, the time it was produced, the amplitude of the signal, the integral of the current (charge), or simply a yes/no flag. The yes/no flag is the cheapest from an electronics standpoint: the only processing

[2]Technically speaking, the RD94 MUID was not overly segmented longitudinally – overly extended or overly thickened may be better descriptions since the total thickness is more than what is needed to absorb most showers. We say "over-segmented longitudinally" to mean "more cells (or λ_I) than necessary"

associated with it is discrimination (about 5ns) that determines whether the signal was generated from a relevant physical process or not, a yes (1) or a no (0); and little memory is needed (1 bit) and so forth. The other methods require processing which significantly raises the experiment price tag, increases event time (through both processing and I/O with the Data Acquisition System), and increases event memory requirements. For large experiments such as PHENIX, knowing what minimum information is required for the job at hand can mean tremendous savings. With this in mind, RD94 measured the integrated current

- *to determine if the charge measurement was necessary or even useful.*

With this information, the yes/no flag method can be modeled by simply determining a threshold during data analysis to determine if the particular detector was hit, and further ignore the measured charge.

Large experiments typically have tens of thousands of signal channels and the electronics that process those signals are usually expensive and quickly deplete funding. Another hardware goal of RD94 was

- *to design the experiment in such a way that eliminated the need for signal amplification.*

Software Goals

If the applicable physics of nuclear reactions is quantitatively understood, then predictions of detector response should be possible. Many codes exist that attempt this coupling of theory with (simulated) reality but disagreement always occurs at some level. The PHENIX Collaboration uses GEANT for simulation studies and so one of our goals is

- *to benchmark* GEANT *using results of* RD94.

If, for instance, GEANT predicts shallower penetration of pions by some amount, then PHENIX simulations can be adjusted accordingly.

In the RD94 Experiment, clean samples of muons and pions were not always achieved with the on-line trigger system, especially at momenta below 3GeV/c. MuID response to muons and pions can not be individually verified with contaminated samples. Our goal was

- *to establish an off-line discriminant function that separates muons from pions and subsequently determines the detection efficiency of the* MuID *as well as identifies the best and fewest parameters with which to distinguish muons from pions.*

2.3 The Experimental Environment

2.3.1 The AGS

The RD94 Experiment was conducted at the Alternating Gradient Synchrotron (AGS) at Brookhaven National Laboratory (BNL). Located in Upton, New York, approximately in the center of Long Island, BNL has been conducting advanced-level particle research since 1950 when the first of its "mighty machines", the Brookhaven Graphite Research Reactor, came on-line. Although the Graphite Reactor was the impetus for the Laboratory's establishment, plans were afoot for a source of even higher energy particles before the reactor's design was completed. In 1952-3, BNL commissioned the Cosmotron, the first synchrotron that could accelerate protons to the energy realm of cosmic particles – billions of electron volts (GeV). This machine lead to major discoveries such as the K_L^0, the first of the vector mesons(ρ), and the heavy, unstable "vee"(Λ) particles. In the late 1950s, BNL began work on an accelerator, the Alternating Gradient Synchrotron, using newly developed magnet technology – alternating gradients with strong focusing – which reduced the magnet mass, aperture, and bending radius and allowed for greater accelerations and thus higher attainable energies. In 1960, the AGS came on-line and accelerated protons to the unprecedented level of 33GeV.

The AGS is a ring accelerator with a circumference of about 800m with four primary beam lines (A, B, C, and D) along which several secondary beam lines can be found (1, 2, ...). Ions enter the AGS from either the linear accelerator (LINAC) if they are protons or from the Tandem Van de Graff via the Booster Ring if they are heavy ions. The AGS receives a "bucket" of particles and accelerates it to a high energy which depends on the particles' mass. Protons, as mentioned above, can be accelerated as high as 33GeV while gold nuclei typically attain about 11GeV/nucleon. The acceleration takes about three seconds during which time the bucket of particles smears into a uniformly distributed beam. After the acceleration the particles are ready for transport down one or all the beam lines. The AGS operates in one of three modes: slow extraction, fast extraction, or single-bunch extraction. In slow extraction, the particles come out of the AGS with a uniform intensity over the relatively long time of about a second yielding about a 4 second cycle. In fast extraction, the particles come out of the AGS in 12 short bunches spread over 2.75 microseconds yielding a 1.5 second cycle. The last mode of extraction is similar to the fast extraction mode with the exception that only one of the bunches is directed to the primary beam line.

Once the particles are in the primary beam line, they are delivered to experiments sitting directly on the beam line (primary transport) or they may strike a target, usually a thin piece of aluminum, beryllium or copper, and secondary particles emanating from collisions between the primary beam and target nuclei may be directed toward an experimental area (secondary transport).

2.3.2 The B2 Beam Line

In 1992, the AGS constructed a small, multi-user experimental test area on the B-line, denoted the B2 test area, taking the place of the previous test beam area on the A2 test area on the A-line. When the AGS is in slow extraction mode, the test area may receive secondaries from collisions of 24GeV protons with a beryllium target[Carroll] with dimensions 0.6cm x 0.6cm x 7.5cm. The optics that direct the secondary beam to the experimental area far exceeds its predecessor's, primarily because it has two dipole (bending) magnets, each with fore and aft quadrupole (focusing) magnets. The A2 area only had one dipole-quadrupole set, allowing a much broader spread in beam momentum. In addition, the first quadrupole in the B2-line sits closer to the primary beam axis ($8°$ vs. $10°$), allowing for a higher secondary beam rate at a higher energy. The magnets themselves were also upgraded. Higher current magnets allowed selection of beam momentum up to about 9.5GeV/c, although we limited our study to 9.0GeV/c. The last major improvement was the AGS itself. Beam rates often exceeded the 10 trillion particles per spill, which was quite an achievement for the AGS. We actually had to request the control room to lessen the flux at our target to keep our count rate down and prevent pile-up (2 or more beam particles in the event gate). In previous years, the AGS topped out at the 10 or 100 billion particles per spill level, giving an event rate of about 10 events per spill, whereas now the event rate was several hundred and mainly limited by the tape writing speed.

In order to boost the electron flux, typically low at low momentum due to the much more dominant hadron flux, a 2mm thick lead converter was positioned in the beam, downstream of the target but upstream of the unused S1 start counter (not shown in figure 2-1). This thin piece of lead boosted the electron flux by simple conversion of low-energy (few GeV) photons via pair production. Because the converter was so thin, little flux was attenuated and because it was positioned close to the target

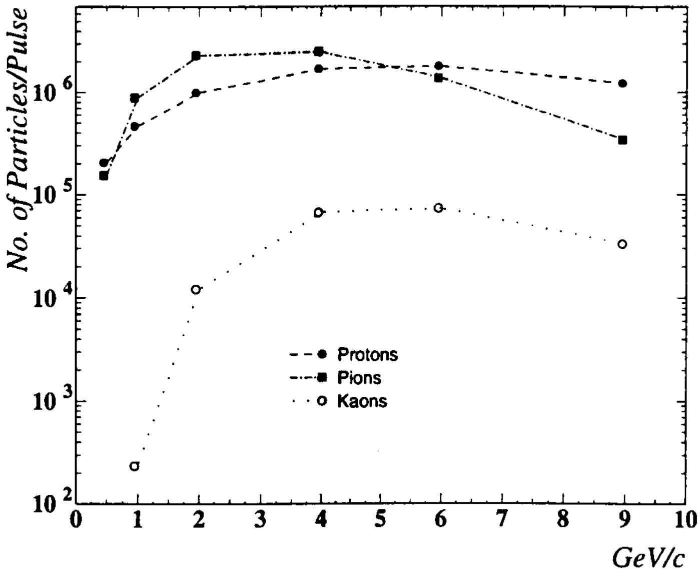

Figure 2-2: The beam profile as predicted from calculations[Carroll].

and upstream of the bending and focusing magnets, it could not degrade the beam. The result was a much higher electron flux at low momenta. Figure 2-2 shows the predicted numbers of protons, pions and kaons, positives only[3].

DIBBUK and Magnet Control

In order to give as much flexibility and control of the beam to the experimenter, the AGS implements a fully automated beamline control system called DIBBUK. This system allows the user to remotely adjust any of the magnet amperages and collimator positions with point-and-click simplicity. All settings can be saved, recalled, and reloaded, so one can easily return to a particular momentum (barring hysteresis) in a short period of time (10sec). The system also has a tutorial for the new user and printing capabilities.

[3]The curves were "calculated for the solid angle calculated by a beam program, the Sanford-Wang particle production formula for 24 GeV incident and 6 Deg production"[Carroll].

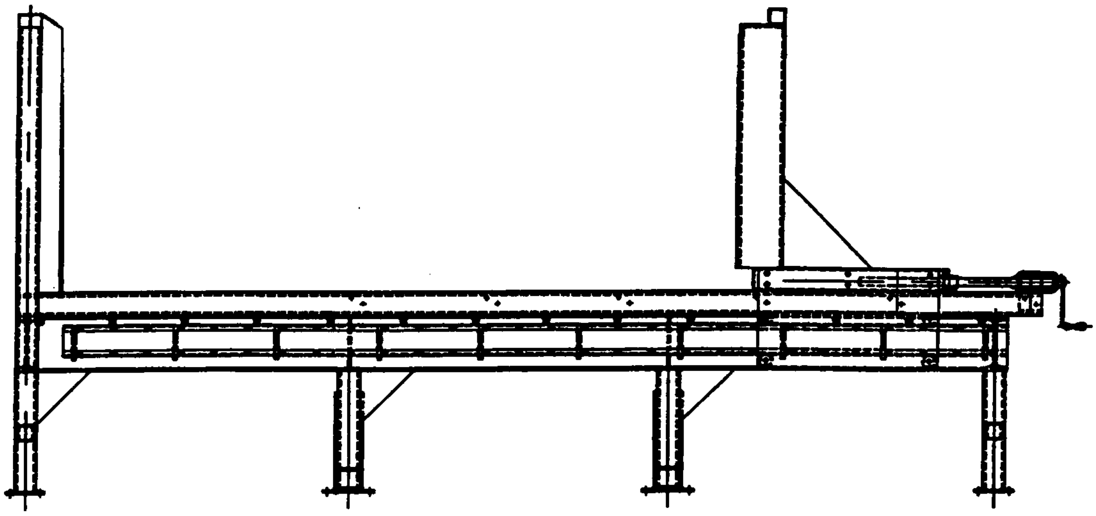

Figure 2-3: Elevation view of the MuID supporting stand.

2.4 The Muon Identifier

2.4.1 Design Overview

The RD94 MuID design began with several parameters already determined, or limited. Originally, when the earlier RD10/RD45 experiments were first being considered, a reusable stand was built (see figure 2-3) to accommodate several restackings of the calorimeter during a typical run period thus allowing several different calorimeters to be studied without having to redesign support structure for each. The stand was required to support thin metal plates (4ft by 4ft) stacked on edge while allowing sensitive detector planes to be inserted periodically between them without being crushed, as well as allowing all four lateral sides free of support structure and encasement for access to the detectors. The stand eventually took the shape of an oversized bookcase, with the downstream end stationary and the upstream end having a movable "bookend". The lateral size of the calorimeter, and thus the stand, was determined by minimizing the amount of leakage from the sides of the detector but keeping the laborious job of restacking as simple as possible with small cranes. Thus, the 4ft by 4ft lateral dimension was chosen. The stand was designed to facilitate the study of any calorimeter of any thickness less than 12ft and lateral extent less than 4ft on a side and so the MuID lateral and longitudinal dimensions were limited in this way (see figure 2-4). In addition, the choice of absorber material is somewhat limited. The material must have a small λ_I so that the thickness does not exceed available floor space. A self-supporting material would be ideal since containers and supports would not have to be purchased which not only add to the cost of the project, but to the thickness of the calorimeter as well. Also, to keep costs down, the material should have as

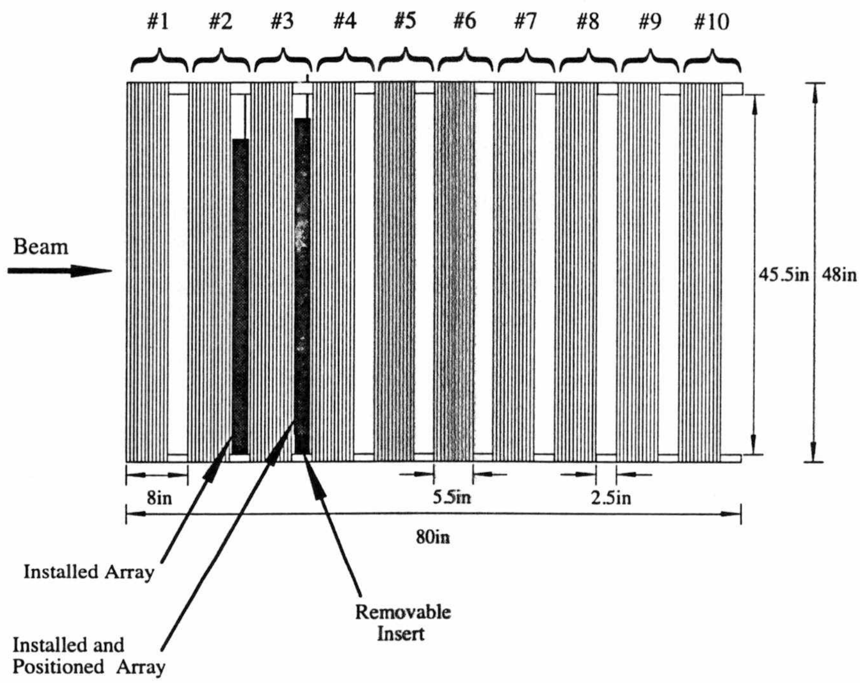

Figure 2-4: Elevation view of the Muon Identifier showing two installed arrays. The array in cell #3 has been correctly positioned vertically by a removable insert.

few special handling requirements as possible. Materials such as uranium or beryllium have high toxicities and machining them on large scales would be prohibitively expensive. These requirements limit the choices to basically two metals: iron and aluminum. Iron was chosen for its smaller λ_I. The actual iron plates available were 4ft by 4ft by 1/2in in physical dimension and had a density of 7.87g/cm^3.

The lateral extent of the MuID was determined by the height of the array of LST supertubes (a PVC jacket holding 4 LSTs) that could fit into the stack. Since the MuID's absorber height was 4ft (or 120cm), the number of LST supertubes was limited to three (34.2cm each) for a total height of 102.6cm. To keep construction and data analysis simple, the width of the MuID was put at 102.6cm as well, even though its only real restriction was the 4ft side-to-side dimension determined by the stack of metal absorber. The active area of the MuID was then 102.6cm x 102.6cm.

The longitudinal extent of the MuID was determined by how many metal plates we could obtain, limited of course by the physical length of the stand. A simulation study was performed using GEANT (see section 2.4.3) to determine the best arrangement (distribution) of iron plates, that is, how the thicknesses of individual cells should be distributed, given a certain overall thickness. The study concluded that a uniform distribution performed about as well as or better than the others over several momentum ranges. Therefore, the number of plates used needed to be an integer multiple of the number of cells to keep the cells of uniform thickness. At that time, PHENIX's design had 10 cells, which was then chosen to be the number of cells for RD94. The plate number then had to be an integer multiple of 10. One hundred thirteen plates were targeted for the experiment which then meant 110 plates would be used giving 11 plates to each cell.

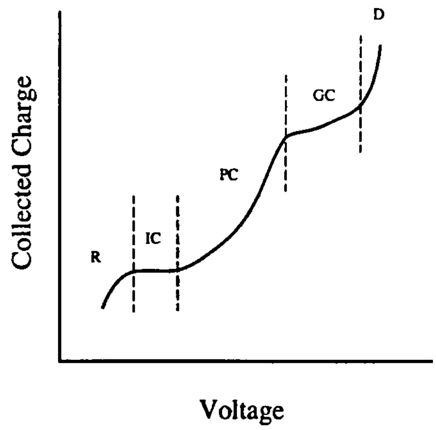

Figure 2-5: The Geiger-Müller Curve showing various regions of gas phenomena. **R** is the recombination region; **IC** is the ion chamber region; **PC** is the proportional region; **GC** is the Geiger region; and **D** is the continuous discharge region.

2.4.2 LST Detector Arrays and the Active Region

LST Design

At the time of this writing, Limited Streamer Tubes (LSTs) are the technology choice for the detector layers of the PHENIX Muon Identifier, and these were implemented in the RD94 MuID. LSTs have been on the market for more than ten years with a proven record for durability, reliability, good efficiency[Battistoni80]. The limited streamer mode of operation is similar to the geiger mode (see figure 2-5) in that the pulses are large ($\approx$30pC) but the pulse's extent along the wire is limited to about 1cm, due mainly to the UV-absorbing component of the gas. What has come to be known as the "standard" LST consists of a tray made from PVC with eight extruded U-shaped chambers. (see figure 2-6). Each chamber is approximately 9mm from septa to septa, and also 9mm from the bottom of the U to the top. A 1mm PVC wall separates the chambers, giving the LST a 1cm pitch. The length of the tray can extend up to many meters[Ellila87]. After the graphite coating has been applied and the anode

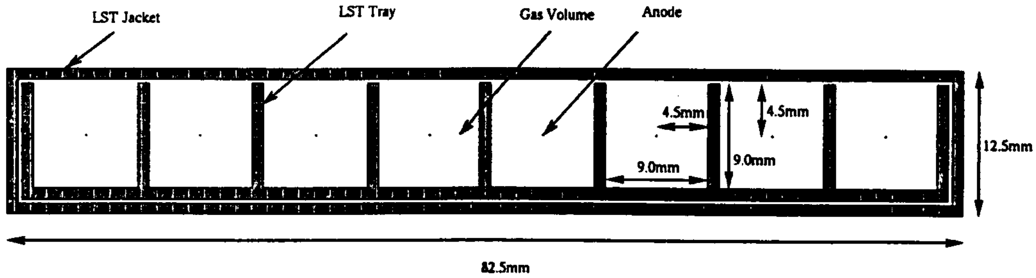

Figure 2-6: Cross section of a Limited Streamer Mode Tube.

positioned, the tray then slides into a PVC jacket. The anodes are then secured to a high voltage bus on one end and terminated at the other and the endcaps are epoxied on. This then is the standard LST which was purchased at relatively low cost, given the area of coverage, efficiency, etc. An additional support jacket, called a supertube, can house four LSTs, side-to-side. The final detector array stood three supertubes on top of each other (see figure 2-7). to give a total active streamer-producing height of 3 x 4 x 8 x 9mm = 86.4cm distributed over 102.6cm yielding an average geometrical efficiency of 84.2% for particles incident normal to the detector plane over its entire face.

Geometrical efficiency increases quickly with incident particle angle. Normal to the detector plane, an incident particle has a 10% chance of passing straight through one of the 1mm PVC walls and a 90% chance of passing through one of the 9mm chambers. When the LSTs sit side-by-side, their outer jackets add some dead space, and when the LSTs are placed in supertube housings, even more dead space is added. The dead space between two supertubes can be as much as a 8.2mm, almost the width of a single chamber (see figure 2-8). The good news is that as the incident angle declines from the normal, the geometrical efficiency increases because the incident particle sees effectively larger gas volume cross sections and at large enough angles

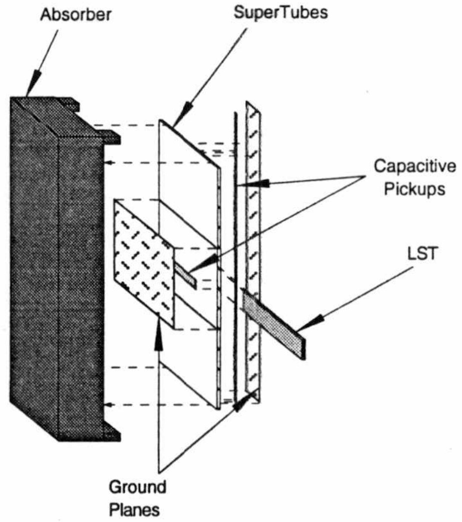

Figure 2-7: Perspective view of a cell in the MuID.

i.e. 6°, the gas volumes overlap and the geometrical efficiency is 100%.

Capacitive Signal Readout and MuID Boundaries

The next component in the array is the capacitive readouts. Much discussion and planning went into strip and pad readout design, particularly since the number of channels was limited by the available electronics. Figure 2-9 shows the relative sizes of the two geometries of pickups used. With six 96-channel ADCs[4] available (576 channels total) and 10 detector planes, not more than 57 channels could be allotted to a plane. Dividing 57 in half (for horizontal and vertical orientations of strips) left no more than 28 channels per orientation per plane. Allowing some spare channels (in case things break) then dropped the channel count to 24 which happens to also be convenient: with 96 streamer chambers in a plane, 24 channels meant an even 4

[4]Both Lecroy 1881 and 1885 fast bus ADCs were used.

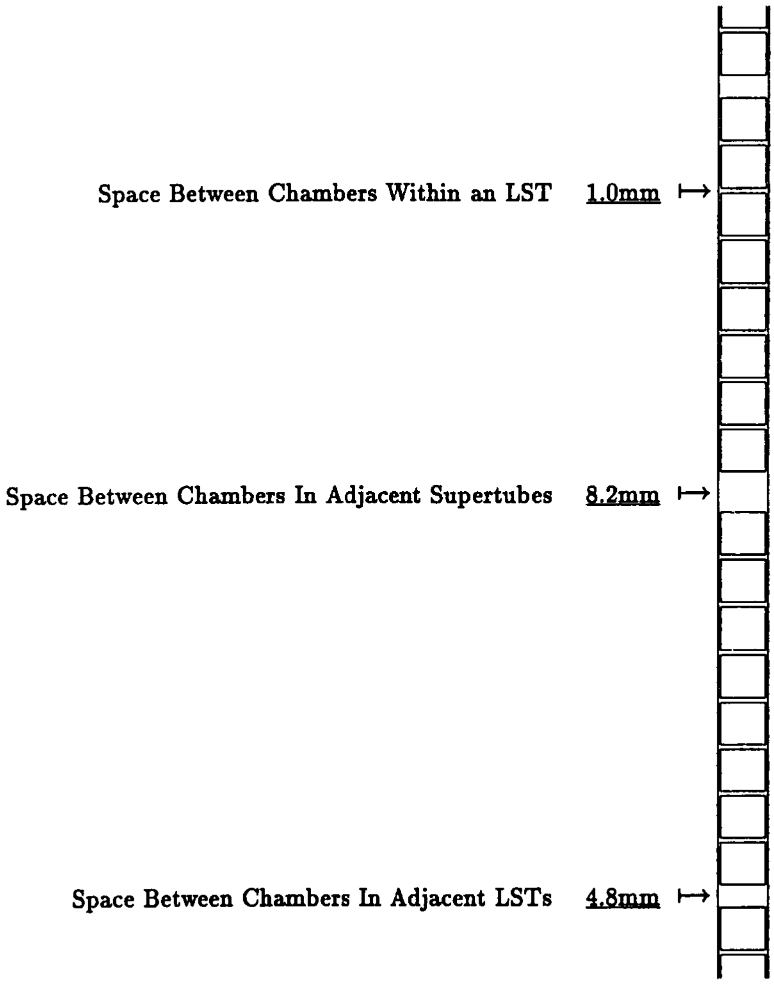

Figure 2-8: Cross-section of a portion of an LST showing dead spaces between the chambers.

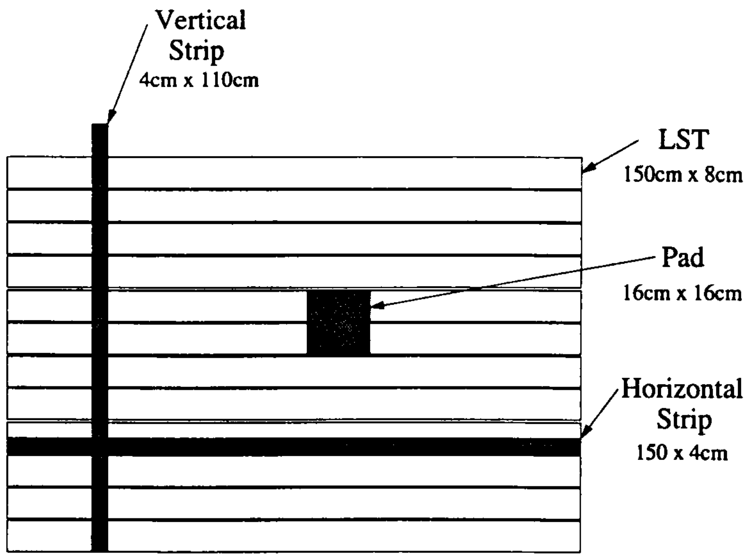

Figure 2-9: Comparison of relative sizes of capacitive readouts.

chambers (horizontal) per readout strip which prevented partial chamber overlapping of the strips. Also, the construction became simpler since a board with 8 strips matched the width of a supertube. The final strip width was then chosen to be 4cm with a 2mm separation.

Lessening the channel count to 24 per orientation per plane then accounted for 2 x 24 x 10 channels, exactly 5 of the 6 fast bus ADCs. As it turned out more channels per plane were needed for the pad readouts when they were installed. With 96 spare channels, it was decided that half would be used as spares, leaving the other half for the extra pad channels. The pads were made as large as possible, yet not so large as to make construction complicated and not so small as to exceed the number of allotted spare channels, 48. The chosen pad size became 16cm x 16cm, thus putting 2 x 6 pads evenly on a supertube and making the total pad channels per plane 36. Therefore 12 extra channels per plane with pads were needed. Since only 3 planes had pads on one side of the array, the total extra channels needed was 36, nicely below the half-ADC count of 48.

An important consideration in the design of capacitive readouts is the actual capacitance itself. The capacitive readouts used here simply have thin copper foil adhered to both sides of a thin PVC corrugated board. This forms a capacitor with capacitance (C_g)

$$C_g = \epsilon \frac{A}{d}.$$

Since the area (A) is determined by the desired pickup area, the capacitance can be controlled by choice of material with permittivity (ϵ) and material thickness (d). This capacitance determines the transmission characteristics of the readout which is important for matching the impedance of the signal transmission line. Without proper impedance matching, significant fractions of the pulse (amplitude, integral area) are not transmitted across impedance boundaries but reflected. The losses then reduce and distort the signal and reflections can interfere with signals produced later. Although the strips and pads were designed to match our cabling impedance (50Ω), we nevertheless had some reflection. However, it is unclear if the source of the reflection was due to the pickup capacitance or a slight impedance imposed by the connector to the signal cable.

When the readouts are coupled to the LST, a second capacitor is formed C_c between the pickup and the resistive cathode (see figure 2-10). As a streamer forms, its positive image forms on the cathode and this capacitor (C_c) charges up on a time scale about that of the streamer formation time giving the observed pulse about a 5ns rise time. The capacitor also begins discharging but at slower rate proportional to the $R_c C_c$ time constant of the circuit which, in practice, is controlled by the resistivity (R_c) of the cathode[Battistoni82] and is typically on the order of 50ns.

The resistive cathode may be thought of as a kind of window that allows the strip to "see" the streamer charge and the resistance of the cathode controls the "trans-

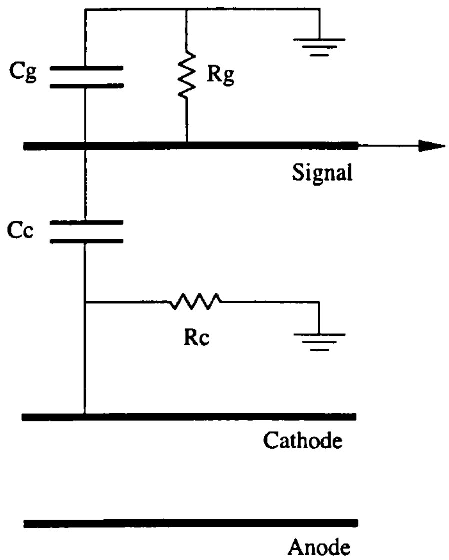

Figure 2-10: Schematic of signal pickup from an LST.

parency" of the window. [Battistoni82] defines transparency as the ratio of the signal amplitude on a strip directly above the signal generation site to the signal amplitude on an adjacent strip. Testing both 1cm and 2cm strip widths, oriented orthogonal to the anode, they found that transparency increases approximately linearly with cathode resistance (R_c) from about 10K$\Omega/\Box$ up to about 100K$\Omega/\Box$ where it levels off. High R_c has two implications on signal pickup: (1) that orthogonal strips over a broad length of the anode will see the signal; and (2) that strips parallel to the anode will pickup a larger pulse. These two dissimilar pickup characteristics are in fact observed in RD94.

LST Array Construction and Preparation

The detector array's primary components are streamer tubes and capacitive pickups. Supertubes, thin plywood, banding straps and string,together with the primary components, completed the array. The array design hinged on one question: to glue or not to glue. Quite often with LSTs, one glues the strips in place[Ellila87] conveniently keeping the pickups attached and certain glues have been shown to not alter the capacitance significantly. One may also glue the strips to the exterior of the supporting supertube, allowing the LST to be removed and replaced without disturbing the assembly. RD94 opted to use supertubes but instead of gluing, we chose to build an assembly that compressed the pickups against the LSTs sufficiently to pickup the signal without collapsing the LSTs.

The advantage of not gluing is that the pickups can be reused in other capacities. Also, without gluing, different sets of pickup geometries could be installed, while using all the other parts of the same assembly; with gluing, new supertubes and pickups would be needed. One more advantage is portability. Once the pickups are glued on, the array becomes an unwieldy 1m x 1.5m plane that would require great care in transport. Without gluing, everything can easily be transported in a box. The disadvantage to not gluing is twofold. The compression technique we used was not especially sophisticated and air gaps developed between the pickup and LST which increased the capacitance (C_c) and broadened the pulse. Since the integrated current (and not the pulse amplitude) was measured, the air gaps were not a significant problem for us, even though some of the signal would be lost to the upper limit of integration time. The other disadvantage is structural strength and array thickness. With gluing, the LSTs and strips become a rigid plane without need of any further support. The advantage here is that the thickness of the array is about 2cm. Without gluing, the components needed for compression and support (here a 1m x 1m piece of plywood) adds considerable thickness, totaling just over 2in, and thus adds overall thickness to the MuID.

The array was constructed in this order: First a square piece of plywood was laid upon an assembly table. Four holes were drilled in strategic places earlier and at this point, 2 long pieces of string are laced through 2 holes each. Next, 3 boards of vertical strips are laid upon the wood, ground plane side down, and the strings are brought between them. Next the supertubes with LSTs installed are laid on top of the vertical strips, orthogonally, with care to note the orientation of the LSTs (graphite side should be toward the vertical strips)[5]. Here the strings should be threaded between the supertubes. The horizontal strips (or pads) are placed on top, aligned with the supertubes and then the top plywood piece is laid down. The string must then be threaded up through the holes. The next step is to make sure all components are properly aligned. Then the straps are banded around vertically near the edges and then the strings are tied as tightly as possible. This, then is the detector array assembly.

Once the array was assembled, it was installed in the absorber stack. The spacers that were welded onto the top and bottom of every eleventh absorber plate provided a $2\frac{1}{2}$in space for the array and allowed it to be installed from either side of the stack but they required the height of the array to be less than 45.5in ($\approx$115cm). The height of the three supertubes was only 102cm, conveniently less than the 115cm provided by the opening between the spacers. However, the vertical strips were required to extend above the top of the stack of iron so the signal cable could connect to the strip. The height of the vertical strips was therefore made to be 110cm. Once installed, the array had to be vertically centered in the beam line. This was accomplished by inserting a length of wood (non-conducting) under the array to lift it $2\frac{3}{4}$in. In so doing, the vertical strips then broached the top of the iron stack about 1in. In addition, the height of the wooden inserts was staggered so that alternate planes were offset by half of a chamber width (0.5cm$\approx$0.25in) to stagger the dead spaces in the LSTs.

[5]One can determine this orientation by peering into the gas inlet on the LST.

The Gas System

When streamers are formed, hundreds of thousands of ion pairs are produced near the anode. Electrons collect at the anode and the heavy, slow-moving ions drift toward the cathode. When the electrons reach the anode, they quickly diffuse along the anode network and are eventually removed by the high voltage power supply. However, the ions can not travel any farther than the cathode surface because of their size. Eventually the ions will recombine with electrons either along the path toward or upon reaching the cathode. A gas replenishing system was implemented in RD94 to prevent static charge buildup[6] of the heavy, slow-moving ions at the cathode and possible distortion of the electric field; and to ensure that the proper gas mixture is maintained. The gas used was a mixture of Argon and iso-Butane in a 1:3 ratio. This mixture has come to be known as the "standard" mix by many who use LSTs. Preliminary benchtop tests showed that the standard mix provided stable single streamers with little or no after-pulsing when voltage was kept within the limited streamer plateau.

The driving criterion in the design of the gas system was ensuring an accurate ratio(Ar:iso-Butane::1:3) of gases in the mix. If too much iso-Butane is present, recombination of the ionized gas molecules becomes more dominant and the sensitive volume around the anode decreases making the detector less efficient. If too little iso-Butane is present, the mode of operation shifts from the limited-streamer mode to the streamer or spark mode or even to the constant-discharge mode and serious damage to the anode may result. In order to keep the proper ratio, two issues dictated the basic design of the gas handling system: the vapor pressure of iso-Butane(35psi) and the need for continuous flow.

[6][Battistoni80] reports exposing a detector very much like an LST to a Sr^{90} source with no gas flow. After 2.8 x 10^9 pulses over about a 1cm length of anode,"no appreciable effect was observed".

The easiest way to mix gases is by the method of partial pressures. The first benchtop tests we performed on LSTs used a gas mixed by this method. Briefly, a tank was evacuated and filled with iso-Butane to 30psi. Argon was then bled into the tank until the total pressure was 40psi, resulting in about a 1:3 mix. The resulting gas mixture worked well as a test mixture for initial LST studies but an independent verification of the precise ratio was not performed and since the pressures were measured to $\pm$2psi, it was felt that a more accurate method was needed. Besides, iso-Butane's vapor pressure limited the total pressure of the mixture to about 40psi, which means that an extremely large volume would be needed to prevent the need for frequent re-mixing. The volume used for this test-mix was approximately 4ft^3. At a typical flow rate of 20cc/min, the gas would be depleted in about 100 hours (4 days). For the RD94 Experiment about 10 times this rate would be needed, requiring mixing every eight-hour shift which could not realistically happen given the manpower requirements and limited beam time. Another, more subtle, problem is that the tank pressure decreases with depletion which continuously alters the flow rate. A simple solution to this would be to add a flow controller to the system to automatically compensate for pressure changes at the source. However, an even better solution would be to add two flow controllers, one for iso-Butane and one for argon and eliminate the need for manual mixing altogether. This, in fact, was the method used in the RD94 MuID (see figure 2-11).

High Voltage System

To energize the LSTs, RD94 used a CAEN model 270, 40 channel, high voltage (positive) power supply. Since each channel on the supply had a high enough current rating (200μA), one channel alone could supply an array of 12 LSTs, allowing each detector plane to be operated as a unit(see figure 2-12). The characteristics of this model

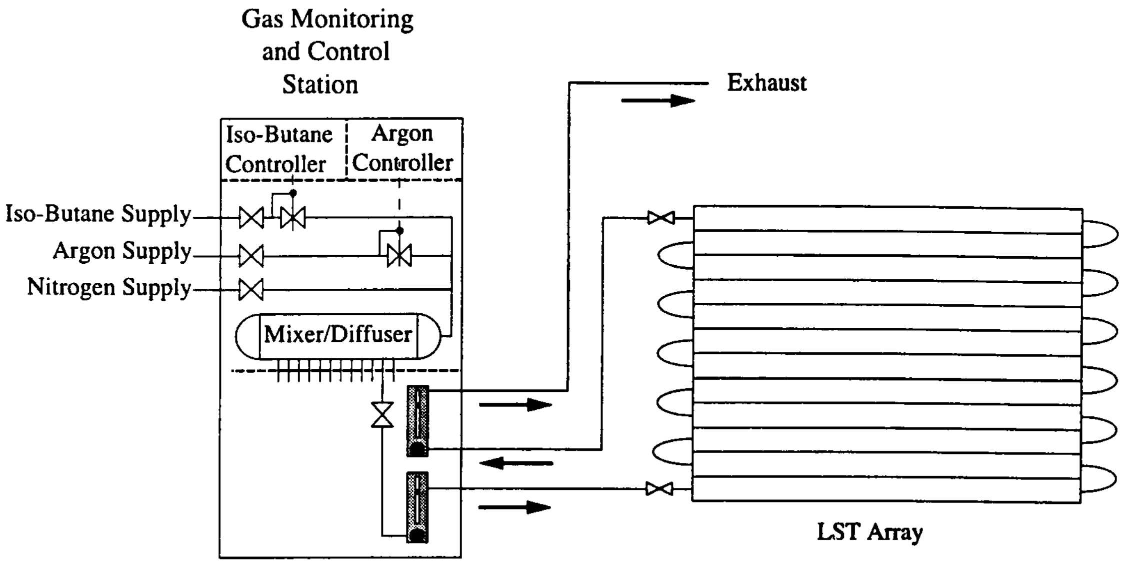

Figure 2-11: Flow schematic for the gas-handling system.

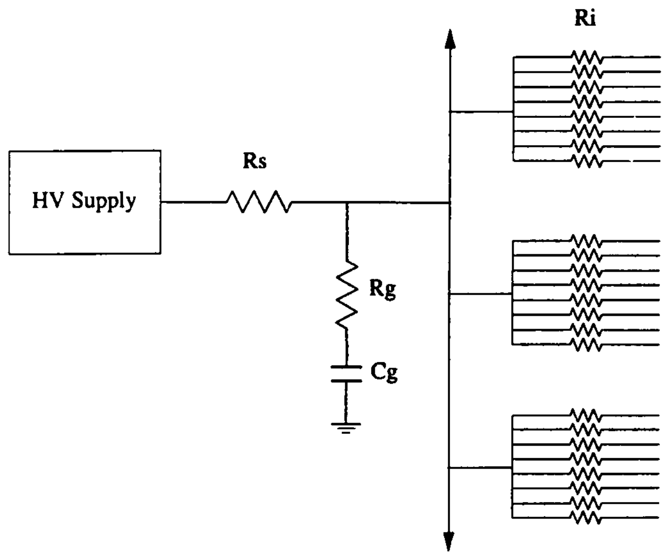

Figure 2-12: High Voltage Network for the LSTs.

power supply make it well suited for supplying LSTs. Three useful characteristics are

- high power: +5500V at 200μA per channel;
- high current trips may be set to decrease the voltage at a user specified rate;
- factory installed software that can automatically burn-in LSTs and lets the user control aspects such as voltage ramp-up and ramp-down rates, current limits and step voltages and time intervals;
- control may be interfaced via RS-232 connection on the face of the supply for remote and automated control.

Throughout the experiment, the supply worked well and may even be credited with saving the experiment. Due to a communication error during some tests of RD94, voltage was left on while the iso-Butane component of the gas mixture was turned off. Without the UV-absorbing iso-Butane, the operating region shifts out of the limited streamer toward the continuous discharge region and the pulses become very large. Continued operation in this high current region has been shown to damage anodes and render LSTs unusable. Fortunately, even after operation like this for two days, no damage to the LST or the power supply was observed.

LSTs may be operated in one of two modes[Battistoni86]: constant charge or constant voltage. The difference is determined by how the high voltage line is coupled to the LSTs. In both modes, a high impedance resistor (1MΩ) couples the high voltage line to an LST. In the constant charge mode, a large capacitor (several μF) connects the high voltage line to ground on the LST-side of the 1MΩ resistor. Here, the capacitor drops the signal pulse to ground and the other anode potentials are undisturbed. In constant voltage mode, no capacitor is present to drop the pulse so it (a negative going pulse) spreads out along all anodes on the LST-side of the 1MΩ

resistor and induces a slight negative charge on the horizontal strips. To keep the streamer charge as constant as possible, RD94 used the constant charge mode.

Conditioning

Although the resistive cathode has the advantage of allowing external capacitive pickup of the signal pulse, it brings with it a small difficulty. The resistive coating is applied to the surface of the LST by applying graphite in a colloidal form with isobutyl-methyl-ketone[Ellila87]. The technique has improved somewhat since the idea's inception so as to make the signal transparency uniform and to minimize flaking. Although the distribution of graphite has become quite uniform with improved techniques, flaking remains a problem. Flakes of graphite may loosen on the surface of the cathode, rise up some, and cause a distortion in the electric field which may result in a continuous discharge to the anode (given high enough voltage). Also, bits of carbon dust may collect on the anode which similarly results in a singularity and a nonuniform field strength. Continuous operation with a "hot spot" will discolor the anode, cause pitting, and eventually cause failure. Since LSTs are sealed (with the exception of gas connections) the remedy is to allow the discharge to occur, but to control it in a manner that eventually burns the flake off. This procedure is better known as "burn-in". Anytime the LST is moved or jostled, the "burn-in" procedure must be performed to literally burn off any flakes that may cause field distortions. The procedure may be automated but we chose to burn-in the LSTs manually. Basically one simply raises voltage in 500V steps slowly and monitors LST current keeping it below 1-2μA per LST until 4400V is reached. Newly created LSTs that have never been energized need a somewhat more cautious high voltage ramp-up. Once 4400V (the low end of the operating plateau)is reached it is recommended that voltage be raised at 100V steps and held for periods of 30min while maintaining current below

$2\mu A$. When 4850V is reached, voltage steps of 50V should be taken and held for 60min. When 4900V is reached, it should be held for 120min. Afterwards the LST is considered operational.

2.4.3 Absorber Design Criteria

The last question to answer before construction of the RD94 MuID began was how to distribute the LSTs within the stack of iron plates. Many arrangements can be imagined; in fact, more than 10^{13} different arrangements exist for 10 detector planes and 111 plates. We can weed out most of these arrangements with a little reasoning. First, consider pions. Since pions hadronically shower (most of the time) within $5\lambda_I$, we might consider a few arrangements that have a large density of detector planes on the upstream portion of the stack. Conversely, we may want high higher density toward the downstream portion due to penetrating shower secondaries. We should also consider that we have to detect muons and that they have a fairly broad range of energy (1-9GeV). These two considerations suggest a more uniformly distributed arrangement. With these considerations in mind, we chose 5 arrangements to study: uniformly distributed; linearly increasing or decreasing with depth; and exponentially increasing or decreasing with depth (see figure 2-13).

Using GEANT3.15 (see section 2.9) for the simulation code, we let 2000 muons and pions of a given momentum impinge upon each of the 5 arrangements. A particle was detected as a muon if it passed through the stack or as a pion if it did not. Since this is a simulation study, we know what the actual particle type and from the simulated detector information we are given what the detected particle type is. With this information we can set up a 2 by 2 matrix where the rows are actual particle type and the columns are detected particle type. Along the diagonal we have the quantities such as actual muons that were detected as muons and actual pions

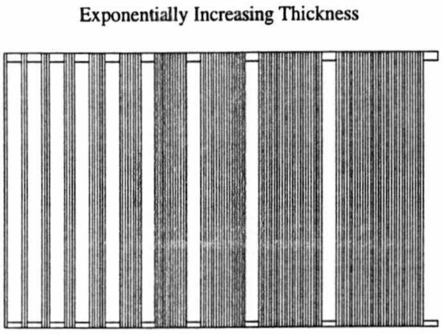

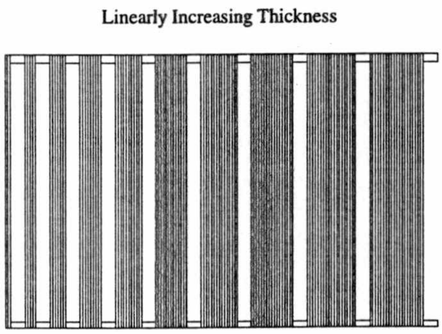

Figure 2-13: Absorber plate configurations, other than uniformly distributed plates (see figure 2-4), under consideration for the Muon Identifier.

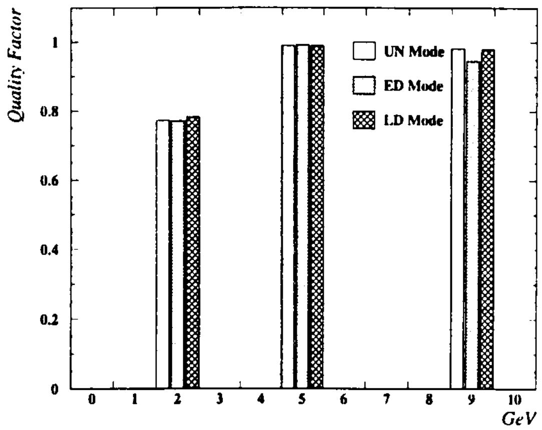

Figure 2-14: Quality factor of three absorber plate configurations (modes) calculated at 2, 5 and 9 GeV. The configurations are uniformly distributed (**UN**), exponentially distributed (**ED**), and linearly distributed (**LD**) plates. The **UN** and **LD** bars are horizontally displaced on the abscissa for clarity.

that were detected as pions. The off-diagonal elements then refer to misidentified particles. The determinant of this matrix will then be interpreted as a "quality factor" (qf). A qf of 1 would imply every particle was correctly identified and a -1 would imply all were misidentified. Figure 2-14 shows the quality factor calculated for three configurations of the MuID plates. All three distributions have similar quality factors at the three energies of the study, 2, 5, and 9 GeV. Since no configuration was shown to be significantly better than the others, the uniform distribution was chosen.

2.5 Incident Particle Identification

The first step in understanding the response of the MuID to a particle type is to know what that particle type is. All the detectors in the RD94 Experiment, besides the MuID, were designed and operated to select different particle types. Some of these detectors were located upstream from the MuID so as to give direct particle identification prior to striking the MuID. Others were located downstream of the MuID, whose basic function were to distinguish muons from pions at high (>3GeV/c) momentum.

2.5.1 Start Counters

The RD94 Experiment used three "start" counters, denoted S2, S3, and S4, to define raw beam particles incident on the MuID. A fourth counter, S1, was located so close the target (see figure 2-1) inside the primary cave that its continuously high count rate from background radiation rendered it unusable.

The start counters — so-named because they start the event trigger — were distributed along the beam line in the experimental area so as to put the maximum distance between them, while allowing access to the signals by all users of the B2-line. By maximizing the distance between detectors, we subsequently increase the resolution of the measurement of a particle's mass[7] by measuring the time that each counter was hit with respect to the event start time (flight time). If we know the momentum of the particle, which we do since we select it by adjusting the magnet's current settings, and it's flight time, we then know the velocity (β) and mass. Particle identification can be made off-line with this information but, on-line (during data-taking), time-of-flight information was not used. While on-line, the start counters were only used for "raw-beam" definition. See appendix A.

All three start counters were thin scintillating plastic with dual photo-multiplier tube readout, optically coupled through a lucite plastic wave-guide. Each plastic scintillator was 0.5cm thick and their vertical and horizontal dimensions varied ac-

[7]Actually, rigidity (mass/charge) is the more correct term since the dipole magnets D1 and D2 bend particle trajectories by their momentum/charge. However, all particles under RD94's study have the same charge of $\pm e$ so mass is not an incorrect term.

cording to their positions along the beam. S2 was located just in front of the second dipole-quadrupole set where the beam envelope had a broader horizontal extent than it did a vertical extent; hence, S2 was made 5cm by 20cm. S3 was located in the experimental area just behind C2 where the envelope was more uniform; hence, S3 was 5cm by 10cm. S4 was much farther down the beam line, where the beam envelope still had the same horizontal to vertical ratio but was more extended. At this point, limiting the solid angle impinging the MuID limited the breadth of S4; hence, S4 was 13cm by 13cm.

2.5.2 Cerenkov Counters

Three Cerenkov counters were used in RD94 for particle identifcation, labeled C1, C2, and C3. All of these were threshold-type Cerenkovs which basically work as follows: Particles can not travel faster than the speed of light (c) in vacuum but light has different speeds (c_n) for different materials according to the relation

$$c_n = \frac{c}{n}$$

where n is the index of refraction for a given material. When a particle is traveling near the speed of light in a vacuum ($n = 1$), then crosses over into a volume of some material where the speed of light is less than the particle's speed, the particle will emit light at a characteristic angle, dependent on its mass. The particle will continue to give off this light, named Cerenkov light after its discoverer, until the speed of the particle is below the speed of light for that material.

Threshold Cerenkov counters are basically switches that turn on when a particle's speed is above some threshold, determined by the type and density of the medium. Since all particles measured during a particular run have the same momentum, the "speed" switch can be interpreted as a "mass" switch. If the particle did not have sufficient speed to make Cerenkov light, then it was too massive. Since all three Cerenkovs in RD94 used a gas medium, we can discuss density in terms of the gas pressure. The relationship for threshold momentum and pressure is

$$p_t = \frac{m}{\sqrt{2\delta_0}}\sqrt{\frac{P_0}{P}}$$

where p_t = threshold momentum (GeV/c)

m = particle mass

δ_0 = n-1 (index of refraction at reference pressure)

P_0 =reference pressure

P = pressure.

The thresholds of each of the Cerenkov counters were controlled by the type of gas and amount of pressure. C1 and C3 used Freon-12 and C2 used N_2. Table 2.1 lists the pressure settings for each of the counters as a function of pressure. Pressures were checked or adjusted prior to each run accordingly: C1 was intended to separate protons from everything else, hence its pressure was set low so that everything but the heavy proton fired it. C2 was intended to distinguish electrons and positrons from everything else. Hence C2's pressure was set high. Logically, muons and pions were those that fired C1 but not C2. C3 was designed to help partially distinguish muons from pions. If a pion decayed to a muon in flight after passing the first start counter, three things could happen: (1) it could decay in the forward direction, and the decay muon would then have a slightly higher momentum than its parent. This we would simply call a muon and assume it had been a muon all along; (2) the pion could decay at some large transverse angle, so large that the decay muon would not strike all the

Table 2.1: Cerenkov pressure settings.

	c1(PSIA)	c2(in Hg)	c3(PSIG)
1	15	0	15
1.5	55	0	38
2	55(30 for μ run)	0	15
3	55	0	-1
4	50	0	35
5	50	-1.5	35
6	50	-3.5	35
7	50	-9.5	35
8	50	-15.5	35
9	50	-21.5	35

start counters – most often missing S4; or (3) it could decay backwards, giving the decay muon an energy approximately 57% that of its parent. C3 was tuned to help separate the full-momentum muons from these low-momentum muons that arise from backward decayed pions[Cornell94].

2.5.3 Veto Counter

In addition to the positive-signal detectors, such as the start counters and the Cerenkov counters, we employed a negative-signal detector (a charged particle veto) to reduce the probability of multiple particles striking the MuID in the same event. It was composed of 8, 60cm long x 22cm wide plastic scintillating slats. Pairs of these slats were doubled-up and placed laterally around the hole, wide side facing upstream. Each slat was composed of plastic scintillator with single PMT readout optically coupled through a triangular wave-guide. The Veto covered an area of 60cm x 60cm normal to the beam axis with a 13cm x 13cm hole through which the beam passed. It was not used in the event trigger, rather, signals from the Veto were slaved for off-line analysis.

2.5.4 Muon Taggers

Three sets of muon "tagging" detector planes were placed downstream of the MuID in tandem to identify muons during high momentum runs. All were composed of plastic scintillating slats with dual-PMT readout. The first two detectors (looking downstream), denoted M1 and M2, were segmented horizontally and vertically by 10cm and fully covered an area of 110cm by 110cm with 1cm thick slats. Both M1 and M2 were constructed identically. M3, located farthest downstream, had only 9 horizontally oriented slats, 15cm tall, 96cm long and 5cm thick, covering a total area of 96cm x 135cm. Due to the lack of electronics, only the horizontal portions of each were used in the event trigger; the vertical portions of M1 and M2 were slaved for off-line analysis.

Between each of the taggers was located an 18-ton, 1m thick block of steel for particle absorption. The intent was to identify muons by their range and bias against pions, especially those that punch through the MuID, by increasing the probability of showering for the pions. Muons and pions lose 1GeV ($\langle dE/dx \rangle$) per $4.87\lambda_I$ of iron, but pions have an additional probability of hadron showering ($\propto 1 - e^{-x/\lambda_I}$). After $8.3\lambda_I$ (the thickness of the MuID), a 3GeV muon has a 99% chance of surviving past M1, but a pion only has 0.001% chance of reaching M1, intact. As momentum increases, the probability of pions reaching successively deeper taggers, exponentially decreases, improving muon-pion separation in the on-line trigger system.

Below 3GeV/c, the taggers were not used in online particle identification. For 3 and 4GeV/c runs, M1 was used in the online trigger, for 5 and 6 GeV/c runs M2 was used and for higher momentum runs M3 was used. In this manner, we could successfully distinguish muons from pions to better than 1% accuracy.

2.6 The Event Trigger

The Event trigger is an electronic logic pulse that flags the event for subsequent storage and monitoring. The pulse comes from a series of checks and comparisons whose outputs confirm or reject the event as a suitable candidate for analysis. All of the signals originate from detectors in the path of the beam, with the exception of the "In-Spill" signal. The In-Spill tells the system that the AGS is on, which minimizes the possibility of events originating from other sources such as cosmic rays. All of the detectors upstream and downstream of the MuID fed logic signals to the trigger from their discriminated analogue pulses with the following exceptions: the Veto, C3, and the vertical portions of the downstream muon taggers, M1and M2.

Figure 2-15 shows the schematical overview of the operation of the event trigger with an accompanying logic diagram of event sequence. The trigger is composed of two levels, primarily for timing purposes. Data signals from the MuID are fed into the 6 Lecroy 96-channel ADCs that require a 40ns lead time before digitization can start. Signals coming earlier than 40ns after gate pulse have their leading edges truncated. The detectors that made up the first level counters are all those counters upstream of the MuID: the start counters and the cerenkov counters, whose signals traveled via fast signal cable to the trigger. The second level trigger was made up of all the downstream counters: the taggers. Their signals arrived at the trigger long afterwards, through the much slower RG-58 coax cable, the same type and length that the MuID signals themselves traveled along. The signals from the MuID at the digitizers before the second level trigger confirmed that they were to be accepted. If it happened that the second level trigger did not confirm, then digitization was stopped and cleared and the trigger was reset.

A brief description of the trigger's logical sequence follows: When the level 1 condition is met, two signals are immediately issued: one to set a BUSY latch to

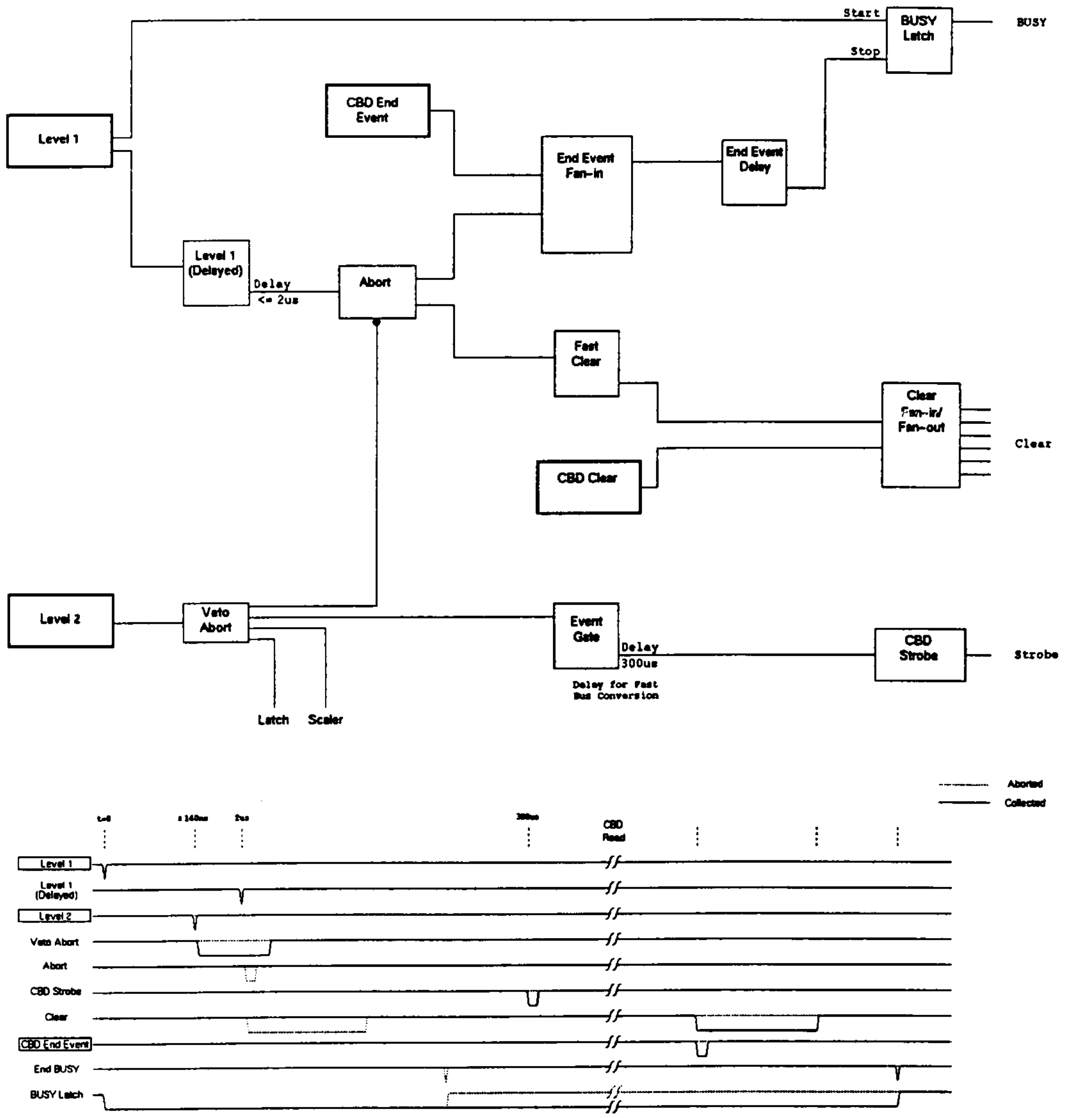

Figure 2-15: Schematical overview and logic diagram of the event trigger.

prevent any other level 1 signals in the system, and one to abort the event. The abort signal is delayed for $2\mu s$ to allow the level 2 signal to stop it. If the level 2 signal is made, it blocks the abort and issues a signal (delayed $300\mu s$ to ensure completed digitizations) to the data acquisition system to fetch the event. After fetching the event, the DAQ sends out two signals, one to reset all digitizers and one to clear the BUSY latch. At this point the trigger is ready to accept new events. See appendix D for the detailed schematics of the trigger circuit.

2.7 Data Acquisition

Intimately connected to the event trigger is the data acquisition system(DAQ). The DAQ basically is the system which takes all the data from the digitizers and stores it and makes it available for on-line monitoring. The primary driver for the DAQ[8] used a Motorolla 167 (MC68040 processor) with OS-9 as the operating system in VME architecture. The acquisition program has three major control features: an event "fetcher", and event "recorder", and an "intercom" (see figures 2-16 and 2-17). The fetcher reads all of the event records via the CAMAC Branch Driver (CBD 8210) from the daisy-chained electronics crates (2 CAMAC crates and 1 fast bus crate) and writes the events to a buffer. The recorder reads the event from the buffer and writes it to tape. The buffer can be thought of as "circular" since events that are written to it always go to the bottom, thus cycling the memory. The intercom passes control information between the main engine (OS-9) and run control processes. Another role of the recorder is to send events to the monitoring system. This is a low-priority role of the recorder so as to minimize down-time and missed events.

The monitoring system was LabVIEW 2 running on a Macintosh Quadra computer

[8]Initial design by Sean McCorkle, BNL; Modification for RD94 by Xiaochun He, UTK.

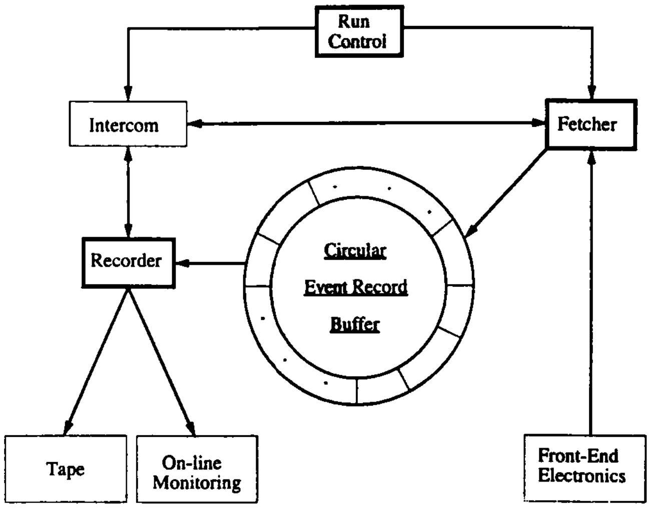

Figure 2-16: DAQ **software schematic.**

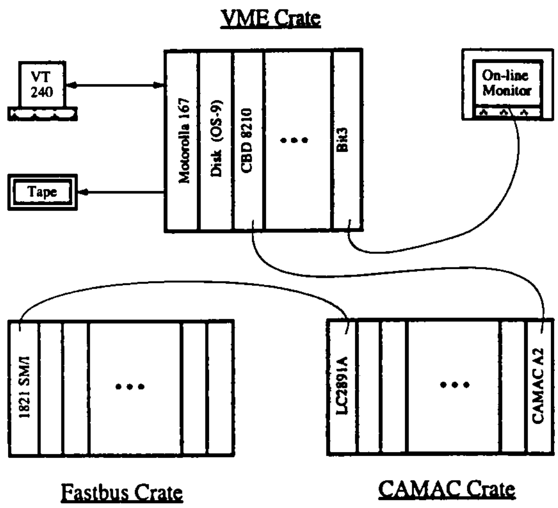

Figure 2-17: DAQ **hardware layout.**

coupled to the recorder through a BIT3 card and a VIC8250. LabVIEW works well for small numbers of parameters (channels) but in our case, where the event record was well over 1000 parameters, it was too slow to monitor data acquisition effectively.

2.8 Data Runs

RD93/RD94 studied MuID response to four particle types, including muons ($\mu^{\pm}$), pions ($\pi^{\pm}$), electrons ($e^{\pm}$), protons (p)[9] and an all-encompassing "Min-Bias" or "raw-beam" over a 1-9GeV/c momentum range, with two capacitive pickup geometries. Tables 2.2 and 2.3 list all successful data runs. Significantly more runs were taken in RD94 than in RD93 with both pad and strip readout geometries. Nearly all the integer momenta were studied with strips and all but three were studied with pads. Moreover, in nearly all cases, both positive and negative polarities were studied, rather unlike the RD93 data set where only one polarity was obtained. In addition, the data runs taken in RD94 were considerably longer. In RD94 we targeted 50K events as a full run, whereas in RD93 we targeted 20K. Appendix C lists the relevant event quantities along with run statistics.

[9] Antiprotons p^{-} were not studied because they make up a very small fraction of the total beam.

Table 2.2: Data Runs with Strips Installed.

Momentum	RD93					RD94				
	Trigger					*Trigger*				
(GeV/c)	*Min-Bias*	*p*	π	μ	*e*	*Min-Bias*	*p*	π	μ	*e*
1.0	□				□	□	□			□
1.5					□	⬓	□	⬓		⬓
2.0	□	□	□	□	□	⬓	□	⬓	⬓	⬓
3.0	□	□	□	□	□	⬓	□	⬓	⬓	⬓
4.0		□	□	□	□	□	□	□	□	□
5.0						□	□	□	⬓	□
6.0	■	□	■	■	■	⬓	□	⬓	⬓	⬓
7.0						⬓	□	⬓	⬓	⬓
8.0	□	□	□	□	□	□	□	□	□	□
9.0						⬓	□	⬓	⬓	⬓

□ Positive polarity.

■ Negative polarity.

⬓ Both positive and negative polarity.

Table 2.3: Data Runs with Pads Installed.

Momentum	RD93					RD94				
	Trigger					*Trigger*				
(GeV/c)	*Min-Bias*	p	π	μ	e	*Min-Bias*	p	π	μ	e
1.0	□					⬓				⬓
1.5	□					⬓			■	■
2.0						⬓	□	⬓	⬓	⬓
3.0						⬓	□	⬓	⬓	■
4.0	□	□	□	□	□	⬓	□	⬓	⬓	⬓
5.0										
6.0						⬓	□	⬓	⬓	⬓
7.0										
8.0	□									
9.0						■		■	■	■

□ Positive polarity.

■ Negative polarity.

⬓ Both positive and negative polarity.

2.9 Simulations

In order to properly design a particle detector, estimates of its response should be known beforehand to ensure that the measurements fall within the range of the measuring device. Analytical approaches to estimating nuclear and atomic processes are not sufficient because they do not incorporate all the random fluctuations akin to physical processes. With the advent of computers, large numbers of calculations can be made that include statistical "monte carlo" fluctuations that more realistically predict physical events. GEANT is one of the more widely used codes for detector development primarily because of its ability to determine detector response down to nearly atomic-physics levels. New versions are often released: the version presently available is 3.21[GEANT]. PHENIX uses GEANT as the basis for its development code PISA and so GEANT was also used to study RD94.

The versatility of GEANT is evidenced by the broad range of particle energy that can be simulated. A broad range of possible energies implies that many physical processes are represented in the code. Energies for electromagnetic processes can be as low as 10keV or as high as 100GeV; 10TeV for muonic interactions. Hadronic interactions can be simulated by one of two different codes incorporated into GEANT, namely GHEISHA or FLUKA. These codes are primarily particle generators and virtually any energy for which there is known data can be simulated. Results for energies outside the range of existing data can be extrapolated from systematics. Cross-sections for all known electromagnetic processes are reproduced from systematic fits to existing data. For hadronic events in GHEISHA, cross-sections are based on pion and proton data and above 2GeV the general law

$$\sigma(A) = 1.25 \times \sigma_{tot}^{Proton} \times A^{4/3}$$

is used.

The code abides by the following general algorithm. First a particle is fetched that is to be tracked through a particular medium and the code decides how many interaction lengths the particle will travel. The distance to the next interaction point is evaluated by multiplying the number of interaction lengths by the inverse of the macroscopic cross-section for each of the possible processes. The minimum of these then determines the distance the particle will be transported as well as the next interaction to take place. The particle will move along a straight path to the interaction site, or along a helicoidal path if a magnetic field should be present and the particle is charged. The final state of the process is then generated. If the particle survives the interaction, the number of interaction lengths to the next process is decided and so on until the particle does not survive or it leaves the boundaries of the experiment. If the particle does not survive, the next particle is fetched. If secondaries are produced, they are stored and tracked in turn. This is a feature which allows showers to be modeled which is essential for the present work.

Two of the more attractive features of GEANT is the simplicity of its geometry and drawing packages. Detectors are easily defined through calls to appropriate subroutines that define the material the detector is made of and its size. New materials can be defined or standard materials already stored in GEANT can be used and magnetic fields can be defined through each material. Many sub-nuclear particles and ions are defined and so can be used as incident particles but just as with materials, the user is free to define new particles. GEANT also comes with interactive version where detectors can be displayed to view their orientations, locations, and dimensions. Moreover, particles can be launched and the response of the detector can be viewed. Figure 2-18 shows a simulated pion striking the RD94 MuID.

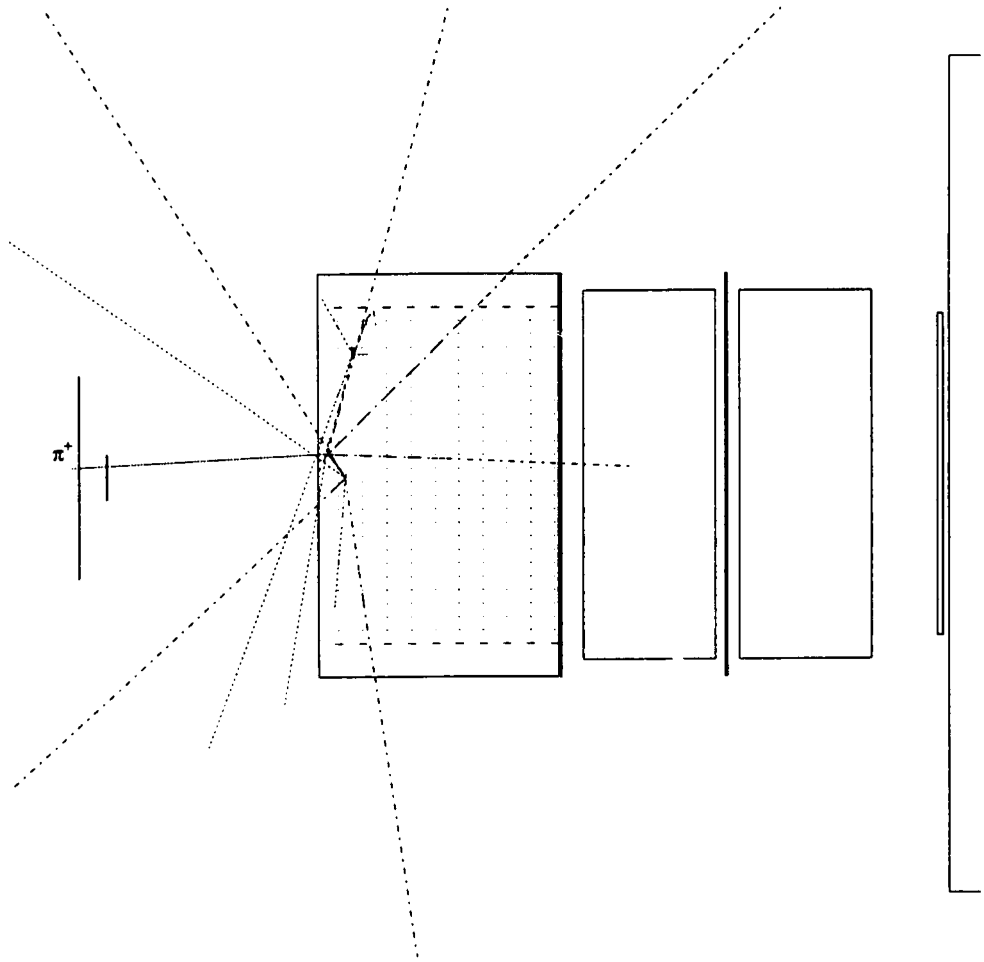

Figure 2-18: A GEANT simulation of a 2GeV pion striking the RD94 MuID.

Chapter 3

Data Analysis

3.1 Pedestal Subtraction

The first step in measuring the response of the entire MuID is to inspect the individual signals coming off the readout strips or pads, not only to verify their proper operation, but to establish the noise levels, otherwise known as pedestals. Appendix B describes the details of subtracting and suppressing the pedestals but a brief summary is in order here.

When the mean of the signal is several standard deviations (of the signal) above the noise, separating them is easily done by subtracting the mean of the noise and suppressing signals between the mean and a multiple of the standard deviations of the noise. Every signal above that point is accepted as a "hit". In the RD94 MuID pedestal subtraction is made complicated be the fact that the signal and the noise are very close to one another. Factors affecting the measurement include improper timing of the ADC gate, un-optimized gate width, non-uniform cable lengths among the MuID channels, poor coupling of the capacitive pickup to the LST, and cable irregularities. Another factor that would cause the signal to "shoulder" the noise, is that

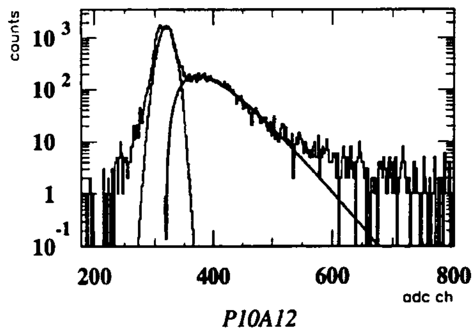

Figure 3-1: An example of fitting the pedestal and signal with gaussian and poisson curves, respectively. The intersection is considered the optimum threshold to distinguish signal from noise.

the pickups are sensitive to neighboring streamer production sites. The strip directly above a streamer may see its full strength; the neighboring strips would get a smaller amount of the image charge, the amount would depend on how far away the strip is from the streamer. Hence, a more sophisticated method of subtraction/suppression needs to be employed.

Briefly the method works in three steps. The first step is to measure the out-of-beam pedestal and fit it with a gaussian. The next step is to fit the in-beam pedestal and signal with a dual gaussian. These measurements provide starting points for the third measurement which is to subtract the in-beam gaussian from the data and fit the remaining portion of the data with a poisson curve. The poisson curve was chosen because the distribution of charge of streamers appear to possess a poisson distribution. This is done several times, each time using a different gaussian with a width and mean between those of the in-beam and out-of-beam pedestals. The remaining distribution is fitted with a poisson. The poisson with the best fit, as determined by the minimum χ^2, and the corresponding gaussian are chosen to define the threshold between data and noise. See figure 3-1. The threshold that is selected as the one to best separate data from noise is then the intersection, although a range about the intersection can be established via

$$\frac{poisson(x) - gaussian(x)}{poisson(x) + gaussian(x)}$$

which defines a range between -1 and +1. A value of +1 is obtained when the gaussian function is very small and limited to values of x greater than the gaussian mean. A value of -1 would be at the null point of the poisson which is equivalent to the mean of the gaussian. A value of zero defines the intersection which is always used for the following analysis.

3.2 Particle Identification

As discussed in section 2.5.2, the RD94 Experiment was designed so that several different particle species could be individually identified and selected while taking data. The particle identification system was not, however, designed to be 100% efficient, since a too-rigid system might bias against certain classes of particles. Instead, the online PID system was relaxed some which leads to misidentification and degraded response of the MuID. To correct for this, a significant portion of data analysis time is spent re-identifying the incident particles.

Several momentum-dependent techniques help define particle types. At low momenta (1GeV/c< P < 3GeV/c), particles are quite easily differentiated by their time-of-flight (TOF). At each momentum studied, Cerenkov counters play an important role, and at momenta higher than 3GeV/c, the detector arrays downstream of the MuID help distinguish between muons and pions.

3.2.1 Time of Flight (β) Measurement

If we know the time difference of an object crossing two particular points (Δt), and we know the distance between those points (Δd), we can calculate the object's average velocity(β) with respect to the speed of light ($\beta = \Delta d / c\Delta t$). If we know the object's momentum(P), we can determine its mass ($P = m\beta\gamma$) and if we know the object's mass, we consider it identified. This is the basis of particle identification using time-of-flight information.

In the RD94 experiment, we used three detectors to measure the TOF. These are the start counters which are placed along the beam line in tandem, with known positions. As a charged particle travels along its trajectory, ~~it~~ must strike all three start counters in order to be registered as a candidate particle for study. When each of the detectors is hit, the time is recorded with respect to one of the counters that was selected to be the overall start time for the event, time zero (t_0), and we obtain three sets of time and position information. The times (Δt) and the detector positions composed the time-of-flight data. The trajectory of the particle after it registers a hit in the first start counter (S2) carries it through a bending magnet and a focusing magnet. From there the particle travels essentially a straight line and maintains a fairly constant speed[1]. For each event, we may fit the space-time data to a straight line whose slope is the β of the particle. Further details of the calibration and calculation process can be found in appendix A.

The results are that protons are the most clearly defined particle due to its relatively heavy mass and slow speed for a given momentum. The timing measurements are accurate to within 2% and the widths of the proton peak at several momenta indicate that momentum spread is below 5% of the beam momentum. Heavier

[1]Gravitational deflection is on the order of a tenth of a micrometer and kinetic energy loss is about 220keV/m through air and about 1MeV/cm through the plastic scintillator of the start counter implying a several GeV/c particle takes an essentially straight path at constant velocity.

species, such as deuterium or helium begin to appear at higher momenta but with very small peaks. The lighter species are merged together, even at the lowest momentum, 1GeV/c, but electrons can be somewhat distinguished from the muon-pion peak.

The measurement yielded an anomalous feature seen both in the calculation of β and, more significantly, in the raw data. Satellite peaks were observed on both sides of the velocity, (higher and lower velocities) of the proton on all low momentum runs. The means of the peaks scale with the momentum and have a gaussian shape. As tighter restrictions are imposed on the fit of the data, the peaks do not disappear, they, in fact, sharpen.

The first guess in solving this anomaly was to check the method of calculation. However, the peaks appeared in the raw spectra, before any calculation was performed. Also, they increased with increasing momentum. These are two prime indicators that the peaks are physical and not results of errors in the method. Lastly, we placed cuts on these timing peaks and observed the MuID's response to them and they appear to have a response close to that of protons. The next place to look for a solution is the hardware. A jitter in the timing circuit would produce satellite peaks, however, one would expect to find them around other particle peaks, not only the protons.

Exactly what is causing the peaks is not known. We can not give an explanation as to why they form nice sharp peaks both above and below the proton peak. Our guess is that the satellite peaks are caused by protons since 1) the peaks disappear when the beam polarity is switched to negative and protons are no longer focused and 2) the response in the MuID is similar to protons. It may be that the valleys between the peaks and not the peaks themselves are the anomalies. If this was the case, then the proton peak would then be wider so as to include the satellites. Our estimates of

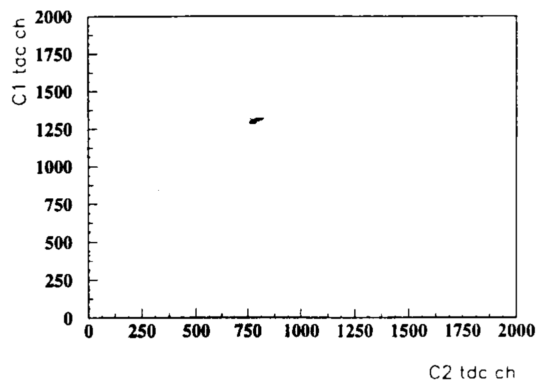

Figure 3-2: Two-dimensional histogram of C1 TDC vs. C2 TDCs. The diagonal line indicates C1 and C2 were hit within $\Delta t \approx$ 150ns.

momentum spread would widen accordingly.

3.2.2 Cerenkov Counters

The three threshold Cerenkov counters were arranged in tandem to identify charged particles by whether Cerenkov light was given off as they traversed the medium of the counter. The threshold of C1 was set low to separate protons from lighter particles. The threshold of C2 was set high to separate electrons from heavier particles.

The usefulness of C1 and C2 can be shown in one two-dimensional histogram obtained from a 1.5GeV/c raw beam run. In raw beam runs, all charged particle species are accepted, so superimposing all events from a raw beam run will show the effects of all particles in the beam. The relatively heavy proton should not register a hit because it was too slow to emit Cerenkov light for all of the established thresholds.

Figure 3-2 shows the two dimensional projection of the timing information from C1 and C2. The diagonal line indicates when a particle fired both Cerenkov counters. These particles are electrons. In the opposite polarity case we would have positrons. If other particles fired both counters, they too would show up but along different diagonals. The horizontal line indicates when a particle hit C2 and missed C1. C1 then "times out" and gives a constant value where C2's time varies due to the spread in beam momentum. These particles are the muons and pions.

Since pressures were adjusted in each of the Cerenkovs with changing momentum runs, the discriminating power of each was maintained. Hence, once the timing cuts were defined, they can be used for all momenta.

The C3 counter was designed[Cornell94] to distinguish muons that emanate from two different sources. What is meant here by "source" is not so much *what* created it, but *how* was it created. Muons in the beam are predominantly decay products from pions and, to a lesser extent, kaons. There are other sources (other *whats*) such as dilepton production from the the Drell-Yan process (time inverse process of that shown in figure 1-1), or weak interactions such as $e^+e^- \xrightarrow{Z^0} \mu^+\mu^-$ but these are negligible compared to pion decay due to low beam energy.

C3 was primarily designed to distinguish muons at full beam momentum from muons that decay from pions in the *backward* direction in the pion rest frame. The backward muons have approximately 57% of the beam energy and give off significantly less Cerenkov light than full momentum muons or pions. However, in the RD94 arrangement, most of these backward muons will not be focused into the experimental area because the second bending magnet will keep them out of the envelope. Thus, it is only those pions that decay to muons *when* they were between the second bending magnet and S4 that may be candidates for rejection. The problem is made difficult by the fact that pions decay to muons all along the trajectory, so backward muons will have a range of beam energy from 57% to 100%. The problem is made even more difficult by the fact that horizontal and vertical extents of the beam envelope are not symmetric: the vertical extent is broader, hence there will be broader spread in decay muon energy. Because of these arguments, the C3 counter did not operate efficiently to separate full from low momentum muons. The counter became, in effect, a second electron identifier.

3.2.3 Muon Taggers

The muon taggers were primarily used for on-line triggering to define muons. In off-line analysis, they can be used to help define pions at high momentum. At low momentum (<3GeV/c), very few pions penetrate the MuID. Above 3GeV/c, pion shower products can penetrate the MuID and register hits in the taggers. As momentum is increased, so does the number of shower secondaries that reach the taggers as does the depth of of their penetration. Hence, for high momentum runs, we can define pions as events which either have no hits (due to early showering which we expect to be the case most of the time) or many hits (which we expect will be due to penetration of shower secondaries) in the muon taggers. Figure 3-3 shows the multiplicities (product of horizontal hits and vertical hits) in M1 and M2 for an 8GeV/c muon run. To be called a muon at this high momentum, a hit (one or more) was required in M3. Most of the pion shower products will not make it back to M3 at this momentum but there there are a few, evidenced by the small shoulder in M1 at multiplicity ≈ 6. Note that there are few events in M2 with large multiplicities (>4 hits).

3.2.4 Beam Profile

With particle identification techniques in place, we can now measure the profile of the beam: the fraction of the beam that is made up of the various particle species. Figure 3-4 shows the beam profile for positively charged particles as measured with the beam defining detectors upstream and downstream of the MuID. For momenta at and below 5GeV/c, time-of-flight and the cerenkov counters were used to define

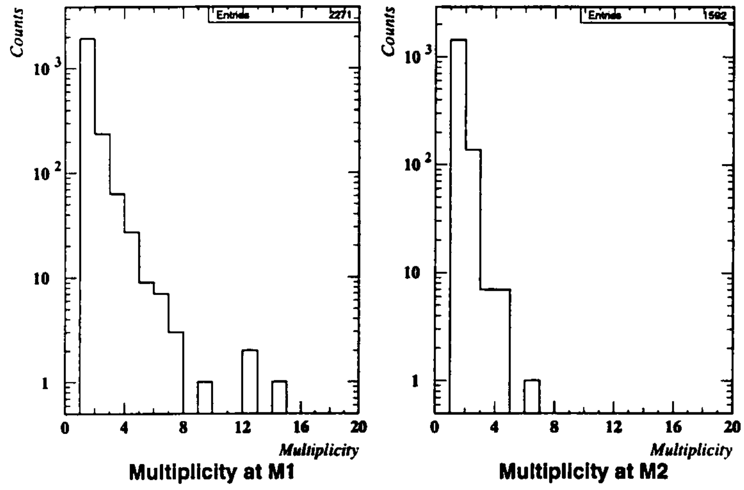

Figure 3-3: Multiplicities (defined as the product of the horizontal and vertical slats hit) at M1 and M2 for an 8GeV/c muon run. One hit is required at M3 at this high momentum to define a muon.

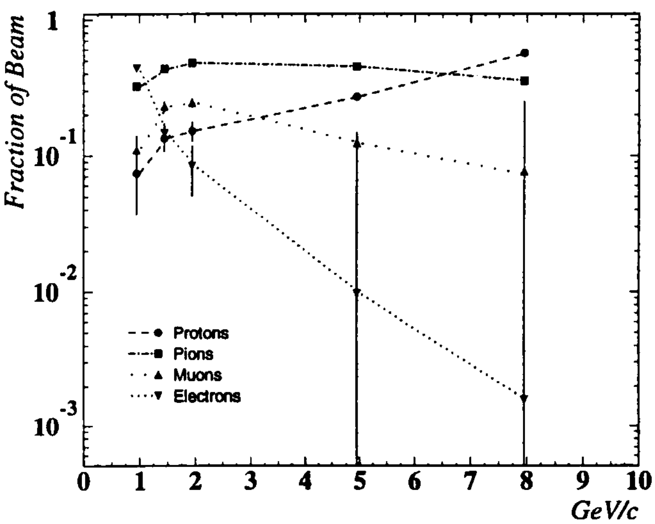

Figure 3-4: The beam profile measured with the beam defining detectors upstream and downstream of the Muon Identifier. The fraction of the beam that is muons is determined by discriminant analysis techniques using data from the Identifier.

protons, pions, and electrons. Above 5GeV/c, the cerenkov counters and the taggers were used. Muon-pion separation was made with discriminant analysis with data from the MuID 3.3.

3.3 Separating Muons From Pions: Discriminant Analysis

Since no detector system was employed which efficiently identified muons and pions throughout the momentum range studied, other than the prototype MuID under test, we are forced to use analytical techniques with information from the MuID itself to separate them. For several years, the ORNL HERG, in association GSU, studied discriminant functions with the intent of optimizing muon-pion discrimination with a highly segmented calorimeter.

3.3.1 Theory of the Discriminant Analysis Function

The basis for the the discriminant function used in this analysis has it roots in multivariate analysis[Hand81] and pattern recognition[Coomans86]. The object of building this technique is to understand how to best separate classes of objects, with fewest mistakes. The analysis here falls under what can be termed "supervised" pattern recognition, where a set of knowns (data training set) help decide what the unknowns (data analysis set) are. Furthermore, the technique is also classified as deterministic, as opposed to probabilistic — decisions place objects in one of a determined set of classes instead of weighting them according to some probability scheme. Lastly, the number of classes is fixed at two and all outcomes must fall within one of them. No allowance is made for new classes to appear or for results to be "outside" the bounds of the two classes.

With this method, one begins by establishing probability distributions ρ which are based on functions derived from physical observations x. For instance, a muon deposits 1GeV of energy every $\langle x \rangle \approx 4.9\lambda$. Due to fluctuations, a large set of 3GeV muons would then come to rest at about $14.7\lambda_I$, with a landau distribution that we may approximate as gaussian with spread (σ). This distribution $f(x)$ is the function and the physical observation is the depth or range of penetration.

$$f(x) = Ce^{-\frac{1}{2}(\frac{x-\langle x \rangle}{\sigma})^2}$$

When more classes of objects are included, for example muon and pions, we note that the functions f, their means $\langle x \rangle$, and their spreads σ may differ[2] and we denote them with superscripts

$$f^p(x) = C^p e^{-\frac{1}{2}(\frac{x-\langle x \rangle^p}{\sigma^p})^2}.$$

The probability distribution ρ^p is simply f^p normalized to all possible outcomes

$$\rho^p(x) = \frac{f^p(x)}{\sum_{q=1}^{N} f^q(x)}$$

where N is the total number of classes. The functions and the probability distributions then differ only by a constant and are of the same in form. The main difference is that the point at which the functions of two different classes are equal is not necessarily the point at which the probability distributions are equal. Bayes' Criterion suggests that a good algorithm is one that, simply stated, minimizes mistakes. In our case we implement that criterion by including the size of the sample populations in determining the probability distributions.

[2] We are making the assumption here that the distributions of each of the class types is gaussian. This is not true in general but the derivation of this method becomes difficult if this assumption is not made. For most of the physical observations made in this analysis, a gaussian approximation is not a disastrous one.

We can extend this development to multivariate pattern space by including other physical observations ($x \rightarrow \vec{x}$). We directly compare[Stankus94] the 1 and N dimensional cases by rewriting the one dimensional case

$$\text{1 dimensional:} \quad \rho(x) \quad \propto \quad e^{-\frac{1}{2}[\ (x-\langle x\rangle) \quad s^{-1} \quad (x-\langle x\rangle)\ ]}$$

$$N \text{ dimensional:} \quad \rho(\vec{x}) \quad \propto \quad e^{-\frac{1}{2}[\ (\vec{x}-\langle\vec{x}\rangle)^T \quad \Sigma^{-1} \quad (\vec{x}-\langle\vec{x}\rangle)\ ]}$$

and letting $s \rightarrow \Sigma$, where $s = \sigma^2$. If s is the variance of the function in the one dimensional case, then Σ is the covariance matrix and each is defined

$$s \quad \equiv \quad \langle \quad \left(\tfrac{x-\langle x\rangle}{\langle x\rangle}\right) \quad \left(\tfrac{x-\langle x\rangle}{\langle x\rangle}\right) \quad \rangle$$

$$\Sigma_{i,j} \quad \equiv \quad \langle \quad \left(\tfrac{x_i-\langle x\rangle_i}{\langle x\rangle_i}\right) \quad \left(\tfrac{x_j-\langle x\rangle_j}{\langle x\rangle_j}\right) \quad \rangle.$$

If we then know $f^p(\vec{x})$ from the training data of each class of object, we can then know the $\rho^p(\vec{x})$ and $\langle\vec{x}\rangle^p$ and from these, determine the expectation values of each of the matrix elements of Σ^p. If Σ^p is nonsingular, we can invert it to obtain the inverse covariance matrix $(\Sigma^{-1})^p$ and then calculate $\rho^p(\vec{x})$ for any given object (analysis data). Hence, the training data determines the coefficients Σ^{-1} and $\langle\vec{x}\rangle$ which can be used to determine which class a randomly chosen object will belong to.

We now have expressions for the probability densities of each object class $\rho^p(\vec{x})$. For our analysis, we have only two classes of objects ($N = 2$) so we can conveniently define a discriminant function which combines them:

$$df(\vec{x}) = 2 \times \frac{\rho^\mu(\vec{x}) - \rho^\pi(\vec{x})}{\rho^\mu(\vec{x}) + \rho^\pi(\vec{x})}.$$

This is a simple difference over sum which has the effect of normalizing the difference to a small scale, in this case 2. We chose 2 for the scale (fully ± 2) to compare the difference to the average. *df* is then the discrimination function used in the following analysis. For a given object (in our case, the object is either a muon or a pion and is described by a certain set of measurements $\vec{x}$) the calculated $df(\vec{x})$ will then be a number between 2 and -2. A well defined muon will have a value close to 2 and a well defined pion will have a value close to -2.

Emphasis should be made here about the presence of two sets of data: training and analysis. If we have pure sets of training data, we can construct the discriminant function which can be used to determine the class of an unknown particle type. If the individuals in the analysis set are *presumed* to be known, we can measure the efficiency of the how the analysis set was constructed. For instance, high momentum muons and pions were separated at the time data was taken through the use of the muon taggers. A few percent of the pions that showered within the MuID sent shower secondaries into the taggers and were identified as muons. Pions thus contaminated the muon sample. This contamination lowers the trigger efficiency which can be measured with this method. More importantly, the method becomes a tool for separating the data (see figure 3-5).

3.3.2 The Efficiency Measurement

The efficiency measurement that we employ to describe muon-pion separation may be described with an example. For simplicity, let us choose some fictitious measurement which purports to distinguish muons from pions. Let us assume that the measurements provide us with gaussian distributions for both classes, shown in figure 3-6. We may consider these initial distributions to be the training data on which we base further calculations. Each of the probability distributions has a measurable mean $\langle x \rangle^q$ and width σ^q which define the distribution (ρ^q). With known distributions, normal-

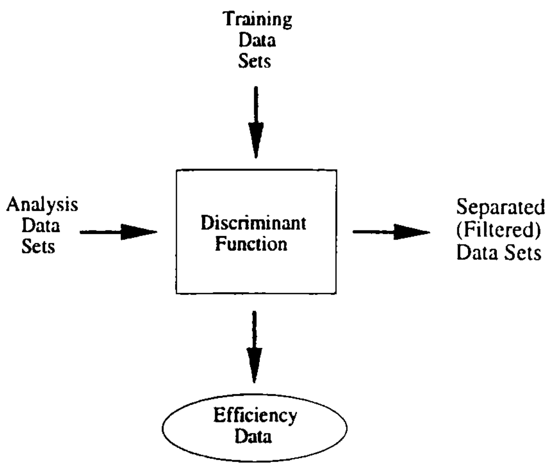

Figure 3-5: Diagram of the discriminant function showing the input training and analysis data sets and the output efficiency measurement and separated analysis data.

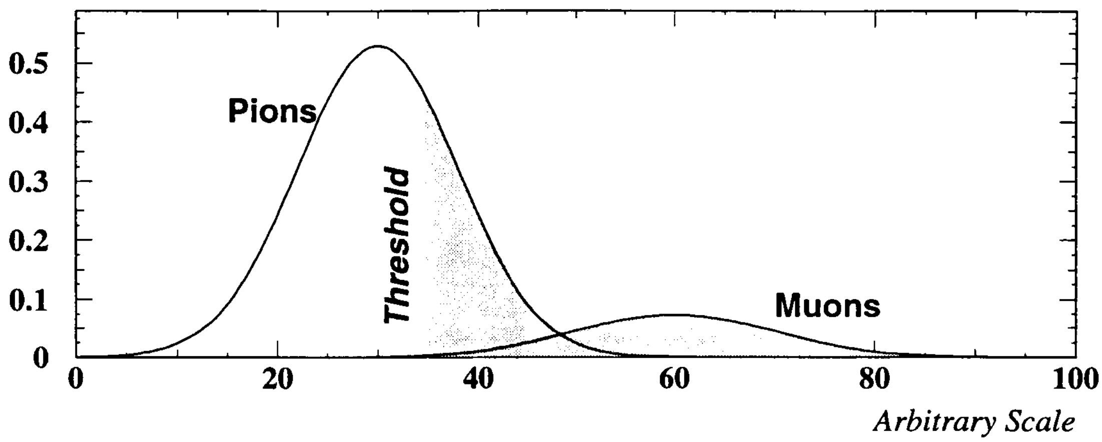

Figure 3-6: Two fictitious probability distributions.

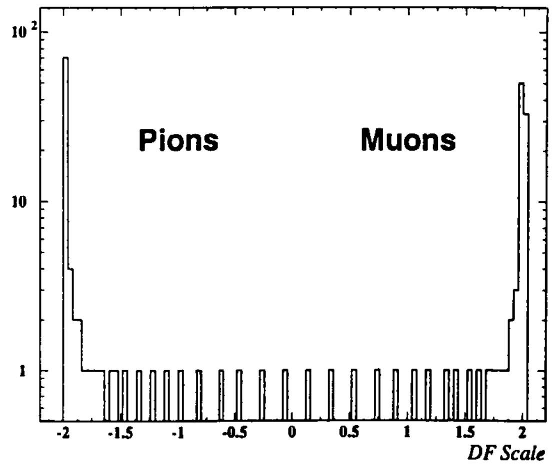

Figure 3-7: Discriminant function based on the probability densities of fictitious probability densities shown in figure 3-6. Because the densities are well separated, the discriminant function peaks are clearly defined.

ized to the numbers of incident particles for both muons and pions, the discriminant function is then determined and we can calculate *df* values for any set of analysis data (the training set may be considered for analysis as well since we now consider individual measurements within the set instead of the set as a whole). Figure 3-7 shows the discriminant function using the training data for analysis. We measure the real muon efficiency by first selecting a particular discriminant cut-off, or threshold, value. Muons, both real and fake are above the threshold; real and fake pions are below the threshold. The efficiency for measuring muons will then be the integral of the muon probability density from the threshold to infinity and the efficiency for measuring fake muons is the integral of the pion probability density, also from the threshold to infinity. The real and fake muon efficiencies are then calculated for each threshold value along the scale (figures 3-8a and 3-8b).

Since we are calculating two quantities (real and fake muon efficiencies) for each threshold value, we recognize that these two calculations form coordinate pairs which

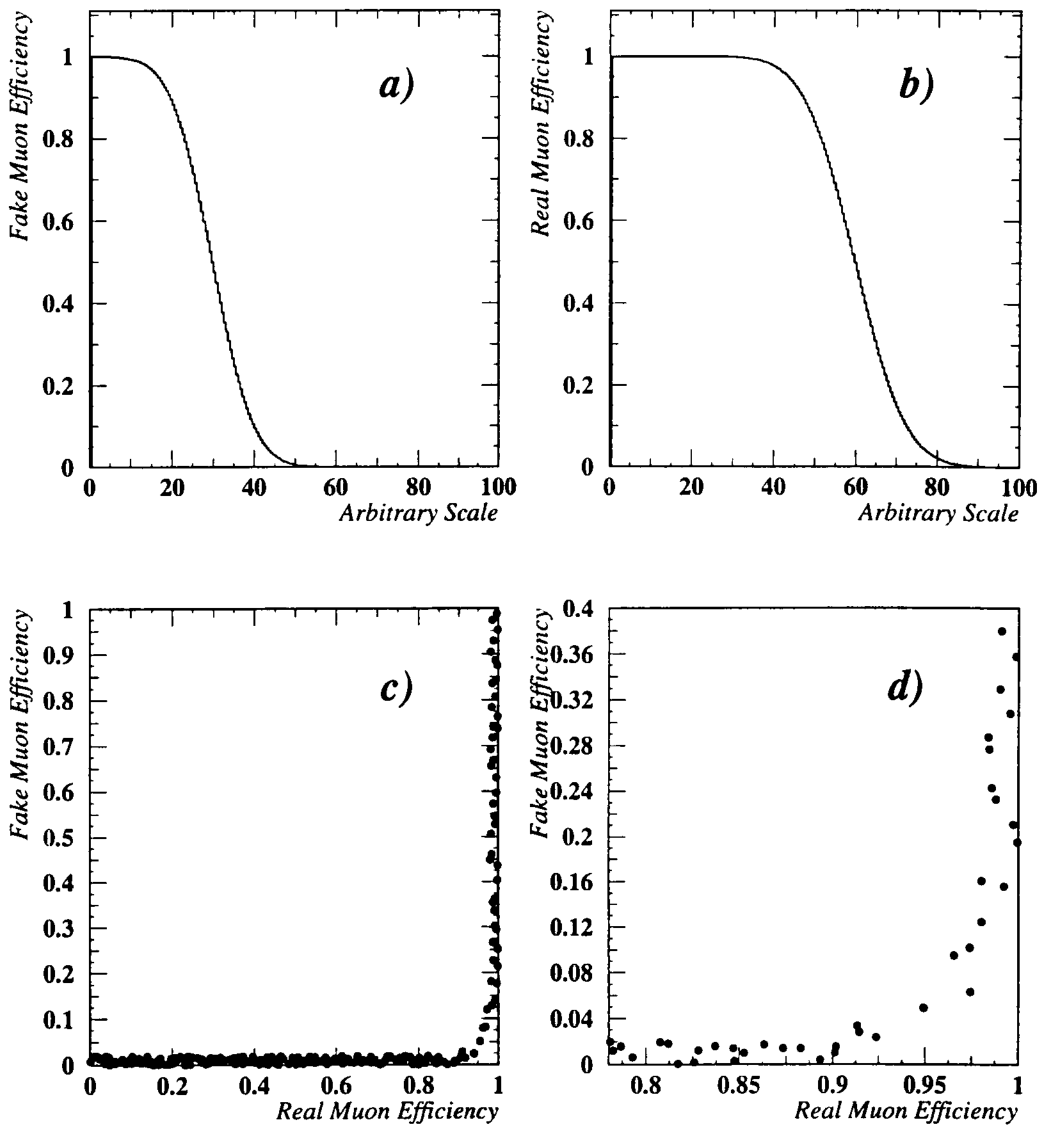

Figure 3-8: Efficiency curves based on fictitious probabilities of figure 3-6. Figure **a** shows the efficiency for finding pions in the muon sample for a given threshold along the abscissa of figure 3-6. Figure **b** is the corresponding real muon efficiency. Both **a** and **b** are calculated by integrating the probability distributions from the threshold to infinity. Figure **c** is the efficiency curve obtained when using the **a** and **b** as coordinate pairs. Figure **d** is a magnification of the lower-right portion of figure **c**.

can be represented on a two dimensional histogram (see figure 3-8c and 3-8d). The bins of the histogram that are defined by all the coordinate pairs then form a curve which give us a good illustration of how the two efficiencies work together. For the remainder of this thesis we will call these curves *efficiency curves.*

To illustrate the dependence of the efficiency curves on the initial probability densities, figure 3-9 shows a study of three cases comparing initial probability distributions and the corresponding efficiency curves. The only difference among the three cases is the mean of the pion probability distribution, which approaches the muon mean. As the pion mean increases, the sharp knee of the efficiency curve relaxes to a bend, showing the increase in fake efficiency for a given desired real muon efficiency.

We need not fill the bins with arbitrary values — we may fill them any single-

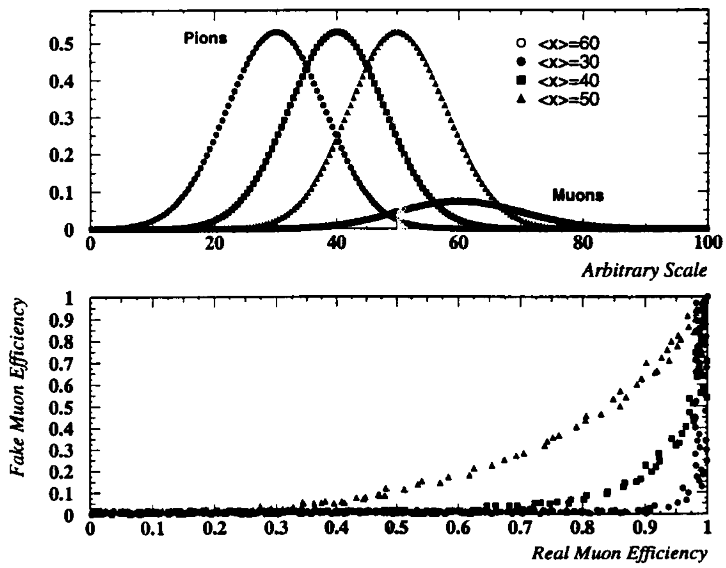

Figure 3-9: A study of the efficiency curves for three cases where one parameter varies. The mean of the pion probability distribution varies from 30, to 40, to 50, while the muon peak stays at 60. The lower figure shows the efficiency curves associated with the upper figure. The markers in the lower figure follow the pion markers in the upper figure.

valued function associated with the real and fake muon coordinates. This will not change the efficiency curve, but enhances it by carrying with it some associated function. Both figures 3-10a and b are similar to figure 3-8c in that the abscissae are chosen by the efficiency coordinates. The difference in the two plots is what associated function fills the ordinate bins (the vertical axis) In figure 3-10a, we fill the bins with the associated scale (0-100).

Through this example, we have have shown that the efficiency curves, measured in this way, provide us with information, not only concerning how the mistakes (fake

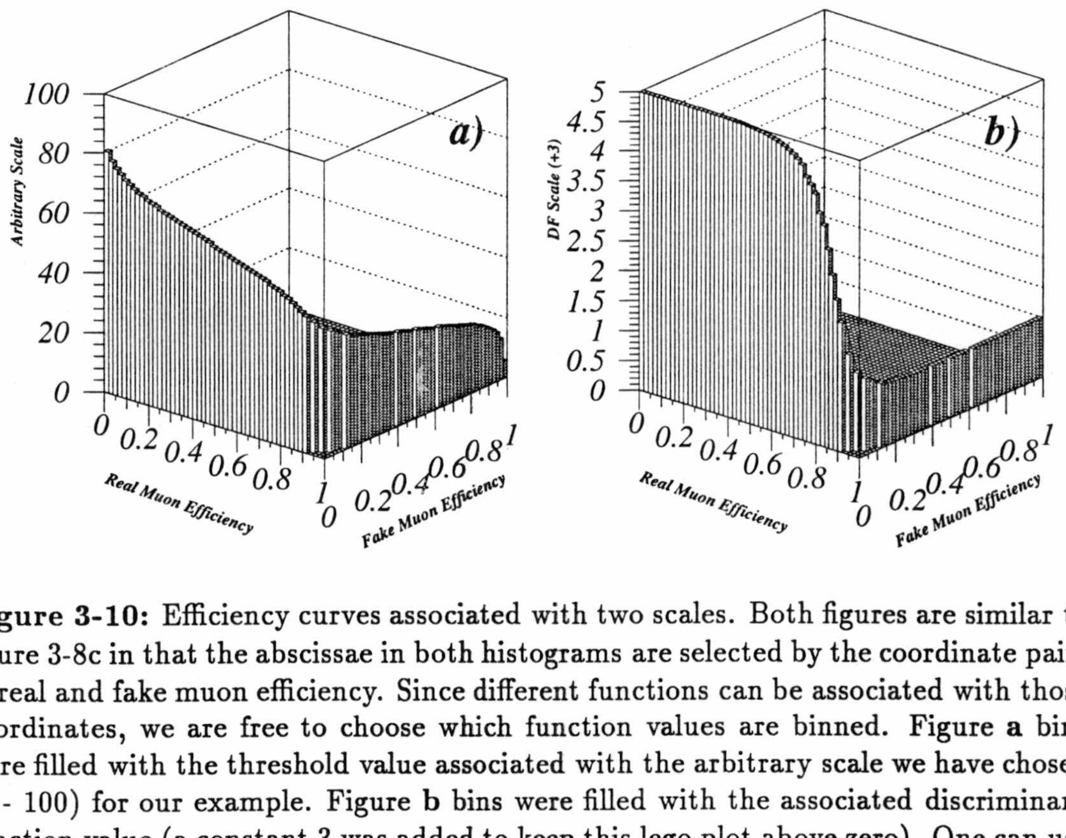

Figure 3-10: Efficiency curves associated with two scales. Both figures are similar to figure 3-8c in that the abscissae in both histograms are selected by the coordinate pairs of real and fake muon efficiency. Since different functions can be associated with those coordinates, we are free to choose which function values are binned. Figure **a** bins were filled with the threshold value associated with the arbitrary scale we have chosen (0 - 100) for our example. Figure **b** bins were filled with the associated discriminant function value (a constant 3 was added to keep this lego plot above zero). One can use these curves to select either the scale value (in **a**) or a discriminant function value (in **b**) by first selecting the desired efficiencies, then reading the corresponding ordinate.

muon efficiency) vary with the literals (real muon efficiency), but how to best decide where to place a dividing line (threshold), based on one's desired level of allowable mistakes or necessary real efficiency. We can now apply this method of measuring efficiency to the MuID and begin to separate real muons and pions. However, at this point, we must decide what measurements to make.

3.3.3 Building the Discriminant Function

With a highly segmented device such as the MuID, one can construct many measurements that may discriminate between muons and pions. For instance, over the momentum range under consideration (1-9GeV/c), pions generally shower within a few λ_I and muons generally penetrate the whole device so we may consider the depth of penetration as one measurement and the width of shower development as another. Likewise, many variables can be constructed from sums, differences, products, or whatever mathematical operation of the pickup signals of the MuID we think will discriminate between muons and pions.

A list of 18 variables was composed (see table 3.1) and studies began with the intent to narrow the choices to as few as possible while keeping the discriminating efficiency high. The studies used data from simulations of the PHENIX MuID which has 6 planes and conical geometry. In the RD94 MuID, the number of variables increased from 18 to 40 for two reasons: the MuID was longitudinally segmented into 10 planes and the horizontal and vertical strip responses varied greatly (see sect. 2.4.2). With four extra planes and splitting the variables into horizontal and vertical components of the original variables, the number of variables easily grows to an unmanageable level. Table 3.2 lists the discriminant variables used in analysis of the RD94 MuID.

As one can see from comparing tables 3.1 and 3.2, most of the variables are equivalent, with the exception of horizontal and vertical partitioning. Two significant

Table 3.1: Original 18 Discriminant Variables.

Variable Number	Variable Name	Description
1	Last_plane_hit	Highest numbered plane recording hits
2	Total_hits	Sum of the hits from all planes
3	Max_plane_hits	Max number of hits recorded in any one plane
4	Plane_ave_hits	Total_hits / Last_plane_hit
5	R_max	Max of $\sqrt{(X_{max} - X_{min})^2) + (Y_{max} - Y_{min})^2)}$
6	RMS_max	Max of $\sqrt{\sigma_x^2 + \sigma_y^2}$ for any plane
7	Total_energy	Sum of all deposited energies
8	Max_plane	Last_plane_hit - plane recording max hits
9	Front_back_ratio	$\frac{\Sigma \text{ hits in 1st 3 planes}}{\Sigma \text{ hits in last 3 planes}}$
10	First_plane_hits	Total hits in first plane
⋮	⋮	⋮
15	Sixth_plane_hits	Total hits in sixth plane
16	Primary_track_ID	Primary particle ID
17	Ptot * $cos(\theta)$	P_z
18	Theta	Theta angle of the launched particle

Table 3.2: RD94 Discriminant Variables. No variable is assigned to number 12.

Variable Number	Variable Name	Description
1(2)	MZH(MZV)	Deepest hor(ver) plane hit (max z)
3(4)	THH(THV)	Total hits in all hor(ver) strips
5(6)	MHH(MHV)	Max number of hor(ver) hits in any one plane
7(8)	APH(APV)	THH/MZH (THV/MZV)
9(10)	EXH(EXV)	Max Extent of hor(ver) hits projected to back plane
11	RMS	Max of $\sqrt{\sigma_h^2 + \sigma_v^2}$ for any plane
13(14)	EQH(EQV)	Deposited Energy: ΣQ on hor(ver) strips
15(16)	MPH(MPV)	MZH - MHH(MPV - MHV)
17(18)	FBH(FBV)	$\frac{\Sigma \text{ h(v) hits in front half}}{\Sigma \text{ h(v) hits in back half}}$
19(20)	H1H(H1V)	Total hor(ver) hits in 1st plane
⋮	⋮	⋮
37(38)	H0H(H0V)	Total hor(ver) hits in 10th plane
39	MOM	Event Momentum
40	PID	Particle ID

changes have been incorporated: the front-to-back ratio has been modified to use the front and back *halves* of the MuID instead of the front or back 3 planes. This is a simple coding change that will have significant usefulness when studying degraded segmentations (section 3.3.7). The other change is the lateral extent of the shower, formerly the shower radius. Instead of simply measuring the horizontal or vertical extent of the shower, we project the measurement back to the last downstream plane. This change was made as a way to include both shower development and penetration depth in one variable. The variable termed the front-to-back ratio is another example of including both aspects in one measurement.

3.3.4 Choosing the Best Set of Measurements

Now that we have what we feel is a somewhat exhaustive list of measurements that may have discriminating power, how do we go about finding the best set? Is there one variable that works just as well as all combined? Does the discriminating power increase with an increasing number of variables? Does it increase with a decreasing number of variables? With these and many other questions and with so many variables to consider, it seems that finding the best set may be so daunting a problem that computation time alone would prohibit a comprehensive study. One of the standard techniques used to find the best set of variables is to find the eigenvalues of the inverse covariance matrix which point to the most efficient parameters. For example, if the inverse matrix is diagonalized, the parameters with the largest values along the diagonal (eigenvalues) will be the ones that most significantly raise (for positive value) or lower (for negative value) the value of the discriminant function. Parameters with small eigenvalues will have little influence. The drawback of this method in our case is that it chooses the parameters for one class (muons) independent of the other class (pions) . The best set that we find for muons may not be a good set for distinguishing pions and the combination may have little discriminating power. In order to effectively study the discriminating power of both inverse covariance matrices together, and keep computation time to a reasonable level we derived a brute-force method based on a set of 40 variables. Since the horizontal and vertical dimensions in the calorimeter are independent and neither is favored, we limited the study to one dimension, horizontal. Next, we chose only those that are constructs, i.e., not those that are simply the number of hits on an individual plane. These considerations reduced the number of variables to a much more manageable quantity of nine. The chosen nine variables are the first nine horizontal variables listed in table 3.2.

With a limited number of variables, we choose to find the best by the brute-force method of checking each subset's calculation "power". We employed two yardsticks to measure this power:

- Adequate: how often the discriminant value is above or below some dividing point (the function minimum) between the extremes, and,
- Best: how often the subset calculates the discriminant value closest to the extreme.

We then construct an algorithm that (1) chooses an event, (2) chooses a subset of the nine variables, then (3) calculates the discriminant value. We present the algorithm explicitly:

From a simulated training data set for a given momentum, we calculate
the covariant matrix elements and discriminant variable averages

  Choose an event from a new data set

    Choose a subset of discriminant variables

      Select the associated covariant submatrices

      Invert the submatrices ($\Sigma^{\mu,\pi} \rightarrow (\Sigma^{-1})^{\mu,\pi}$), building $\rho^{\mu,\pi}$

Calculate the *df*

Keep statistics, how many times adequate, best

Choose a new subset of discriminant variables until exhausted

Choose a new event until exhausted

Choose a new momentum to study

500 events were thus studied with $\Sigma_{i=1}^{9} \binom{9}{i} = 2^9 = 512$ subsets and the results are as follows. First, as a convenient, though possibly complicated-looking device, we resort to the 2-dimensional histogram for display and index the subgroups along the horizontal abscissa. The first bin, index 1, will contain information on variable number 1 when it was the only variable in the subgroup; the ninth bin, index 9, will contain information on variable 9 when it was the only variable in the subgroup; the tenth bin, index 10, moves into the variable subsets of 2, here in index 10 we have variables 1 and 2. This, as one can see, gets complicated trying to remember the subset-index correlation. The easy way to keep it straight is to have the correlation right there on the histogram — this is where the second dimension of the 2-D histogram comes in. Along the vertical abscissa we plot the variable numbers (make it even easier and use their code names), and every time a subset calculates the minimum discriminant function, put a 1 in the bins (vertical abscissa) that are associated with that index (horizontal abscissa). The index numbers then become unnecessary and a more informative way to increment the horizontal abscissa is to label where the divisions of subset size occur, i.e groups of 1 variable, 2 variables, etc. As a guide, figure 3-11 is a display of this device, with all bins filled equally.

The figures in 3-12 show how well groups of 2 parameters calculate the correct discriminant function. For each 500 events studied, if the value of the discriminant function was correct for a particular subgroup — meaning greater than the function

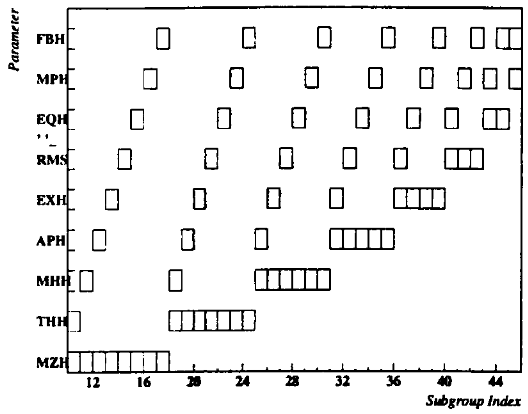

Figure 3-11: Two-dimensional histogram used to illustrate which parameters constitute each subgroup of 2 parameters out of the 9 parameters used in the "Best Parameter" study. Other-sized subgroups are not shown here for simplicity.

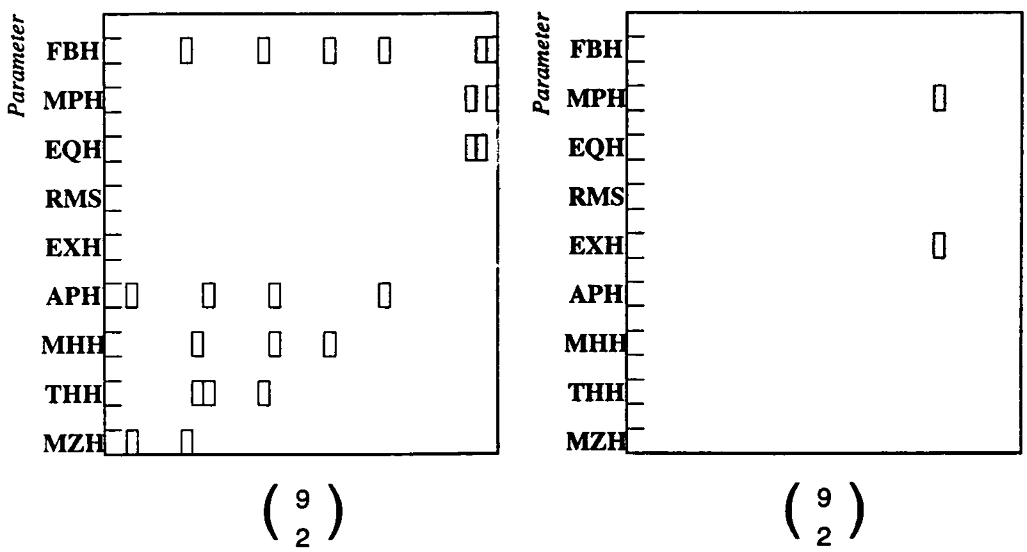

Figure 3-12: Groups-of-2 parameters for adequately measuring 2GeV/c muons(left) and pions(right). The ordinate, designated by the relative sizes of the boxes, was set to a minimum of 498.1. Since only 500 events were studied, the subgroup had to have a "correct" calculation of the discriminant function 499 or 500 times.

minimum for muons and less than the function minimum for pions — then each of the variables associated with that subgroup bin was increased by 1. This measurement we can think of as being adequate in that it calculates the discriminant value to be on the correct side of the function minimum, but not necessarily close to the extreme. From the figures 3-12, one sees that there are several groups (of 2) that calculate the discriminant function with high efficiency for muons but only one high efficiency group (of 2) for pions. Also note that that one high efficiency group for pions is not a high efficiency group for muons. For other sizes of subgroups, the pattern is similar in that many groups are highly efficient for one particle type but not for the other, meaning that we need another way to look for the best set.

We might also consider which group calculates the best value for the discriminant function. If the ideal muon has a value of 2, and the ideal pion has a value of -2, we may ask which set yields values closest to those extremes. Figures 3-13 reveal the sets that have the best calculation (closest to the extreme) for muons and pions. Note that for muons, one variable, by itself, has the best value most often: the front-to-back ratio. For pions, several subgroups seem to do well. Since most of the subgroups that do well for pions are sub-subgroups of the largest one (a group-of-5), and because the one group that does well for muons is also part of that subgroup, it was determined that the group-of-5 would be used for muon-pion discrimination, namely MZH, EXH, RMS, MPH, and FBH (see table 3.2 for explanation of abbreviations).

3.3.5 Analysis of μ, π Events

The data runs taken in RD93/RD94 (see tables 2.2 and 2.3), included muon and pion triggers. At high momentum, the difference in the triggers was the simply hits in a particular muon tagger (which tagger was used depended on the momentum). The muon trigger required a hit in a tagger while the pion trigger did not. At low

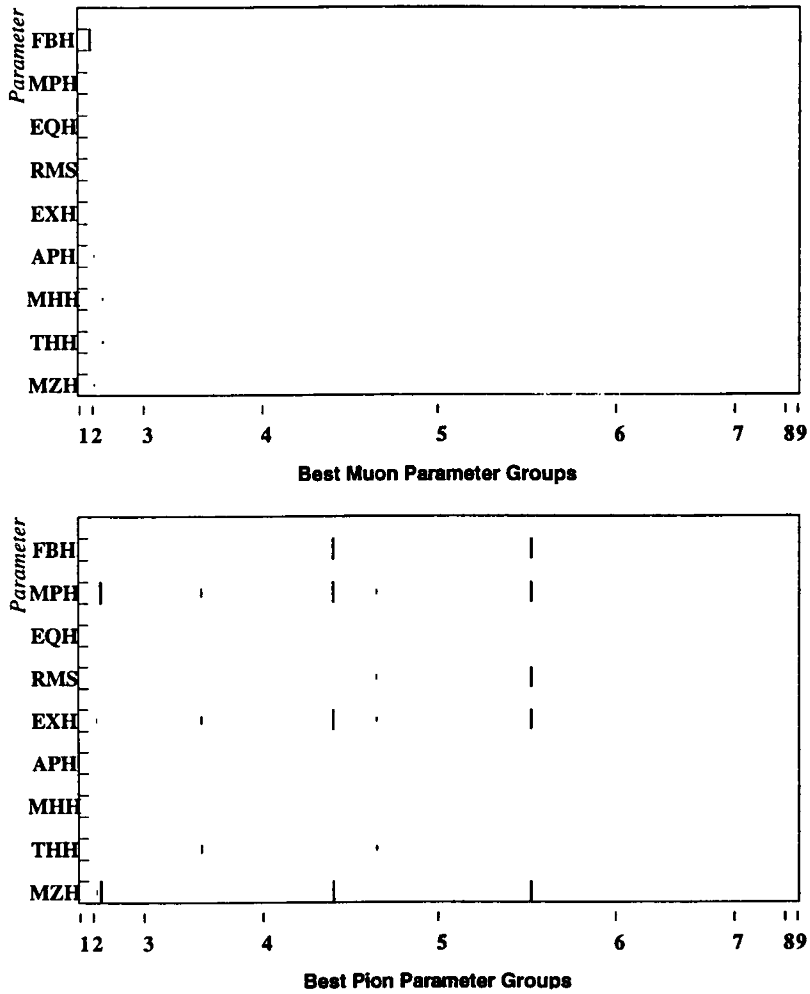

Figure 3-13: Parameter groups that calculate the "best" discriminant function value (i.e. closest to the extremes of the [-2,+2] range) out of 500 events. Horizontal abscissa labels indicate the subgroup size. Note that very few groups calculate the extreme values.

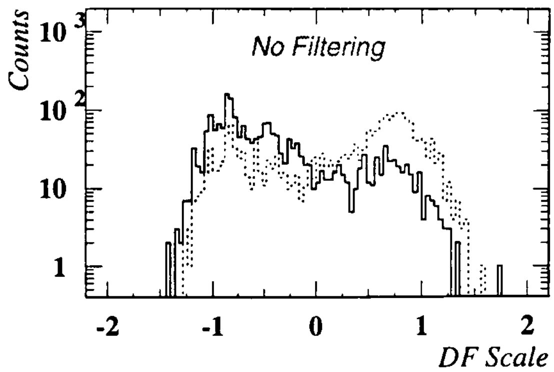

Figure 3-14: Muon(dashed line) and pion(solid line) discriminant functions using data from 2GeV/c muon and pion data runs for training and analysis.

momentum (<3GeV/c) no efficient selection was made. Now, with data collected, we can look at data from the low momentum runs and attempt to select a muon or pion, using the discriminant function.

However, the discriminant function requires training data to form the covariant matrices and the discriminant function averages. As a first pass, let us assume that the muon and pion data taken at low momentum were separated well enough so that they can now be used as training sets. Figure 3-14 shows the discriminant functions for muons and pions at 2GeV/c where the first 5000 events in each associated data run were used for training and the subsequent 5000 events in each were used for analysis. We can see in this figure that there is very little separation, yet there is enough that small peaks are displaced from zero. Two causes may account for the poor separation: either the data is highly contaminated (poorly separated to begin with) or the monte carlo code simulates the setup very poorly.

Most likely the culprit is contamination: we know that our online trigger was inefficient at separating muons from pions at low momentum. We can, as a check, simulate contamination levels to get an estimate of about what the level is and com-

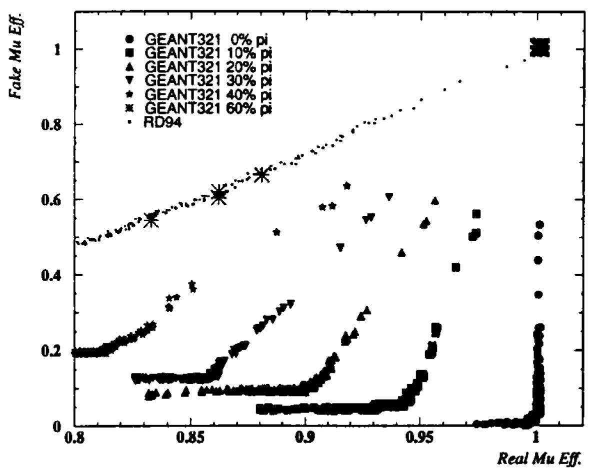

Figure 3-15: Muon Detection Efficiency vs. GEANT Contamination.

pare to MuID data. Figure 3-15 plots real muon efficiency (number of muons above a certain discriminant function cut) to fake muon efficiency (number of pions above the same cut) for both RD94 and GEANT with several different levels of contamination in GEANT. One can see that as the contamination level increases, the distributions look more and more similar, indicating that RD94 was heavily contaminated.

A further confirmation of contamination is the level at which the curves merge. A sample of pions emanating from the target 59m upstream from the MuID, will have, according to [PDG92] the following relationship,

$$P(x) = e^{-\mathcal{M}x\frac{\Lambda}{p}}$$

where P $=$ Probability of survival

$\mathcal{M} =$ Mass of pion ($0.139\mathrm{GeV/c^2}$)

Λ $=$ Inverse of mean proper lifetime ($\tau = 2.6 \times 10^{-8}$s)

p $=$ Momentum(2GeV/c)

which gives a survival probability of about 59% for pions at 2GeV/c. Hence, if we assume that we start with a sample of pions only, 59% will survive to hit the RD94 MuID and the rest will have decayed to muons. This is precisely the level of contamination seen in figure 3-15.

Because of the high contamination then, we can not use the data as it is to define the coefficients. The only recourse seems to be reliance upon simulations to define what "ideal" muons and pions look like.

3.3.6 Re-Analysis: Filtering

If the simulations are somewhat close to reality, then coefficients it defines for the muon and pion discrimination functions will be close to reality and thus training files made of simulated data will approximate the data. However, by using simulations to define muons and pions, we fall into a scenario where one tries to define something in terms of itself. We do not know for a fact that the simulations will define the muon-pion responses with accuracy. With this in mind we set out to develop a new analysis technique to separate muons and pions from each other, yet one that ultimately does not depend on simulations.

Through a series of trials and errors, the technique presented here does, in fact, use simulations as an approximate "picture" from which the discriminant function is built. But, after the approximate, simulation picture is used, it is discarded for the real, MuID picture. The technique begins with generating data sets for muons and pions using the simulation code GEANT (see section 2.9). These data sets are then used to define the coefficients that make up the discriminant functions for muons and pions. Data from the RD94 MuID is then analyzed with it. The discriminant function is calculated for each of 5000 events from both muon and pion data sets. Up to this point, the method is equivalent to that used in the previous section (see 3.3.5).

Now, instead of simply analyzing the events we separate the events according to their discriminant values. If it is below the function minimum, it gets written to a "Pion" file, else it is written to the "Muon" file. After the 5000 events are analyzed and distributed to new files, we then have two new files, one composed of events that look like muons (according to simulation) and one composed of events that look like pions (according to simulation). These new files, although separated by simulation, are still real data events. Nothing in them was changed or modified. If simulations are close to reality, then the data in these files should be close to muons and pions as the RD94 MuID sees them. We call this procedure *Filtering.*

In order to check how well the separation was performed, we repeat the steps on 2 different data sets using 2 different simulation sets to get another set of "filtered" muon and pion files. One set can be used as training and the other for analysis. We show the process schematically in figure 3-16 and the results of performing the filtering process iteratively 5 times in figure 3-17.

The iterative process can be likened to the Newton-Rhapson method of solving for roots of a quadratic equation. In it, one chooses a number near the root of a polynomial, plugs it in and solves it. The solution is plugged into the equation and again solved. After many iterations, the solution either converges to a root of the equation or it diverges. If the difference between successive solutions decreases, then it is said to be converging, otherwise it is diverging. Similarly in the filter process presented here, we start with simulations of the responses of muons and pions as approximations to the true responses, in other words, as training data. RD94 data is then filtered by it, separating the data into muon and pion "solution" groups which then form the next estimate to the true muon and pion responses.

Figure 3-18 shows the efficiency curves for five momenta. In the calculation of each of the curves, except the 1.0 and 1.5GeV/c curves, the measurement was seeded with

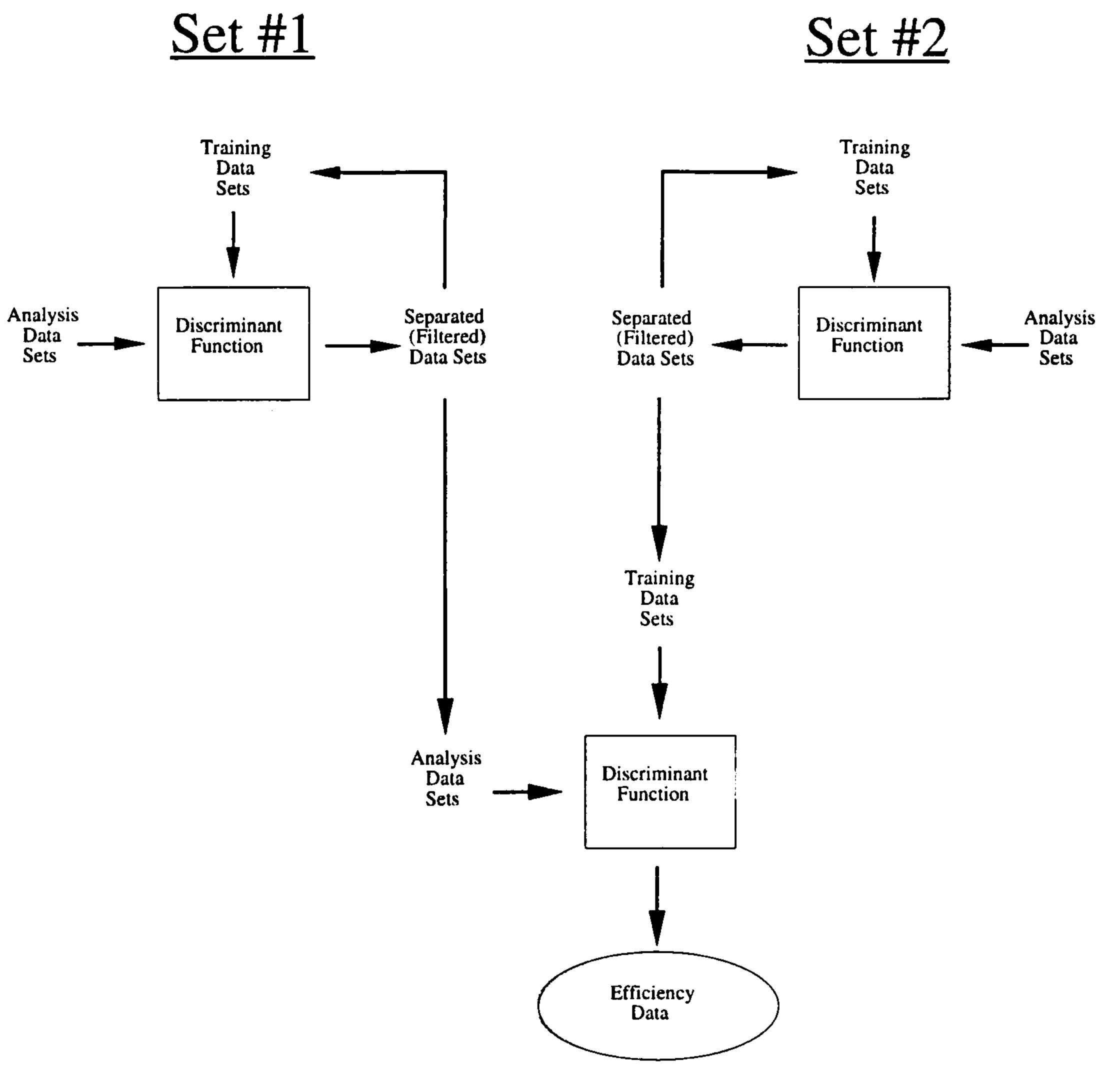

Figure 3-16: Schematic of the filtering process using two sets of training and analysis data. After filtering the analysis data in both sets, efficiency measurements can be made by choosing one analysis set (#2) for training and the other analysis set (#1) for analysis.

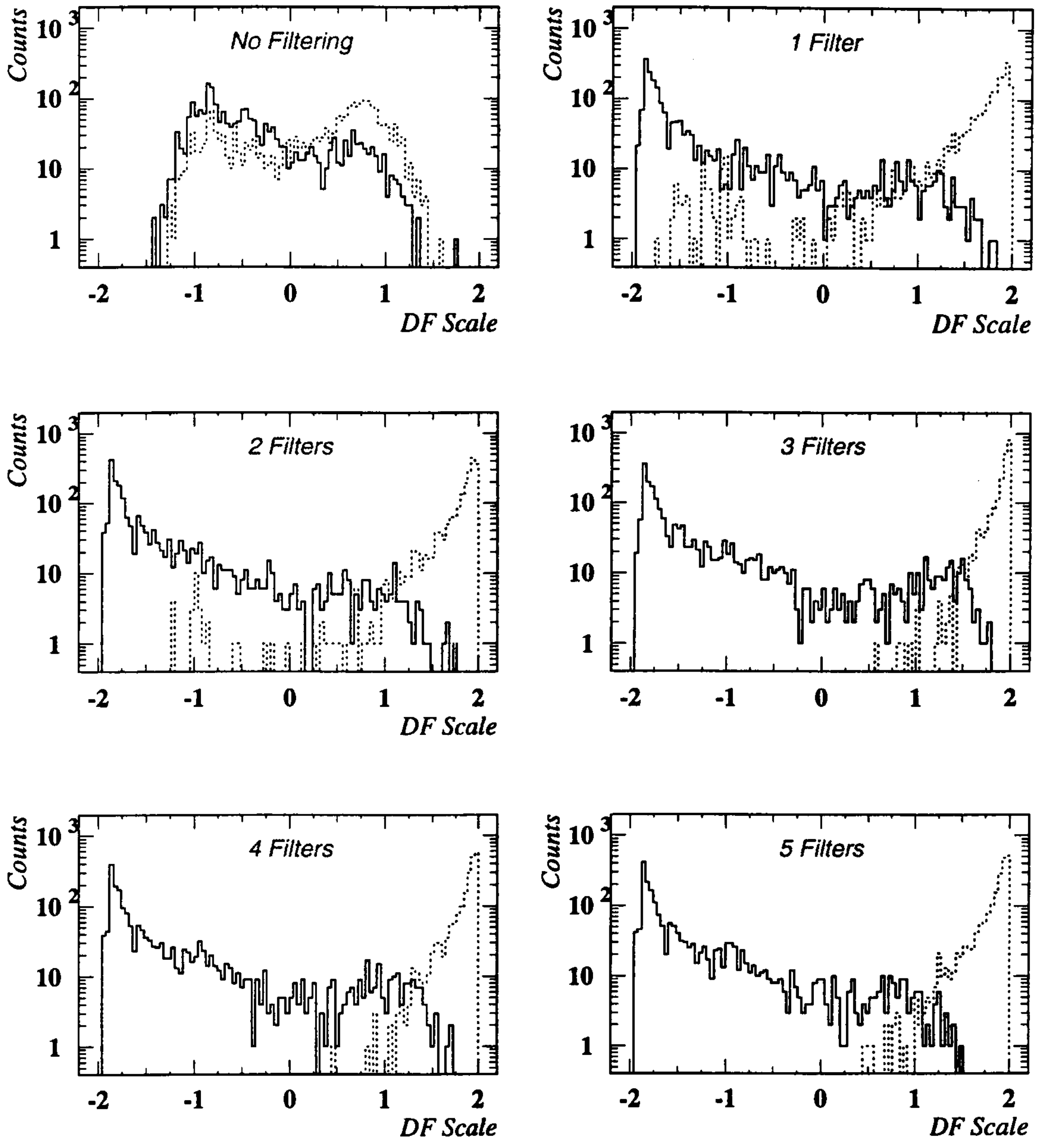

Figure 3-17: The effect of the filtering process after each of 5 iterations shows the function converges.

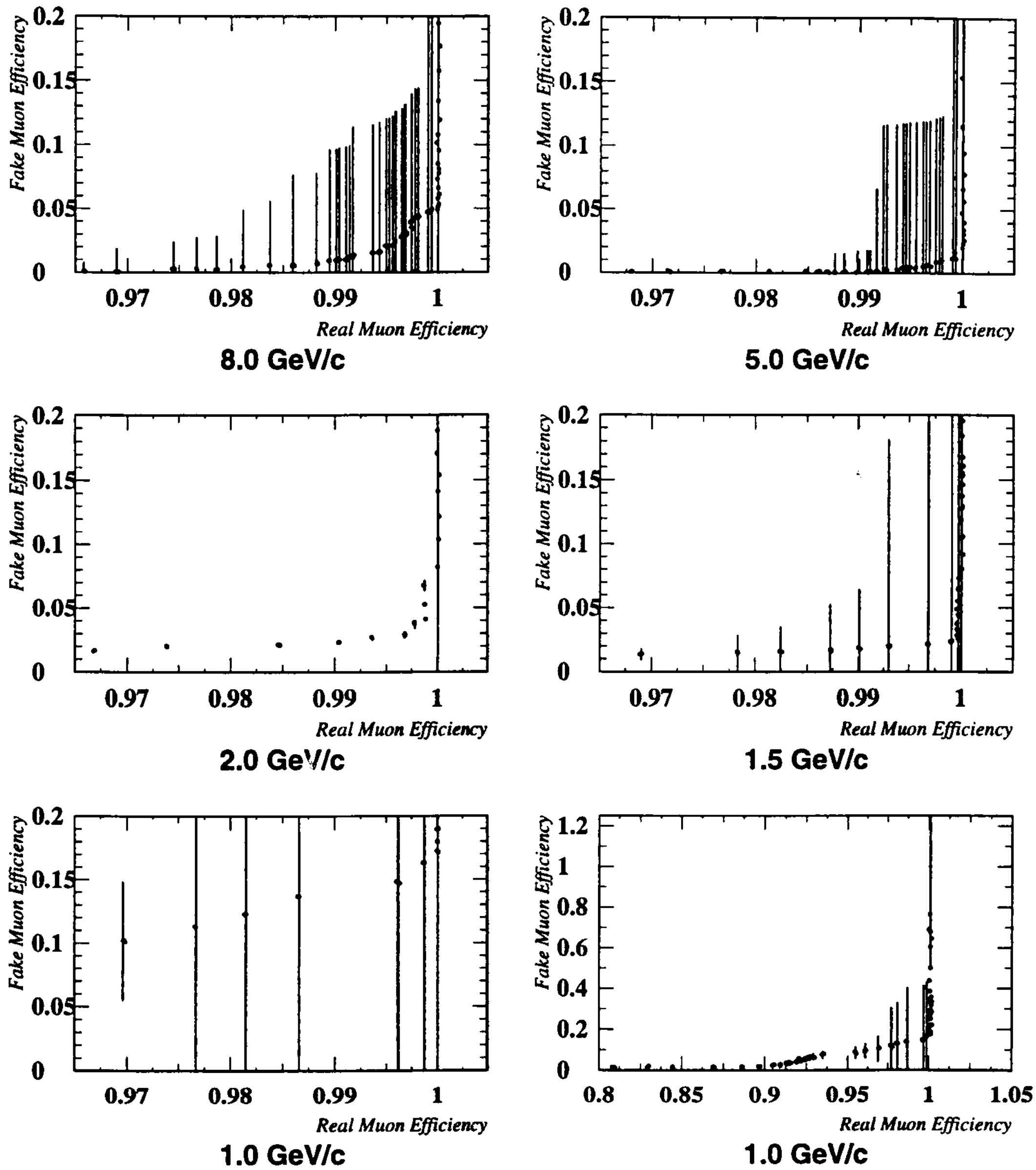

Figure 3-18: Muon-pion efficiency curves for five momenta. The curve for 1.0GeV/c is plotted twice at two different scales.

simulations, meaning that simulations gave the initial distributions of the discriminant variables. However, all subsequent filtering steps were devoid of simulation data. The 1.5GeV/c curve was seeded with the 2.0GeV/c data, and the 1.0GeV/c was seeded with the 1.5GeV/c data. In both the 1.5GeV/c and 1.0GeV/c cases, when the process was seeded with simulation data, the discriminant function $df(\vec{x})$ diverged after several iterations. When the process was seeded with filtered data from the next higher momentum processes, the function converged. We can conclude from this that the simulations were not good estimates of the discriminant function variables at these low momenta.

The curves in figure 3-18 do show that muons can be well separated from pions. For instance, if we set our discriminant function so as to require 97% real muon efficiency, we will make 2% error or less in identifying pions for all momenta except 1GeV/c. At 1GeV/c the error jumps to nearly 15%. This large jump in the pion error rate can be explained by the thickness of the first cell. A 1GeV/c pion has a high probability (>40%) of reacting hadronically in the first cell absorber and nearly 20% chance of ranging out. Also, muons have about the same range as pions, so at this low momentum, the discriminant function is dealing with distributions that severely overlap.

Error Bars

Since we do not actually know the response of the MuID to muons or pions separately, we do feel that this method of separation is possibly the best one can do, given the levels of contamination. Errors can not be assigned to the measurements in relation to a true value because a true value is not known. However, we can estimate the errors by, in a sense, reversing the filtering process. If we consider the filtered data to be the true responses, how well will it separate contaminated *simulated* data? We can measure this exactly by selecting a given momentum, generating two sets of simulated data with a random level of contamination from the opposite species, taking care to note the actual particle identification, but not using it identify the event. After all the events are categorized by the filtration process, we can go through the filtered muon file and count up how many pions were in it. For each of the momenta studied, this accounting was made and it was found that approximately 1% of the pions continued to contaminate the muon set after two iterations. This level is understandable and even predictable given the statistical probability that a pion will not shower before it ranges out.

As another estimation of the error, we use the efficiency curves from these filtered simulated data as an estimate of the true error. The error bars on the curves in figure 3-18 are the fake efficiencies measured after one iteration of the filtering process on these simulated, contaminated, separated analysis files. One sees that in general, the error bars are not much larger than the RD94 fake efficiency. It is only at the extremes of the real efficiency where the error climbs rapidly.

3.3.7 μ, π Separation: Degraded Segmentations

With the separation method established, we can then study the accuracy of separation with coarser granularity in the MuID. We study this by either neglecting certain signals, or treating a region of many hits as a single hit. We first consider lessening the number of planes. The procedure is equivalent to that used previously and outlined in figure 3-16. However, now we neglect all the signals generated in certain planes (starting from the rear of the MuID) which is equivalent to having a thinner MuID[3].

[3]This is approximately, not exactly, true. We should distinguish between neglecting detector planes (something we can do electronically) and neglecting the entire cell (something we can not do without restacking the MUID). Late showering particles in cells with neglected planes can back-scatter into non-neglected detector planes and produce signals. This back-scattering can not occur

Figure 3-19 shows the efficiency curves for four reductions (9,8,7,6 planes plus the full 10 planes curve) in the number of planes for five momenta. Most significantly, the curves reveal that little change is seen in real-fake efficiency for fewer planes — even as few as six. This means that one can make essentially the same measurement with less hardware.

However, it is not so much the number of planes as it is the sampling size and the total thickness between the first and last non-neglected planes. Our sampling size is $0.83\lambda_I$ per cell and six planes is roughly $5\lambda_I$. This thickness is that which [Fabjan82] suggests is approximately the depth needed to contain most of the energy of a hadron shower. Hadrons have better than a 99% chance of showering within the first $5\lambda_I$ (section2.1) and this seems to be the necessary thickness for pion-muon discrimination.

Another significant point to make concerning these coarser granularity studies is that we do not see smoothly shifted curves with fewer numbers of planes. In fact, at certain points, fewer planes appear more efficient than more planes such as in the 8.0GeV/c case where real muon efficiency is greater than 99.5%. In figure 3-19 (8.0GeV/c), eight planes of detectors have lower fake efficiency when 99.5% (or higher) real muon efficiency is required. This suggests that the analysis may be limited at high real muon efficiency.

The PHENIX Experiment has six planes in its design but the cell thickness are not uniform. The first absorber (not including the main magnet pole piece) is 30cm followed by 10cm, 10cm, 20cm, 20cm, 20cm. The total thickness is then 110cm or $6.5\lambda_I$. The main magnet pole piece adds another 60cm of iron to yield over $10\lambda_I$ be-

---

if the absorber as well as the detector plane was removed. This effect is small for two reasons. First, the planes at the back are the ones neglected in this study where few hadrons penetrate (probability $\propto e^{-\lambda_I} \approx 10^{-2.2}$ at $5.0\lambda_I$) and second, the particle's momentum is in the forward direction so the probability of back-scattering massive charged secondaries is small. Figure 2-18 shows back-scattering in the front cells in a simulated pion event.

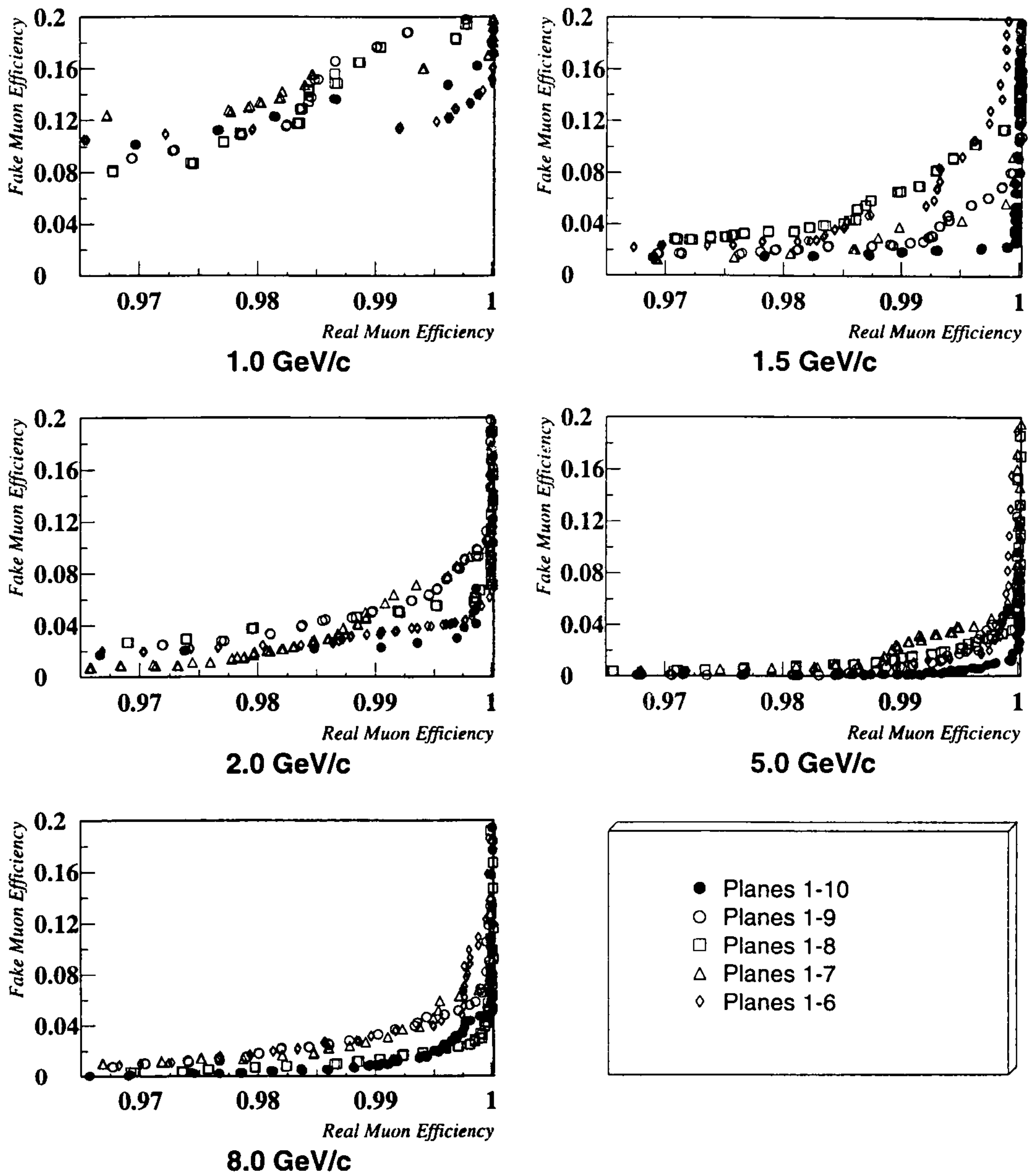

Figure 3-19: Efficiency curves as a function of fewer planes.

tween the interaction region and the last detector plane. With this in mind, what arrangement of RD94 cells, which are all ≈14cm, best resemble the planes in the PHENIX Muon Identifier? First, let us consider only the Muon Identifier portion of the Arm and assume that the Muon Tracker provides all the information that RD94's upstream detectors provide (i.e. momentum and particle identification). After all, the essential role of the PHENIX MuID is to identify those particles that pass through the Tracker unidentified. Next, let us limit then number of planes to six, and keep the total thickness between the front of the RD94 MuID and the last plane approximately $6.5\lambda_I$. From these considerations, we arrive at four configurations other than simply the first six planes:

1) Planes: 1,2,3,4,5,7; $= 5.8\lambda_I$

2) Planes: 2,3,4,5,6,8; $= 6.6\lambda_I$

3) Planes: 1,2,3,4,6,8; $= 6.6\lambda_I$

4) Planes: 1,2,3,5,7,9; $= 7.5\lambda_I$

The second arrangement resembles the PHENIX MuID best. The total thickness is close to PHENIX's and the first cell has a 30cm thickness, which is close (within 2cm) to the thickness of two cells (14cm each) of RD94's. However, as shown in figure 3-20, the second arrangement also appears to do the worst of the four arrangements at separating muons and pions at the low momenta, both 1.5GeV/c and 1.0GeV/c, which is most likely due to the very thick first absorber.

Besides varying the numbers of planes, we can vary the numbers of strips on a plane by summing all the charge on a given set of strips, and if it is greater than zero, call it a hit. This has the effect of degrading the granularity while still keeping the total deposited charge the same. Figure 3-21 shows how the efficiency curves

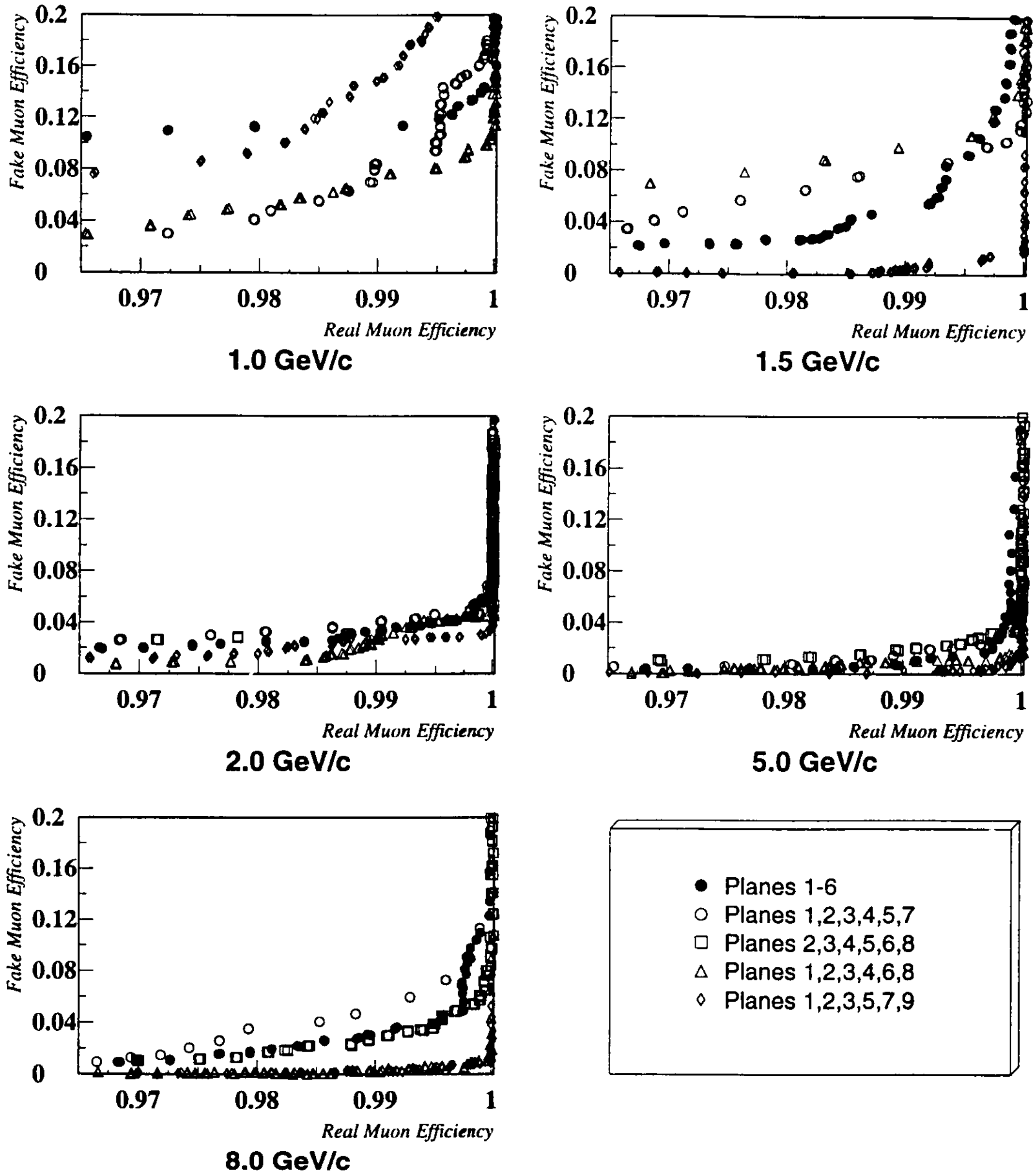

Figure 3-20: Efficiency curves for various combinations of six planes which resemble the PHENIX Muon Arm. These combinations were chosen based on 2 criteria: matching cell widths as closely as possible and keeping thickness between the first and last plane close to PHENIX's. Note that at low momentum (1.0 and 1.5GeV/c), the efficiency curves for the open squares do not fall within the axes. This is the curve which most closely resembles the PHENIX Muon Arm.

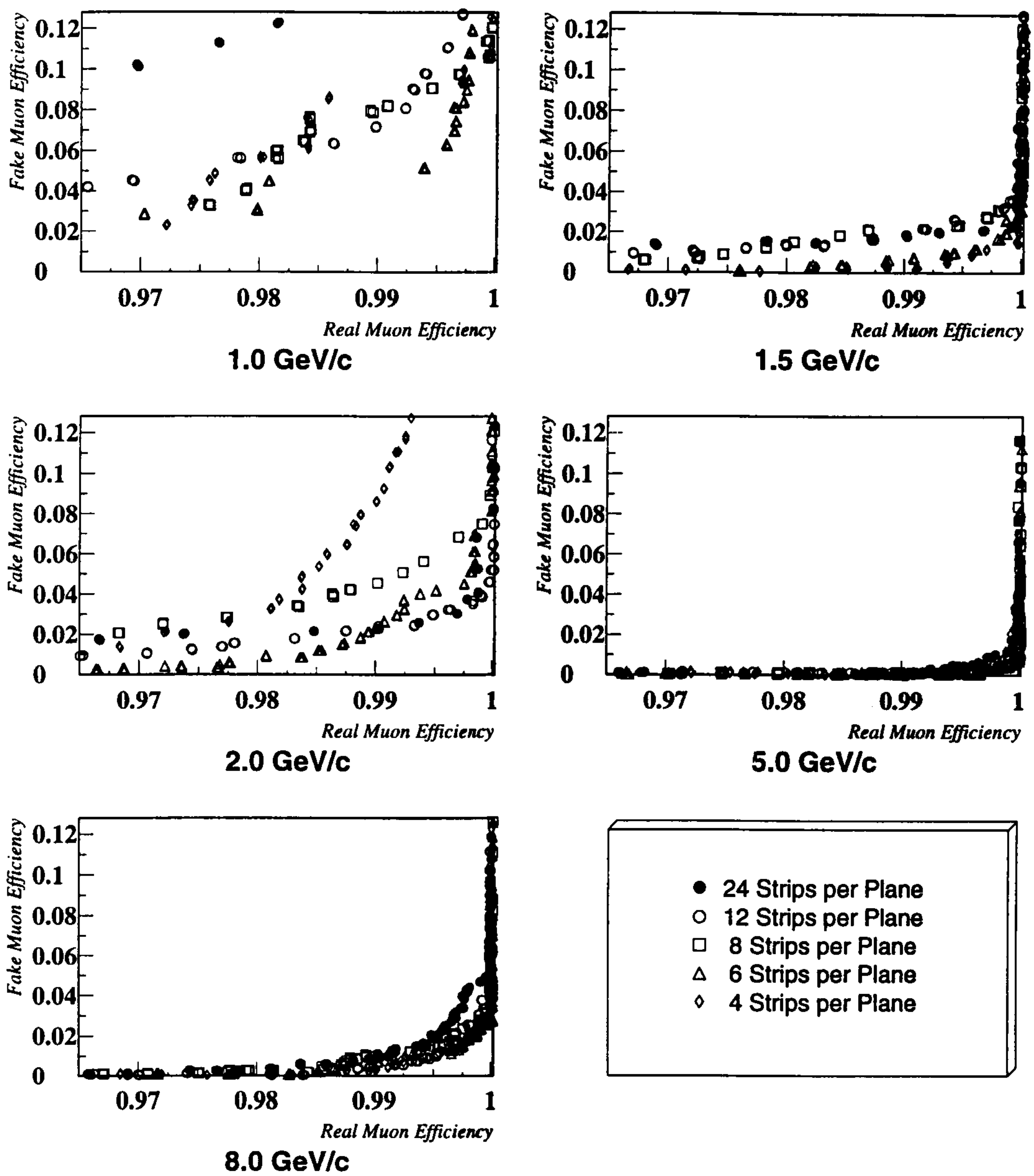

Figure 3-21: Efficiency curves as a function of fewer strips.

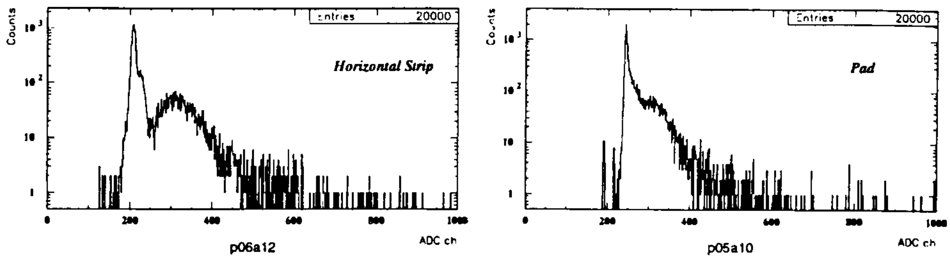

Figure 3-22: Comparison of the charge spectra in pads and horizontal strips for 6GeV/c muons. ADCs are approximately 50fC/channel.

vary with four groupings of strips, along with the curves of individual strips with all ten planes active. Above 5GeV/c, all strip combinations appear to yield about the same efficiencies, but at 2GeV/c and below, some are clearly better. What is most interesting is that some of the combinations do better than the individual strips. This may be attributed to the fact that combining the strips (effectively broadening the strip width) eliminates ambiguities which may arise from the broad area over which the charge is distributed.

3.4 MuID Response

3.4.1 Strip and Pad Readouts

It was the intent of this experiment to study the responses of the MuID with both strip and pad geometries of capacitive pickups. Although data was obtained for both, only the strips were studied in detail in this thesis. We present a brief description of the charge spectra here.

In figure 3-22 we see typical charge spectra for horizontal strips and pads and note the slight shift downward in the pad's peak in relation to the pedestal as compared to the horizontal strip.

The streamer pulse is quite large compared to the pulse generated in lower voltage modes of operation, such as the proportional mode. The charge generated in the limited streamer mode is about 30pC while proportional mode pulses are on the order of a few pC[Iarocci83]. However, this relatively large pulse is not fully seen by the external pickup. The peak in the charge spectra shown in figure 3-22 is only about 75 ADC channels above the pedestal mean, which is about 4pC (0.05pC per channel) when the pulse should be nearly 10 times that amount. Since the signal goes through 70m of cabling and an inverting transformer before it gets to the ADC, we expect some loss in signal strength due to transmission losses. However, these losses were measured to be on the order of 3-5% for fast pulses. The remainder of the loss is due to the transparency of the capacitive coupling.

3.4.2 LST Efficiency

The efficiency measurement of the LSTs was made by counting the number of planes that recorded a hit when hits were recorded in the first muon tagger, M1. Normally, when making an efficiency measurement, one uses a tandem three-detector arrangement. When the first and third detectors register a hit, one looks to see if the middle detector registered a hit. The ratio of the middle detector hits to the first and third detector coincident hits is the efficiency. In the RD94 Experiment, we have such a tandem arrangement defined by the start counter S4, the MuID, and the first muon tagger, M1. Because the MuID and M1 are both segmented detectors, we have a slightly more complicated measurement since incident particles can shower within the MuID and register more than one hit per plane. We thus make the measurement for a variety of scenarios. We select muons, particles that we do not expect to have broad showers akin to hadronic showers, and count the number of planes that register a hit and divide by the number of planes in the MuID (10). We normalize to the number of events in the run and measure this with respect to the number of hits seen in M1. In addition, since the MuID is highly segmented, we can consider four logical constructs of horizontal (Hor) and vertical (Ver) strips: Hor AND Ver, Hor independently, Ver independently, and Hor OR Ver. See figure 3-23.

Since the independent Hor, independent Ver, and the combined Hor AND Ver efficiency measurements all have individual detector flaws included in them, the most reasonable and accurate measurement is when either horizontal OR vertical strips fire, and there is only one hit in M1. That efficiency is $86 \pm 2.5\%$. Considering that this measurement was made with 9GeV/c muons which multiple scatter less than a few degrees through the entire thickness of the MuID, we can consider the geometrical efficiency to be that for particles incident normal to the planes, i.e. 90%. Dividing out this efficiency from the efficiency of 86%, we get 95% which is consistent with that of [Battistoni80].

3.4.3 The Charge Measurement

In the list of measurements (table 3.2) used by the discriminant analysis to determine the set of measurements that will best discriminate muons from pions (section 3.3.4), the energy measurement is absent. Two reasons may be how the deposited charge was modeled (recall that the best set of measurements was determined from simulations) and that the deposited charge is somewhat independent of the species. It is necessary to assess the usefulness of the charge measurement because it may be used in PHENIX.

Charge Modeling

In the simulation program used to model RD94, GEANT, individual particles are tracked stepwise through each volume they penetrate. The total energy deposited by the particle in each volume of the detector is calculated and summed at each

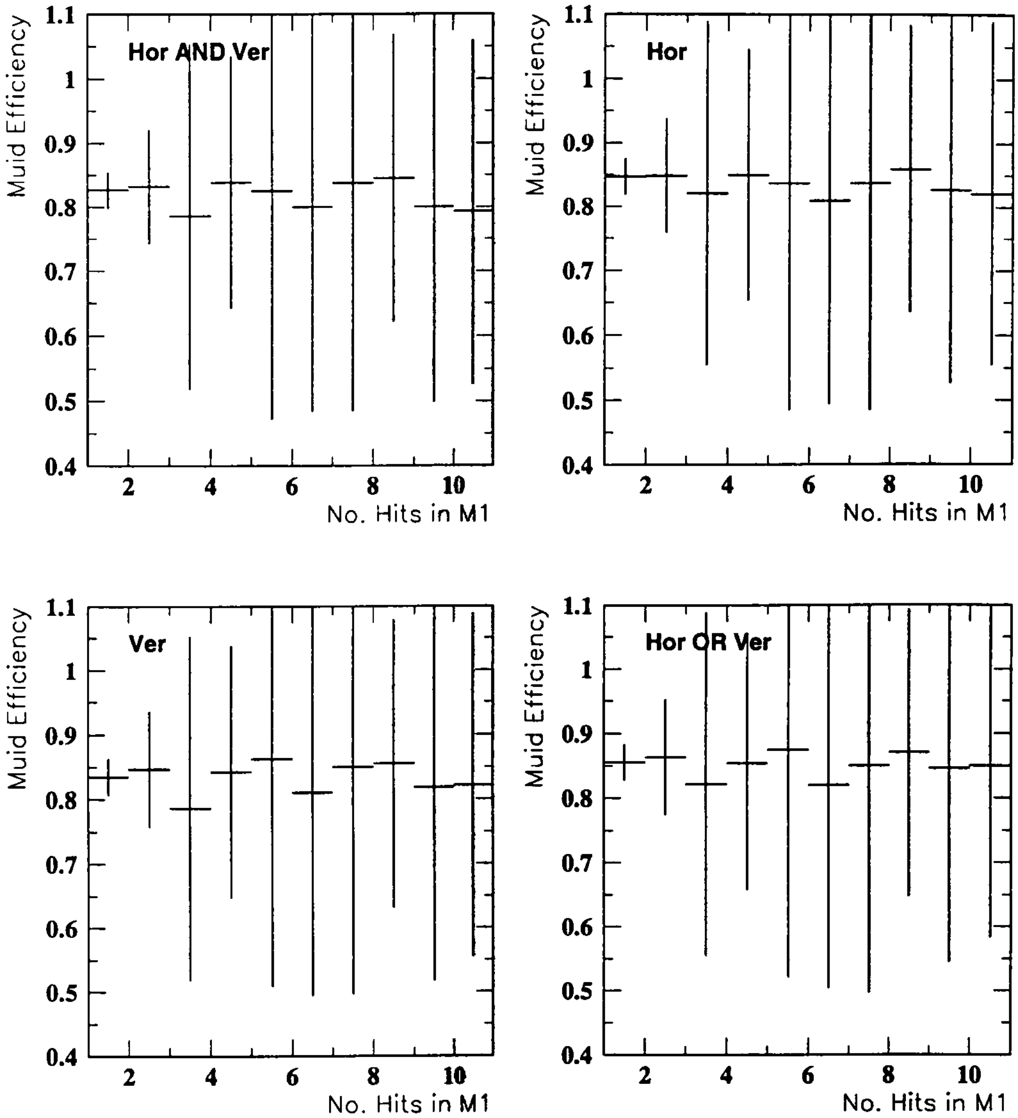

Figure 3-23: LST efficiency as measured by summing the number of planes recording a "hit" divided by the number of planes and the number of events. This measurement was made with 9GeV/c muons which required a hit in the M3 muon tagger downstream of the Muon Identifier. The measurement was made for several scenarios. The abscissa of the histograms is the number of hits in the first muon tagger, M1. Each of the histograms describes which orientations were considered. The one number that describes the efficiency of the LSTs best, barring geometrical inefficiency, is when horizontal OR vertical strips are considered and there was only one hit in M1. This efficiency is 86 $\pm$ 2.5%.

step and stored upon exiting the volume and can be recalled at any time during the event by the user. As charged particles passed through the individual 9mm x 9mm LST gas chambers, the particle emerges having deposited a given amount of energy. That amount of energy is proportional to its path length through the gas volume (see figure 3-24), its incident energy, its mass, and the gas itself as per the Bethe-Bloch formula. Experimental values for ion-pair production in an Argon iso-Butane gas mixture show that pions, for instance, will produce between 100 and 1000 ion-pairs per centimeter with incident energies between 1MeV and 10GeV[Palladino74]. If one ion-pair is produced, it drifts into the avalanche region where the streamer is produced. In the streamer, tens of thousands of secondary electrons are released according to the First Townsend Coefficient (see figure 3-25), so even though the

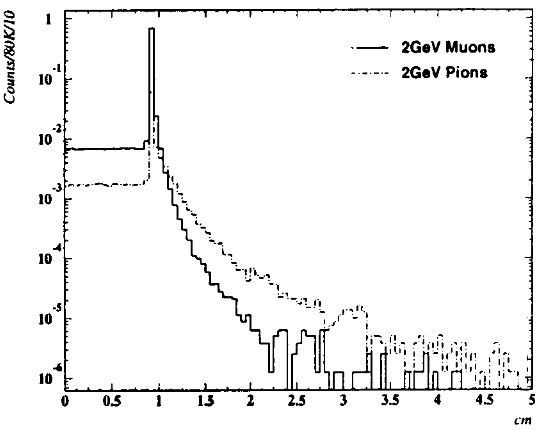

Figure 3-24: Average track lengths of muon and pion events. The tracks through all gas volumes of all primary (incident) and secondary (shower) particles are histogrammed and normalized to the number of incident particles times the number of planes (10) in the stack. The large peak at 9mm indicates most particles travel orthogonally through the gas volume. The flat region below 9mm indicates particles that pass through at some angle, where some fraction of 9mm is encountered in one gas volume and the compliment is passed through its neighboring gas volume. The long tail indicates particles at some angle parallel to the anode, traversing long paths within a gas volume.

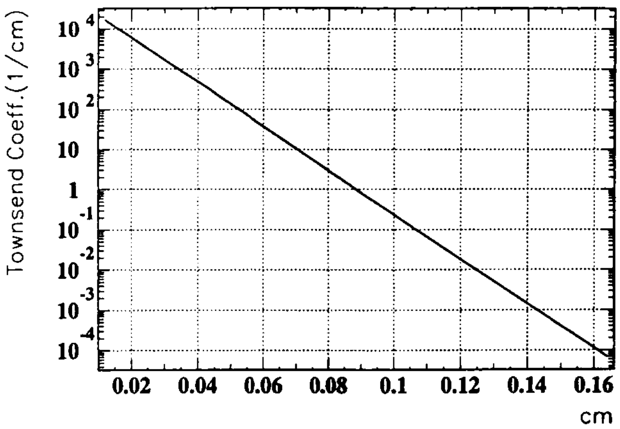

Figure 3-25: First Townsend Coefficient calculated according to the expression $\alpha/p = Ae^{(-B\frac{p}{E}x)}$ where α is the First Townsend Coefficient; p is the pressure in Torr, here ambient is used; E is the electric field, approximated here by E=V/cm=4800V/cm and x is the distance away from the anode. The constants are A=120 cm^{-1} Torr^{-1} and B=284 V cm^{-1} Torr^{-1}[Sharma92]. The avalanche region begins when α is just greater than 1; here it is just under 0.9mm.

number of primary ion-pairs may vary due to energy or mass of the particle, the streamer that is produced is virtually independent of the number of primary ion-pairs. We conclude then that if a charged particle penetrates the gas volume, then the probability of creating a streamer is near 100%. If the incident energy is low ($\leq$keV) or the particle passes through a small fraction of the gas volume at the edges where the electric field is small, the probability of streamer production lowers. In the simulation program, these effects were not fully taken into account but were approximated by simply requiring that the particle penetrate more than 2mm of gas. Because streamers are nearly certain to be produced once a few primary ion-pairs are produced, we can assume that any inefficiency of the LST is mainly geometrical (see section 2.4.2).

In addition to modeling streamer production is how the charge of the streamer is collected on the capacitive pickups. When a streamer is produced, the image of

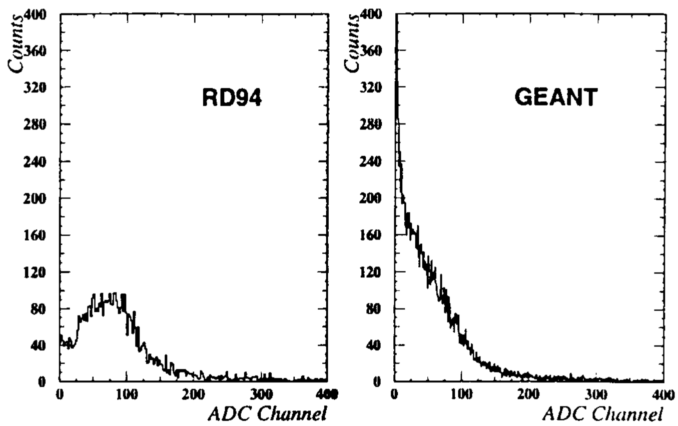

Figure 3-26: Comparison of the charge spectra in RD94 (left) and GEANT (right).

the charge is flashed onto the pickups. This image is opposite in polarity and has a gaussian form that extends to infinity. However, the range of *detectable* charge above background noise appears to extend ±3cm transverse to the anode and ±5cm parallel to the anode[4]. When a particle penetrated more than 2mm of a gas volume in the simulation code, a random amount of charge was chosen, based on a charge spectrum from one real charge spectrum from the MuID. That amount of charge was then placed on both the horizontal and vertical strips in fractional amounts, depending on the production site in relation to the strips. A strip was considered "hit" if the total charge on it was greater than zero. A comparison of the real charge spectrum and the modeled charge spectrum shows disagreement. See figure 3-26. We assume the disagreement is due the fact that the charge spectrum *from one strip* was used instead of the sum of the charge *from one side of the plane.*

[4]The transverse extent of the detectable charge was measured from timing the signals picked up with eight 0.4cm strips over a small area on a single LST exterior to the MuID (a separate experiment run in conjunction with RD94). The parallel extent was measured by fitting hits on the vertical 4.0cm strips within the MuID for single non-showering particles (muons).

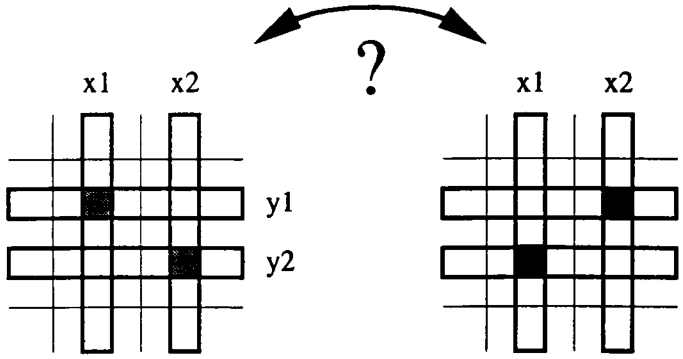

Figure 3-27: An example of hodoscopic ambiguity when two particles are considered as the source of the hits. Patterns that may also yield two horizontal and two vertical hits include three and four particles.

Distinguishing Hodoscopic Ambiguities

It was hoped that even though the *size* of the streamers could not distinguish different particle types, that the *number* of streamers may be a detectable quantity and lead to distinguishing position ambiguities. When multiple particles hit different regions of the plane, their positions are uncertain because the horizontal and vertical measurements are independent of each other. When two vertical strips (x1 and x2) and two horizontal strips (y1 and y2) register hits, the number of particles and actual positions are ambiguous. For example, there are two different ways that two particles could pass through and register two vertical and two horizontal strips. See figure 3-27. Also there are four ways that three particles could register strips in the same way and there is one way that four particles could register the same strips[5]. Normally with grid arrangements, a third, stereoscopic measurement is made at an angle to the orthogonal measurements to remove the ambiguity. However, if the sizes

[5]We do not include the cases where more than one particle passes through a given horizontal-vertical junction. That possibility certainly exists but we do not include it when counting the possibilities.

of the streamers are different, then this can be used as the differentiating third measurement. If we sum the charge that is collected on all the strips on one side of one plane and plot it versus the sum of the charge collected from the strips on the other side of the plane, we would expect that single streamers would be differentiable from multiple streamers. However, multiple streamers were not observed to clump in these curves (see figure 3-28) and it is expected that the reason is due to the broad range

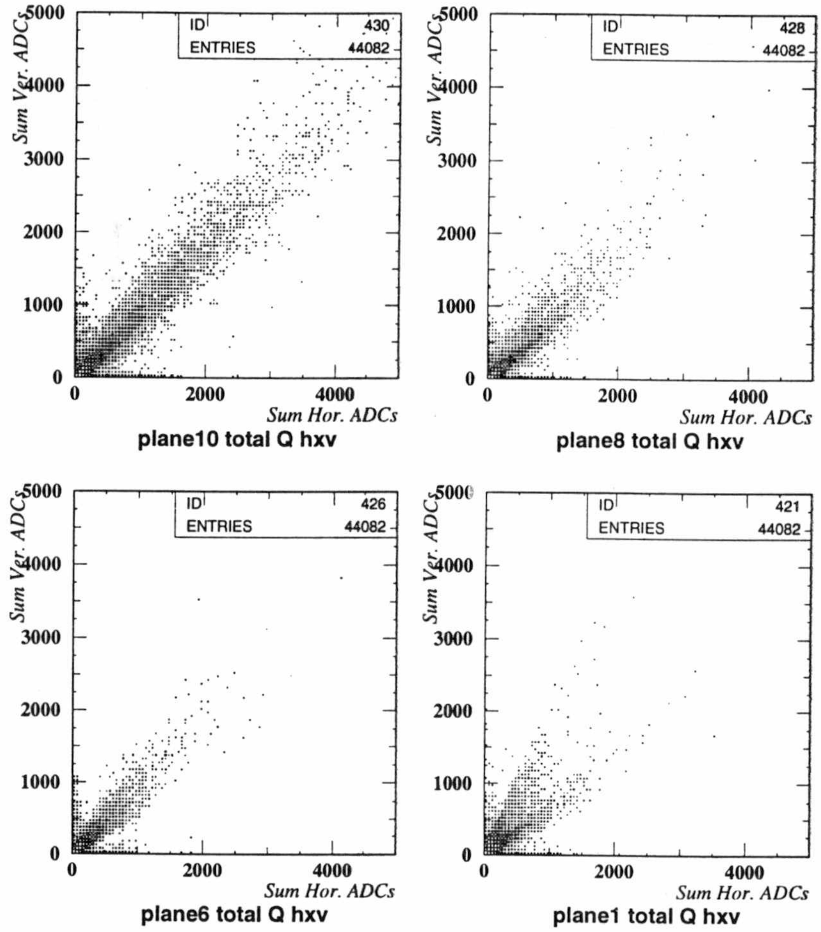

Figure 3-28: Collected charge on horizontal versus vertical planes for four planes. The source of the forked structure in the Plane 1 is unknown.

in charge that streamers possess.

3.4.4 Individual Particle Responses

The response of the MuID can be measured in several ways and we choose to describe it in terms of the depth of penetration. This is also one of the chosen discriminant variables (section 3.3.4) otherwise known as MZH and MZV for Maximum Z (extent in Z or longitude) as measured by the Horizontal or Vertical Strips. The main thrust is to simply show, via this one variable, how the responses compare to simulations and to give the reader an idea of how well the MuID performed. In the following histograms, the last plane hit, as measured by its plane number, is histogrammed and the number of counts are normalized to number of incident particles. GEANT predictions of the same measurement are superimposed on each plot with the exception of the electron histograms.

Figure 3-29 describes the response of protons. In general, the RD94 data follows the GEANT calculations well. Because some noise is allowed in the analysis (see section B) so as to throw away less actual deposited charge when the noise is suppressed, there are several false hits. Because we are measuring the last plane that sees a hit, the peak tends to flatten some and shift toward the rear of the MuID. Overall, the responses are similar.

Figure 3-30 shows the RD94 response to electrons. The GEANT calculations are not shown on these histograms because very few GEANT electrons penetrated the first absorber. Less than one in one thousand of the incident electrons registered a hit in the first plane for all of the momenta calculated.

The pion figures (see figure 3-31 also follows the GEANT calculations well, given the high noise level. It should be noted, that the pion punch-throughs will not show up in the data and should show up in the calculations. The punch-throughs are

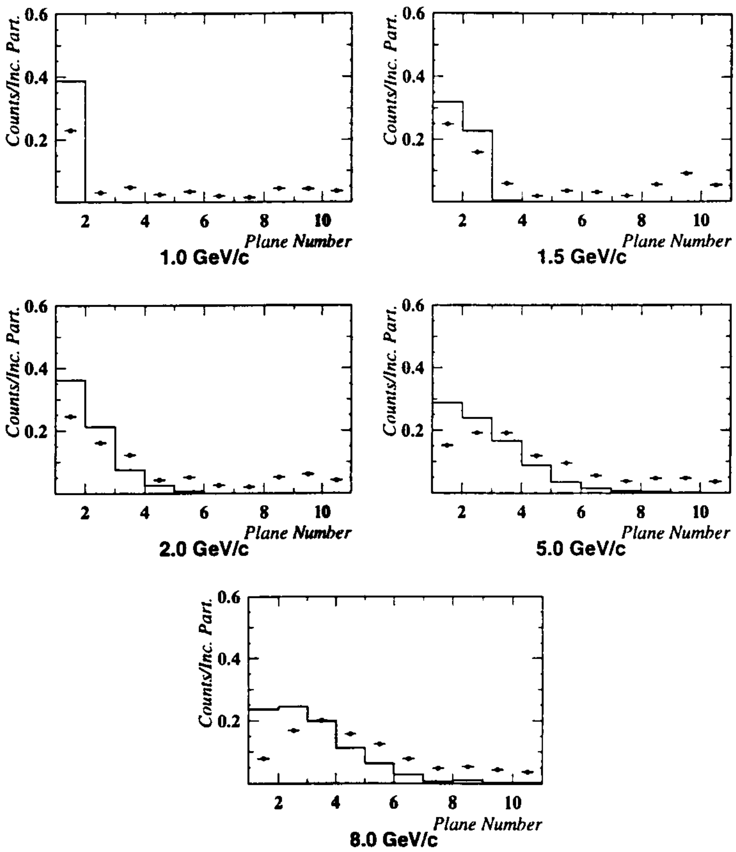

Figure 3-29: Proton response of the MuID as described by the last plane recording a hit. GEANT calculations are the bar histograms and the markers are RD94 data. Error bars are statistical.

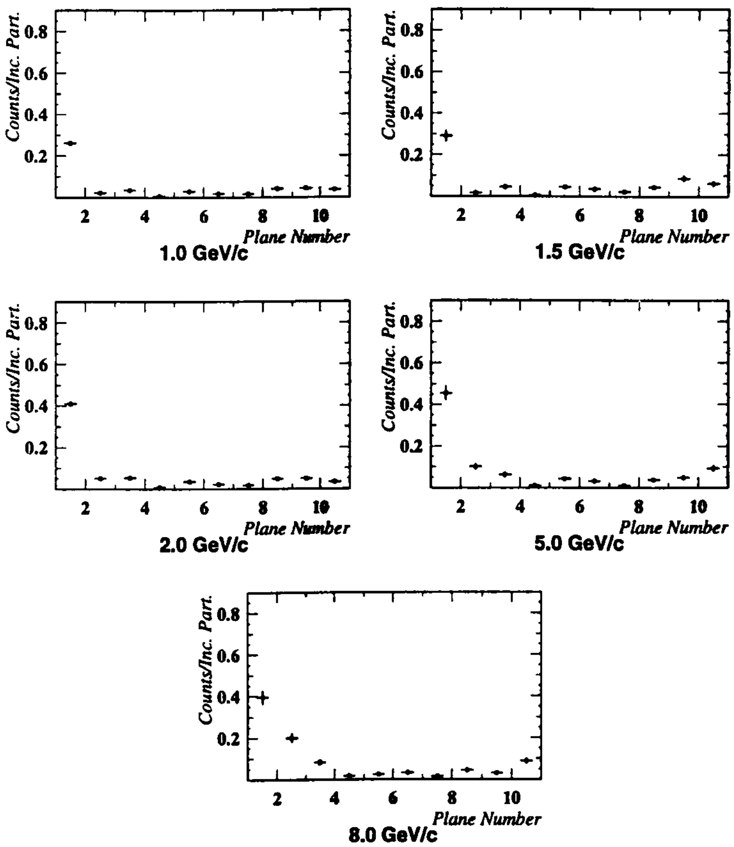

Figure 3-30: Electron response of the MuID as described by the last plane recording a hit. GEANT calculates less than one in one thousand electrons will penetrate the first layer.

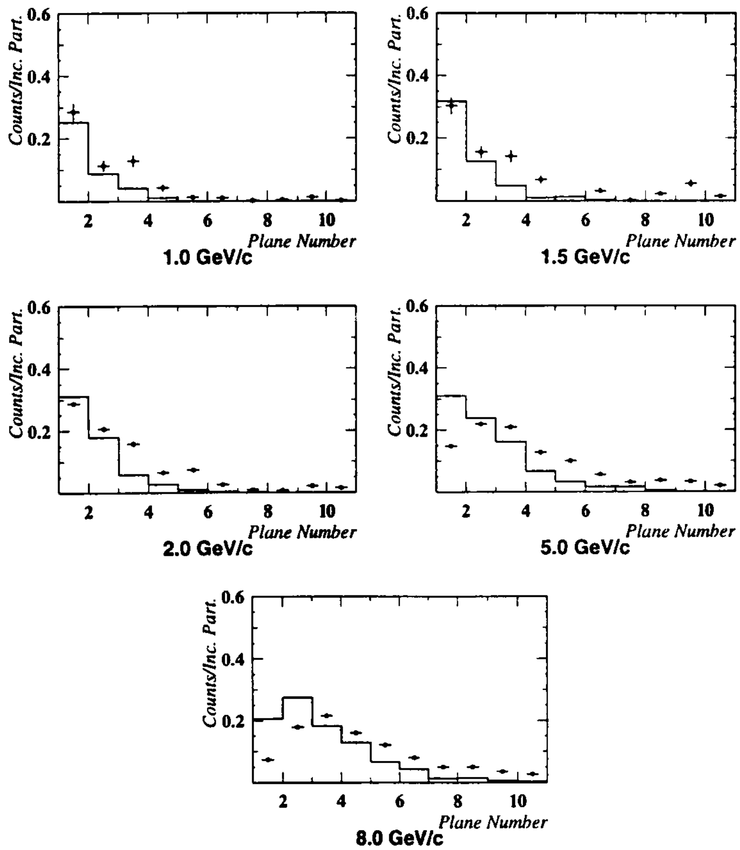

Figure 3-31: Pion response of the MuID as described by the last plane recording a hit. GEANT calculations are the bar histogram and the markers are RD94 data. Error bars are statistical.

those statistically few pions that do not interact hadronically and exhibit behavior indistinguishable from that of muons. The discriminant function will include these punch-through pions in with the muons and nothing can be done about them with this method. We minimize these punch-throughs by making the MuID as thick as possible since the probability of interacting hadronically goes as $e^{-\lambda}$. The RD94 MuID is $8.3\lambda_I$thick meaning we have an inherent contamination level of 0.02% from punch-through pions in the muon sample. Since this is two orders of magnitude below the necessary level of 1-3% we can consider it negligible.

The muon response (figure 3-32) likewise follows the calculations well. At 1GeV/c we have the greatest discrepancy but again, we find it is due to the low threshold of the pedestal subtraction.

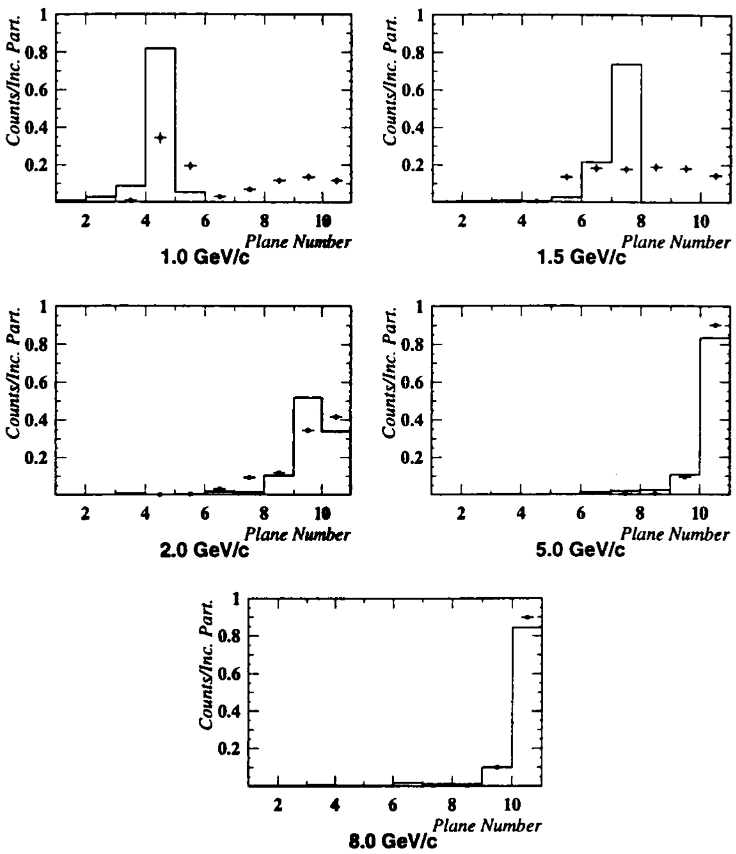

Figure 3-32: Muon response of the MuID as described by the last plane recording a hit. GEANT calculations are the bar histogram and the markers are RD94 data. Error bars are statistical.

Chapter 4

Discussion and Summary

4.1 Discussion

In the forgoing chapters we have described the RD94 Experiment, its motivations, its construction and design, and its analysis and results. This chapter is meant to be a discussion of the results in light of the goals of RD94 as presented in section 2.2. For each of the goals we present a short discussion of what was accomplished.

4.1.1 Primary Goal

As stated in section 2.2.1, the primary goal of the RD94 was to determine if muons and pions can be separated to the 1% level using a device based on sampling calorimeter technology and discriminant analysis techniques. We chose a set of variables from a fairly large and comprehensive set of measurements based on how well each subset of measurements separated muons and pions. A discriminant function was then defined, based on the best subset of variables and muon-pion events from RD94 were separated (filtered) based on the simulated data. The separated files then defined a new discriminant function which then re-separated the data. To calculate the efficiency of separating muons and pions, this procedure was performed on two different sets of data. One set defined a discriminant function and the other was analyzed based on that function. We recognize that the measured efficiencies are not measured with respect to an absolute known so error was determined based on inverting the procedure by testing how well simulated data was separated based on the discriminant function that was defined by the separated RD94 data. The curves presented in figure 3-18 show the levels of efficiency for separating muons and pions using the muon identifier together with this discriminant analysis technique.

PHENIX's goal of 3% separation at 1GeV/c and 1% separation at 2GeV/c look close to being met. At 2GeV/c, fake muon efficiency drops to 2% for high real muon efficiency (97%) which may be an acceptable. At 1GeV/c, however, the fake muon efficiency sharply increases to 10% fake efficiency at 97% real efficiency. Clearly this is not an acceptable level for PHENIX.

One reason for the large inefficiency at low momenta has to do with the discriminant function variables. Since we use a segmented device, the discriminant variables become discrete and at low momenta, the same numbers begin appearing for values of the variables. For instance, the front-to-back ratio has a limited number of values it can be. There are six different values (0-5) for the numerator and five for the denominator (1-5) making only 30 allowed values this one particular variable can have. Lowering the momentum, decreases the subset of the possible 30 values. This effect is clearly evident in figure 4-1 where we compare the discriminant functions *df* of pions and muons at 1GeV/c and 8GeV/c. The low momentum *df* exhibits spiking where the high momentum *df* are relatively smooth.

In addition to measuring the efficiencies for the over-segmented MuID, we measured degraded segmentations with the intent to define minimum segmentation requirements, including the use of fewer planes, different arrangements of six planes (the

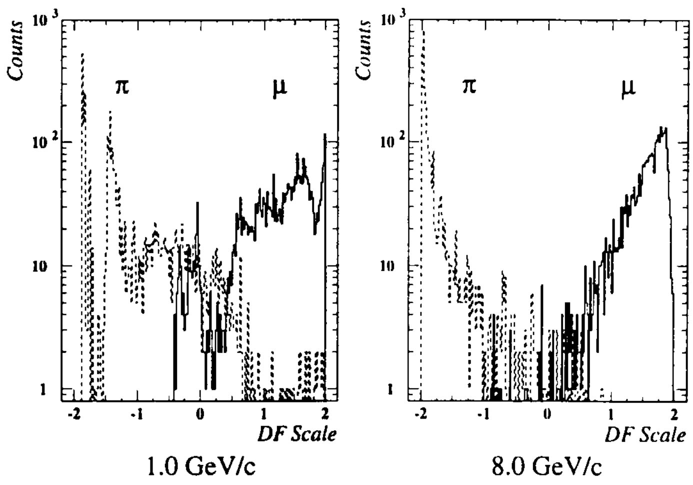

Figure 4-1: Discriminant function comparison at low and high momentum showing the effect of decreased range allowed by discriminant function variables.

number of planes PHENIX will have) and wider strips on each plane. The efficiency curves did not change drastically with the use of fewer planes (as few as six) but the arrangement of the six planes clearly showed an effect. At 2GeV/c and higher, all five arrangements that were measured yielded about 2% fake efficiency at the 97% real efficiency level. But below 2GeV/c, fake efficiencies varied widely at high real muon efficiency. The arrangement that most closely resembles PHENIX's arrangement had fake muon efficiencies greater than 20% at all high real muon efficiencies. This is most likely due to the very thick (30cm) first absorber layer in PHENIX's stack[1].

With wider strips (as wide as 24cm) the efficiencies did not worsen but, in fact, improved. At 1GeV/c, wider strips improved the efficiency measurement and may even be within an acceptable level for PHENIX. The reason for improved efficiency

[1]The trajectory through the the first layer is effectively lengthened on two accounts: first, the particle will strike the initial layer with an incident angle between 10° and 35° adding between 0.5cm and 6.5cm respectively to its path through the steel. Second, the particle will have a skewed component to the angle because of the kick added to it from passing through the radial magnetic field in the tracking section. This added kick will be momentum dependent, larger at lower momenta, which will add even more to its path length through the steel.

with degraded segmentation may be due to the extent of the deposited charge on the pickups. When a streamer forms, charge is deposited over a broad area of the capacitive pickups. When the strips are narrow, many strips see fractions of the deposited charge, increase the number of hits on a plane and confuse the discriminant function; as they widen, an optimum is reached where one strip (on average) sees a hit for one streamer. We found by matching simulated data to physical data that the optimum is different parallel to the anode (9.0cm) or perpendicular to the anode (3.8cm). The difference is reasonable because the charge of the streamer spreads out along the anode, inducing charge over a broad length. Hence, horizontally oriented strips see more charge per strip and fewer strips per streamer are hit; and the vertically oriented strips see smaller fractions of the charge and more strips per streamer are hit.

We found that muons can be efficiently ($\approx$2%) separated from pions over 2-8 GeV/c with as few as six planes distributed by several arrangements between 5.0 to 7.5 λ_I. Below 2GeV/c, the efficiency greatly worsens (>20%) with a thick front absorber. Also, we found that thinner strips does not imply improved separation and even strips that were wider than their optimum gave better efficiency.

4.1.2 Secondary Goals

Hardware

The Iarocci Tubes, 9x9mm^2 limited streamer mode tubes, were used as the primary component of the detection layers in the MuID and, on the whole their operation went quite smoothly. The tubes operated quite efficiently ($\approx$86% including geometrical inefficiency) and virtually trouble-free. One-hundred-twenty tubes were used in the MuID through two run periods, one in 1993 and one in 1994. Only one tube failed during that time, just prior to the 1994 run period. Because of the use of the supertube support jackets, the tube was simply de-energized and replaced. The array did not have to be dismounted and disassembled, which allowed the experiment to go on with relatively little time lost.

Both strip (4x100cm^2 and pad (16x16cm^2) geometries were used (at different times) and studied. However, an incomplete study of the pad geometries was made, such as determining muon-pion separation efficiencies. The general comparison of the ADC charge spectrum implies that large pads perform well, yet, muon-pion separation with them remains to be analyzed.

The manner in which the LSTs were framed and held between the absorber plates was discussed in section 2.4.2. The final design simply had three rectangular spacers, one that ran the length of the absorber at the bottom and two small one at the upper corners. These allowed the array to be inserted from the side, lifted into position, and supported there by a wooden block underneath. The method was simple, inexpensive, and saved many laborious hours of having to unstack and restack the MuID to change the capacitive pads or strips.

Once the pedestals were subtracted and suppressed, the analysis went forward with little information about the magnitude of the measured charge primarily because the study of the best parameters did not find it to be one of the better discriminating variables. Although the study of best parameters did not choose it, it still may be a worthwhile, maybe even necessary. The pedestal subtraction method could not have been implemented without knowing the charge spectra of both the noise and the streamer signal. Without measuring the charge, one is left with yes-no information that requires on-line adjustment of thresholds in the form of discriminator levels which often fluctuate and are sensitive to slight changes in temperature.

Another argument for the charge measurement is that they may be used to distinguish hodoscopic ambiguities. Because the streamers have a broad charge spectrum, they vary in size and with sufficient ADC resolution one may be able to distinguish streamers on the same plane made by different charged particles. If the streamers are significantly different, then hodoscopic ambiguities may be eliminated by matching the charge sites on one side of the plane with the charge sites on the other side. A study of this was done but nothing conclusive was reached, therefore, this is largely conjecture. However, if the sum of the charge was collected on both sides of a plane of LSTs, it certainly seems feasible.

We compared our results to GEANT simulations and found a slight discrepancy in the hadronic response that could easily be explained by excessive noise in the MuID due to the pedestal subtraction method. The muon curve for the last-plane-hit followed the calculations well, except at low momentum where the RD94 peak was significantly broader. Few GEANT electrons caused any response at all, so no comparison was made there.

4.2 Summary

This dissertation discussed the RD94 Project conducted at the AGS test beam line at BNL. Its aim was to find the levels of muon-pion separation possible using a sampling calorimeter based Muon Identifier and discriminant analysis techniques. Since the discriminant analysis technique is based on separating two gaussian distributions that overlap throughout the entire phase space, separation efficiency is based of setting thresholds between the distributions and gathering all particles that lie above the threshold into one group and the rest into the other group. Knowing how efficient the threshold is requires knowing *a priori* the uncontaminated distributions. We were not afforded such luxury and used a two-step *Filtering* process by which we assumed distributions based on simulated data, separated the data based on the best threshold, then used the separated data to define new distributions. With the new "real" distributions, the data was re-filtered into "real" muon and "real" pion data sets. Performing this on two different data sets allowed one (a training set) to define the distribution and the other (an analysis set) to measure the efficiency. The distribution of one of the discriminant variables, the last plane hit in the MuID, was compared with simulated data for several low and high momenta.

Error was measured by, in a sense, reversing the filtering process. Once the final RD94 distributions were found, simulation data was mixed to levels consistent with raw RD94 data, separated by the filtering process with RD94 filtered data defining the training function, then matched against a second set of simulation data that underwent an equivalent process. The resulting simulation efficiencies were plotted as error on the RD94 efficiencies, revealing a high level of consistency in the process.

Conclusion

The RD94 MuID separates muons and pions to 2% or better at 97% real muon efficiency. At lower momentum the fake pion rate sharply increases to 10% at 1GeV/c due to the thick sampling size in the front end of the MuID. The thickness of the MuID may be reduced to six planes over 5-6λ_I and the lateral segmentation may be reduced to 8cm or more with little degradation in separation efficiency.

BIBLIOGRAPHY

Bibliography

[] **General High Energy.**

[Adair87] R. K. Adair, *Landmarks In Particle Physics At Brookhaven National Laboratory*, Brookhaven Lecture Series, BNL-52129, Number 238, November 18, 1987.

[CDR] PHENIX Collaboration, *Conceptual Design Report*, January 29, 1993.

[CDR Update] PHENIX Collaboration, *Conceptual Design Report Update*, November, 1993.

[Cleymans87] J. Cleymans, J. Fingberg, K. Redlich, *Transverse Momentum Distribution of Dileptons in Different Scenarios for the QCD Phase Transitions*, Physical Review D **33** 7 1 April 1987.

[Dodd] James E. Dodd, *The Ideas of Particle Physics, An Introduction for Scientists*, Cambridge University Press, Cambridge, London, 1984.

[Greiner] Walter Greiner, *Extension of the Periodic Table to New Sectors of Strangeness and Antimatter*. Lecture Given at the Physics Division Seminar, Oak Ridge National Laboratory, September 29, 1995.

[HEIOS3] M. Masera, *Dimuon Production Below Mass 3.1GeV/c^2 in p-W and S-W Reations: A Status Report*, Quark Matter '95, Proceedings of the Ninth International Conference on Ultrarelativistic Nucleus-Nucleus Collisions, Monterey, California, USA, January 9-13, 1995, 93c. North-Holland Publishing Company, 1992.

[JACEE] T. Burnett, et. al., Phys. Rev. Lett. **50** 1983, 2062.

[MatSat] T. Matsui and H. Satz, *J/ψ Suppression by Quark-Gluon Plasma formation* Physics Letters, **B178**, 1986, 416.

[Müller92] B. Müller, *Physics of the Quark-Gluon Plasma*, Lecture given at the NATO Advanced Study Institute, July, 1992.

[Nagamiya] Shoji Nagamiya, *Experimental Overview*, Quark Matter '91, Proceedings of the Ninth International Conference on Ultrarelativistic Nucleus-Nucleus Collisions, Gatlinburg,Tennessee, USA, November 11-15, 1991. North-Holland Publishing Company, 1992.

[Perkins] Donald H. Perkins, *Introduction to High Energy Physics*, Addison-Wesley Publishing Company, 1982.

[Salmeron89] R. A. Salmeron, *An Introduction to the Search of the Quark-Gluon Plasma in Ultrarelativistic Heavy Ion Reactions*, Lectures Delivered at the "Winter School on Quark-Gluon Plasma", Puri Orissa, India, 5-16 December 1989.

[Schochet86] C. Grosso-Pilcher and M. J. Shochet, *High Mass Dilepton Production in Hadron Collisions*, Annual Review of Nuclear Particle Science, 1986.36:1-28.

[Shuryak] E. V. Shuryak and O. Zhirov, Phys. Lett. **B171** (1986) 99.

[Swiatecki] W. Swiatecki, Adapted from *Heavy Ion Reactions at Relativistic Energies* by R. Stock and A. M. Poskanzer, GSI Report 87-10, May 1987.

[Sorensen] The WA80 Collaboration, *Distributions of Transverse Energy and Forward Energy in ^{16}O- and ^{32}S-induced Heavy Ion Collisions at 60 and 200 AGeV*, Physical Review C44 2736, 1991.

[Thomas95] J. Thomas and P. Jacobs, editors, *A Guide to the High Energy Heavy Ion Experiments*, Published in conjunction with the *Quark Matter '95* Conference, UCRL-ID-119181, January, 1995.

[Tserruya] I. Tserruya, *Summary of Low-Mass Dilepton and Direct Photon Results*, Quark Matter '95, Proceedings of the Ninth International Conference on Ultrarelativistic Nucleus-Nucleus Collisions, Monterey, California, USA, January 9-13, 1995, 93c. North-Holland Publishing Company, 1992.

[Van Hove] L. Van Hove, Phys. Lett. **B118** (1982) 138.

[Young92] G. R. Young, *Physics from Photon and Lepton-Pair Spectra*, Invited Paper at the NATO Advanced Study Institute, July, 1992.

[] **Calorimetry.**

[MIRAC89] T. Awes, et. al., *The Mid-Rapidity Calorimeter for the Relativistic Heavy-Ion Experiment WA80 at CERN*, Nuclear Instruments and Methods, A279 (1989) 479-502.

[Brau92] J. Brau, *Simulation of Hadronic Showers and Calorimeters*, Nuclear Instruments and Methods, A312 (1992) 483-514.

[Catanesi90] M. G. Catanesi, et. al., *Hadron Showers in an Iron-Streamer Tube Sampling Calorimeter*, Nuclear Instruments and Methods, A292 (1990) 97-112.

[Cornell94] E. Cornell, et. al., *Calorimeter/Absorber Optimization for a Relativistic Heavy Ion Collider Dimuon Experiment*, Ph. D. Thesis, Vanderbilt University, 1995, also Nuclear Instruments and Methods, A350 (1994) 150-173.

[Fabjan77] C. W. Fabjan, et. al., *Iron Liquid-Argon and Uranium Liquid-Argon Calorimeters for Hadron Energy Measurement*, Nuclear Instruments and Methods, 141 (1977) 61-80.

[Fabjan82] C. W. Fabjan and T. Ludlam, *Calorimetry in High Energy Physics*, Annual Review of Nuclear Particle Science 1982. 32:335-89

[Fernow86] R. Fernow, *Introduction to Experimental Particle Physics*, Cambridge University Press, Cambridge, Mass. 1986

[Fesefeldt90] H. Fesefeldt, Th. Hamacher, and J. Schug, *Tests of Punch-Through Simulations*, Nuclear Instruments and Methods, A292 (1990) 279-312.

[Mincer85] A. I. Mincer, et. al., *Measurements of the Response of a Hadronic Calorimeter to Beams of Pions and Protons of 1-10 GeV/c Momenta*, Nuclear Instruments and Methods, A235 (1985) 46-54.

[Sessoms79] A. L. Sessoms, et. al., *The Segmented Calorimeter: A Study of Hadron Structure*, Nuclear Instruments and Methods, 161 (1979) 371-382.

[ZDC89] G. Young, et. al., *The Zero-Degree Calorimeter for the Relativistic Heavy-Ion Experiment WA80 at CERN*, Nuclear Instruments and Methods, A279 (1989) 503-517.

[] **Limited Streamer Mode Tubes and Phenomena.**

[Battistoni80] G. Battistoni, et. al., *Resistive Cathode Detectors with Bidimensional Strip Readout: Tubes and Drift Chambers*, Nuclear Instruments and Methods, 176 (1980) 279-303.

[Battistoni82] G. Battistoni, et. al., *Resistive Cathode Transparency*, Nuclear Instruments and Methods, 202 (1982) 459-464.

[Battistoni86] G. Battistoni, et. al., *A High Voltage Network for Streamer Tubes*, Nuclear Instruments and Methods, A251 (1986) 286-291.

[Ellila87] M. Ellila, et. al., *Limited Streamer Mode Detectors for Mass Production*, DELPHI 87-109 CAL 54, 21 December 1987.

[Iarocci83] E. Iarocci, *Plastic Streamer Tubes and their Apllications in High Energy Physics*, Nuclear Instruments and Methods, 217 (1983) 30-42.

[Palladino74] V. Palladino and B. Sadoulet, *Application of the Classical Theory of Electrons in Gases to Multiwire Proportional and Drift Chambers*, Lawrence Berkely Laboratory Report LBL-3013, 1974.

[Sharma92] A. Sharma and F. Sauli, *A Measurement of the First Townsend Coefficient in Argon Bases Mixtures at High Fields*, Nuclear Instruments and Methods, A323 (1992) 280-283.

[] **Discriminant Function Analysis.**

[Awes89] T. Awes, *A Neural-Network Approach to the Problem of Photon-Pair Combinatorics*, Nuclear Instuments and Methods, A276 (1989) 468-481.

[Stankus94] P. Stankus, *A Few Words About Discrimination Analysis*, PHENIX Technical Note Phenix-Muon-94-3 (http://www.bnl.gov).

[Coomans86] D. Coomans and I. Broeckaert, *Potential Pattern Recognition in Chemical and Medical Decision Making*, Research Studies Press, 1986.

[Hand81] D. J. Hand, *Discrimination and Classification*, John Wiley: Chichester, 1981.

[Lindley65] D. V. Lindley, *Introduction to Probability and Statistics from a Bayesian Viewpoint*, Cambridge Univerity Press, London, 1965.

[] **Other References.**

[Carroll] Alan Carrol, Liaison Physicist, Brookhaven National Laboratory. Personal Communication.

[FNAL] Electronically downloaded from the World-Wide-Web site http://fnnews.fnal.gov/hep_overview.html.

[Guidry] Personal Communication.

[GEANT] GEANT – Detector Description and Simulation Tool, CERN, Geneva, Switzerland 1993.

[Latex] L. Lamport, LaTeX: A Document Preparation System, Addison-Wesley Publishing Company, Reading, Massachusettes, 1986.

[PDG92] editors L. S. Brown, D. L. Nordstrom, and S. G. Brown, Review of Particle Properties, Physical Review D, Vol. 45, No. 11, Part II, June 1, 1992.

APPENDICES

Appendix A

Time of Flight and β

With momentum below 3GeV/c, one the most salient characteristics that can be used to distinguish different particles of equal momentum is their time-of-flight (TOF). In our experiment, RD94, we arranged three "start" counters centered on the beam axis at fixed positions which measured the times at which the particle passed through the counters. Each counter was a 0.5cm thick plastic scintillator with two photomultiplier tubes coupled to it via wave-guides extruded from lucite. The phototubes were placed on opposing sides of the scintillator and were given names "East" and "West". The cross-sectional area covered by each varied but all were of the order of 50-100cm^2. The counters were labeled S2, S3, and S4; S2 was closest to the production target and S4 East's signal was considered t_0 for all events. By choosing a momentum, measuring the distance between each start counter, and measuring the time each counter was hit, we can then calculate the velocity ($\beta = v/c$) and the mass of the particle. This report is a description of the methods used to calibrate the detectors' time signals, calculate β, and identify particles.

We begin first by choosing one particular low momentum run to use in calibration. We select a 1.0GeV/c, Minimum-Bias, positive polarity run for the following reasons:

the on-line, Minimum-Bias trigger performed no particle selection so the entire beam profile would be seen at once, meaning that all particle species are present in the run. The positive polarity was chosen to bring protons into the profile and the 1.0GeV/c momentum was selected to obtain the largest time separation between the positron and proton time measurements. This run should provide us with all the necessary tools to optimize the calibration the TOF system.

Assumptions

We begin by assuming that the positron beta (β_e) is 1 and that the positions of all the start counters are known exactly. At 1GeV/c, $\beta_e = 0.9999998694395$, so assuming it is exactly 1 is good to the 7^{th} decimal place. The detector positions are known to within 2cm so, since the distance between the reference counter and the next closer counter is 2006cm, error in beta due to location error will be about 0.1% yielding an error in momentum measurement of no more than 0.2%. In addition to these assumptions, we further assume that the TDCs on the reference counter are calibrated exactly. Since it provides t_0, this assumption about S4 should not add error to the time measurement.

Calibration

The first step in calibrating the TOF measurement is to define positron and proton timing peaks for each PMT. This step requires the use of the Cerenkov counters, whose thresholds were appropriately set to logically define certain particles or groups of particles. The threshold of C1 was set high so that only electrons emitted enough light to be detected. C2's threshold was set a little lower so that muons and pions or lighter particles would fire it. Hence, electrons/positrons are defined by logically "ANDing" C1 and C2. Protons are defined by ANDing the "NOT" of C1 and C2. We can see in figure 3-2 that when both C1 and C2 fire they do so within a certain Δt, forming the diagonal line in the figure. We then call hits along that line electrons/positrons and define the cut

$$-150. < (c1(tdc) - 517.) - c2(tdc) < 150.$$

Since the positron velocity (β_{e^+}) changes very little within the momentum range used in the entire experiment (1-9GeV/c), this cut, unaltered, will define a positron(e^+) or electron(e^-) regardless of momentum. The proton(p^+) peak is easily discernible at low momenta (i.e. 1GeV/c), even without using the Cerenkov logic (i.e. not C1 and not C2).

Table A.1: Positron and Proton timing peak means and detector positions relative to S4. $\Delta_{e,p}$ is the difference between positron and proton timing means.

	tdc_{e^+}	tdc_{p^+}	$\Delta_{e,p}$	$d(cm)$
S2 East	1012.2	298.25	713.95	2733.04
S2 West	927.12	217.02	710.10	2733.04
S3 East	773.09	241.25	531.84	2006.60
S3 West	688.14	149.66	538.48	2006.60
S4 East	296.11	296.11	0.0	0.0
S4 West	216.96	216.96	0.0	0.0

Once the e^+ and p^+ peaks are defined, the next step in calibration is to measure their means (see table A.1). We then establish the relationship which equates the TDC channel scale to the real time scale, here we will use nanoseconds.

$$t = (tdc_{raw} - tdc_{e^+})\,0.05ns/ch\,(1 - \epsilon) + t_{e^+} \tag{A.1}$$

where t $\equiv$ calibrated time in ns

$\epsilon \equiv$ calibration factor

$tdc_{raw} \equiv$ raw tdc channel

$tdc_{e^+} \equiv$ tdc channel of positron peak

$t_{e^+} \equiv$ expected e^+ arrival time

From eq. A.1 we see that when $tdc_{raw} = tdc_{e^+}$, then $t = t_{e^+}$, meaning that this relation places the positron peak at the correct point in time.

Next, we establish the beam momentum. We set ϵ to zero (i.e. assume that the TDCs are calibrated) and let $\beta_e = 1$ which implies $t_{e^+} = d/c$. Rewriting eq. A.1 we get

$$t = (tdc_{raw} - tdc_{e^+})\,0.05ns/ch - d/c \tag{A.2}$$

where $d \equiv$ distance between S4 and either S2 or S3

$c \equiv$ speed of light

For each detector, we have two PMTs, which give us six position-time coordinate pairs for the proton time peaks which we can plot and fit a line to (see figures A-1 and A-2). Since our reference point is S4, it has coordinate pair values of (0,0) and we force the fitted line to pass through this point. We thus obtain a proton velocity of 21.5096cm/ns, a proton beta of 0.7175 and a corresponding momentum of 0.96644GeV/c.

Next, we solve eq. A.1 for ϵ, giving us

$$\epsilon = 1 - \left(\frac{1}{0.05c}\right)\left(\frac{1-\beta_p}{\beta_p}\right)\left(\frac{d}{\Delta_{e,p}}\right) \tag{A.3}$$

where we have substituted in proton values for $t \to t_p$ and $tdc_{raw} \to tdc_p$ and let $t_p = d/(c\beta_p)$. For each detector then we can find the corresponding calibration factor,

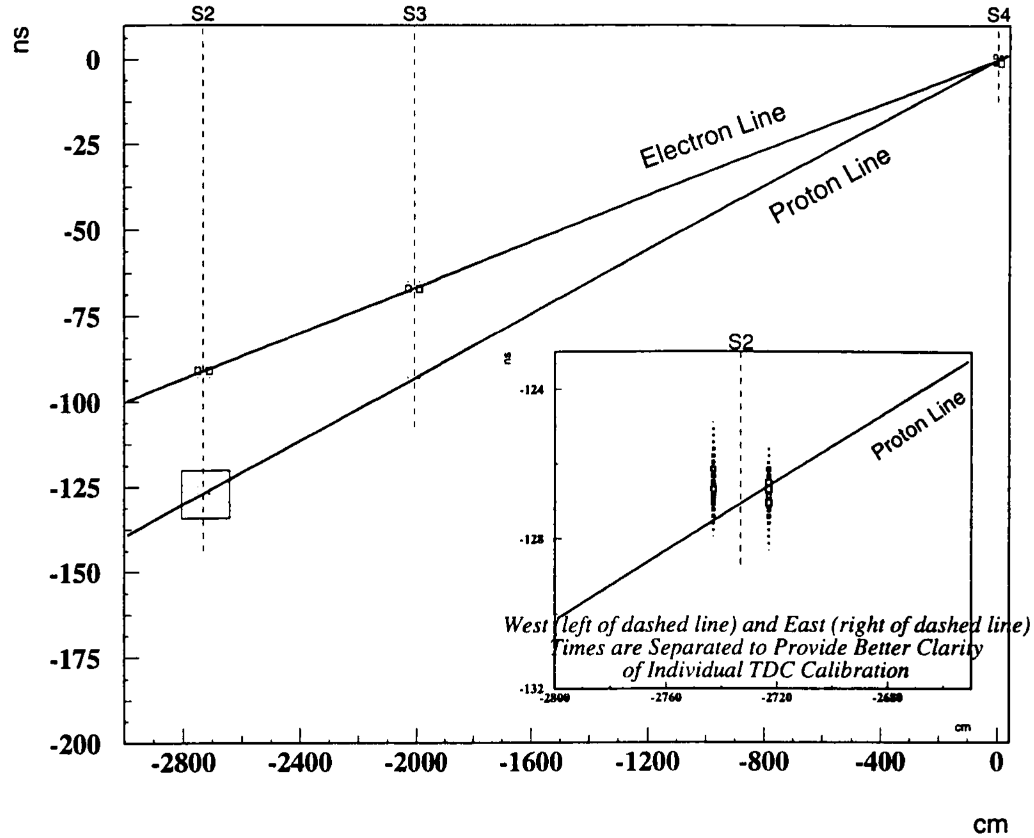

Figure A-1: The uncalibrated start counter hit time for positrons and protons for each detector is plotted versus the detector position. The proton line is fitted to the uncalibrated proton peaks. The insert is a magnification of the box drawn around S2's proton peaks.

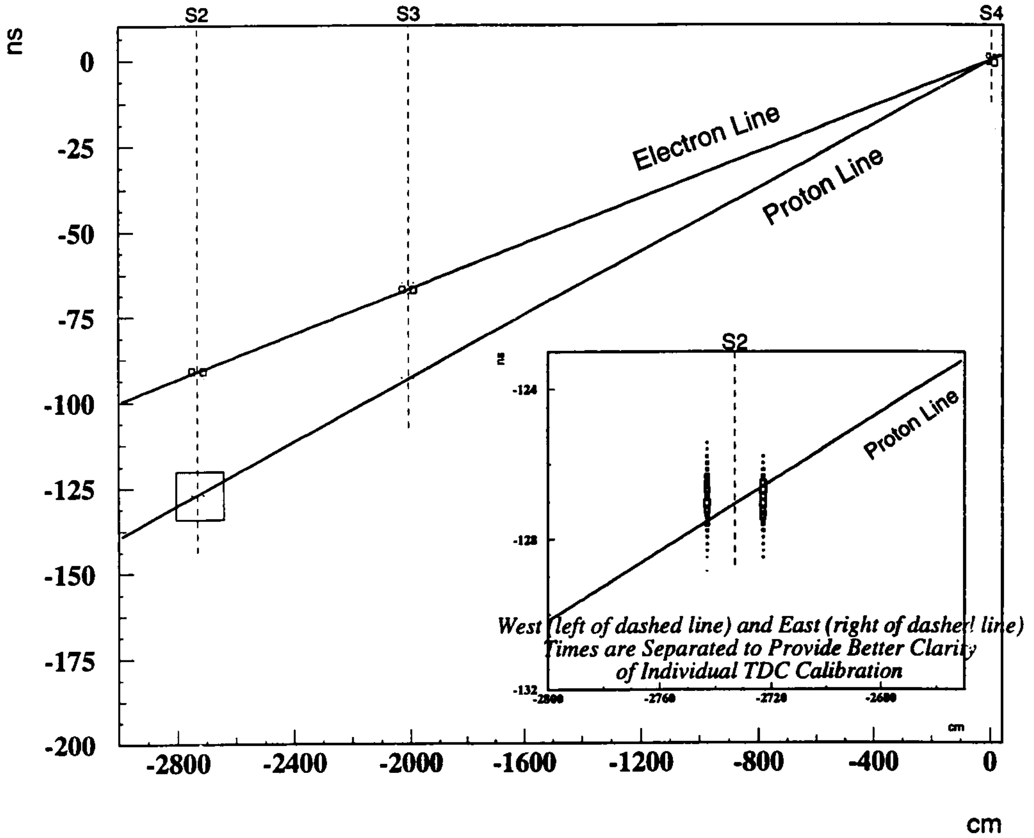

Figure A-2: The calibrated start counter hit time for positrons and protons for each detector is plotted versus the detector position. The calibrated proton peaks intersect proton line and the detector position line (see insert).

ϵ (see table A.2) and using eq. A.1, we can then find the actual time that each detector

Table A.2: TDC calibration factors for each PMT in the TOF system.

	ϵ
S2 East	- 0.00558
S2 West	- 0.01103
S3 East	+ 0.00890
S3 West	+ 0.02112
S4 East	0.0
S4 West	0.0

was hit and thus find the particle velocity. In table A.2 we see the errors are most extreme on the West sides. We can use both S2 West and S3 West to then define the range of uncertainty of the momentum measurement. S2 West estimates momentum high by 0.64% and S3 West estimates momentum low by 1.2%. For brevity, we will simply say the error on the momentum measurement is 1.0%.

β Measurement

Using eq. A.1 we then have six time measurements, two from each counter. Each of these measurements is known to within a certain degree of accuracy based on the width (σ) of the East and West time difference for each counter. With the time measurements, their accuracies, and the detector positions, we can perform a least-squares fit to the following equation

$$t = z * (1/v) - z0 * (1/v)$$

to find v and $z0$ for each event.

With velocity found, we divide by c to get β (see figures A-3, A-4, A-5, and

A-6), and compare to the expected $\beta_{particle}$ of several particle types. If $|\ (\beta - \beta_{particle})/\beta_{particle}\ |$ is less than ~2.0%, the particle is considered identified (see figure A-7). We base the percentage on the uncertainty of the momentum measurement and the width of the β_p. It can be shown that

$$\frac{\sigma_P}{P} = \frac{\sigma_\beta}{\beta}$$

so since the width(σ) of the proton peak in figure A-3a is approximately 0.0035, the momentum range is approximately 0.5%. The total uncertainty in the momentum measurement is then $\pm \sim 1.7\%$. Figures A-7b, A-7c and A-7d show the results of β calculation for runs of higher momentum using the same calibration constants.

Anomalous β Peaks

In the low momentum β spectra we see two peaks that do not correspond to identified particle peaks in figure A-7. The lowest momentum case, 1GeV/c, does show two extra peaks but they vanish after gates are applied (see fig A-3). In contrast, applying stricter time and χ^2 cuts to the higher momentum cases enhances the anomalies, implying that the anomalous peaks in the 1GeV/c case are artifacts from the calculation of β, and the anomalies in the higher momentum cases arise from something physical. Moreover, the anomalous peaks in the higher momentum cases can be seen in the raw tdc spectra, lending credence to their physicality (see for example figure A-8).

Just what is causing the peaks is not understood. The beam is directed from the target region by two dipole (bending) magnets in tandem with adjacent quadrupole (focusing) magnets. The magnetic fields (B) of the bending magnets can be set to select a desired beam momentum (P) by adjusting the magnet current and the

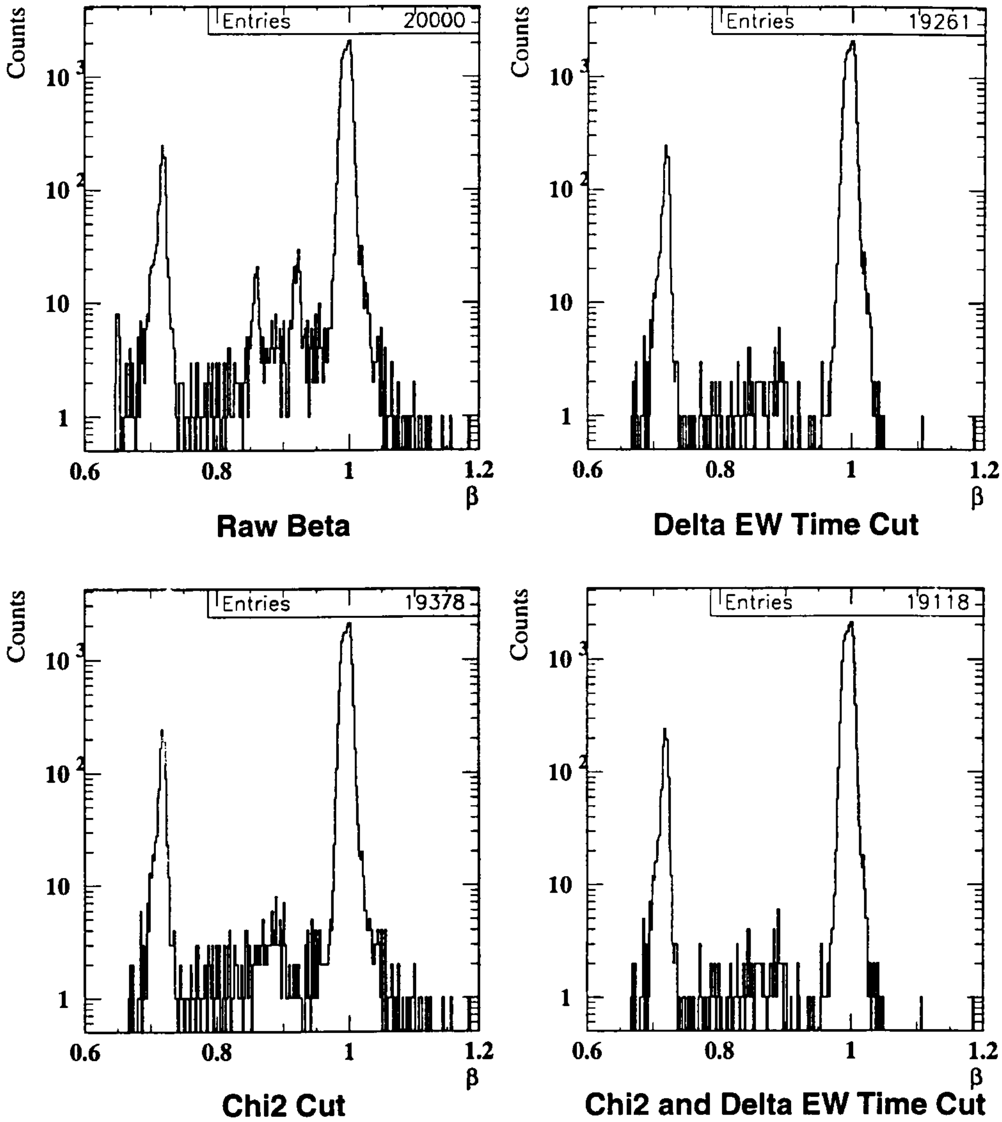

Figure A-3: 1GeV/c beta spectrum showing effects of timing cuts (East time - West time < ±2ns) and velocity fit cuts ($\chi^2 < 0.00064$).

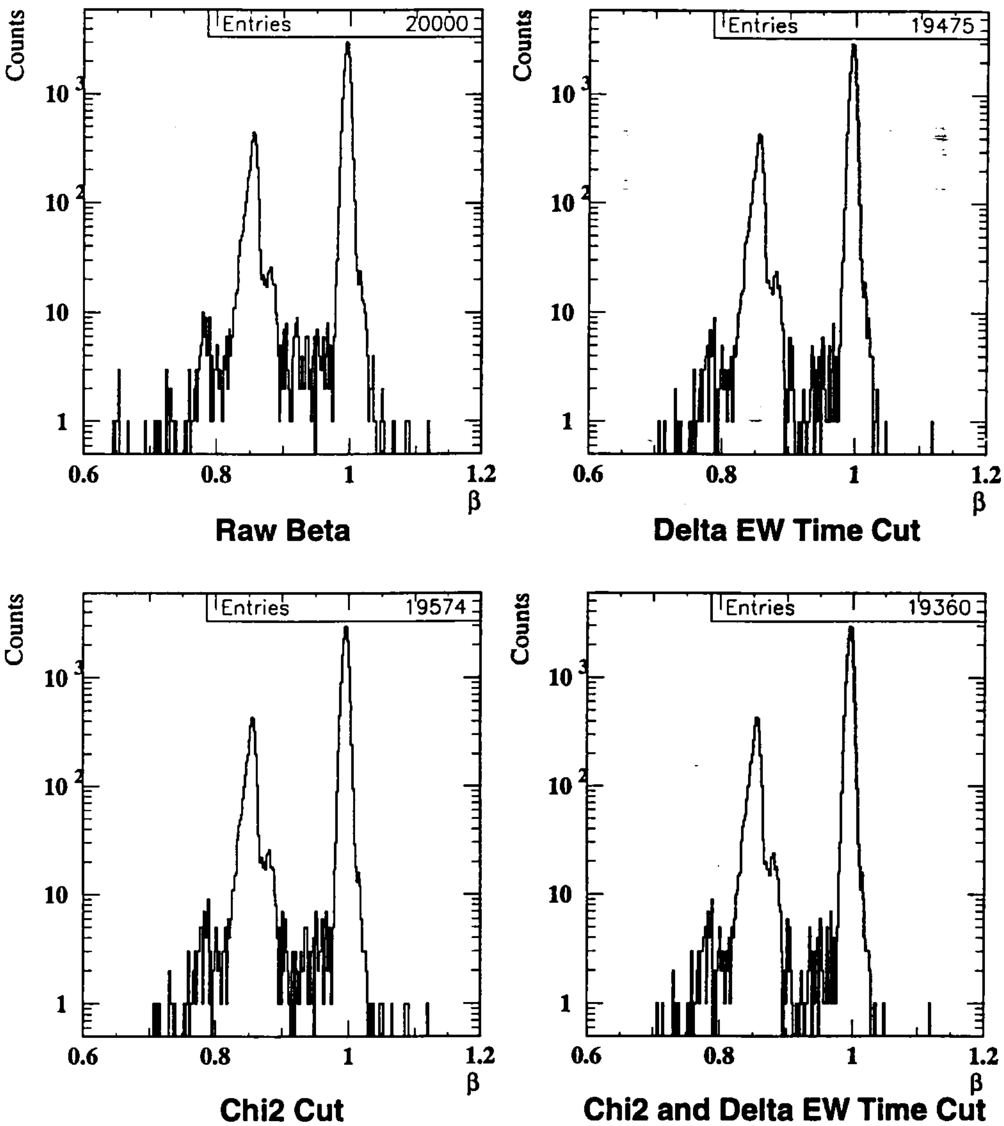

Figure A-4: 1.5GeV/c beta spectrum showing effects of timing cuts (East time - West time < $\pm$2ns) and velocity fit cuts ($\chi^2 < 0.00064$).

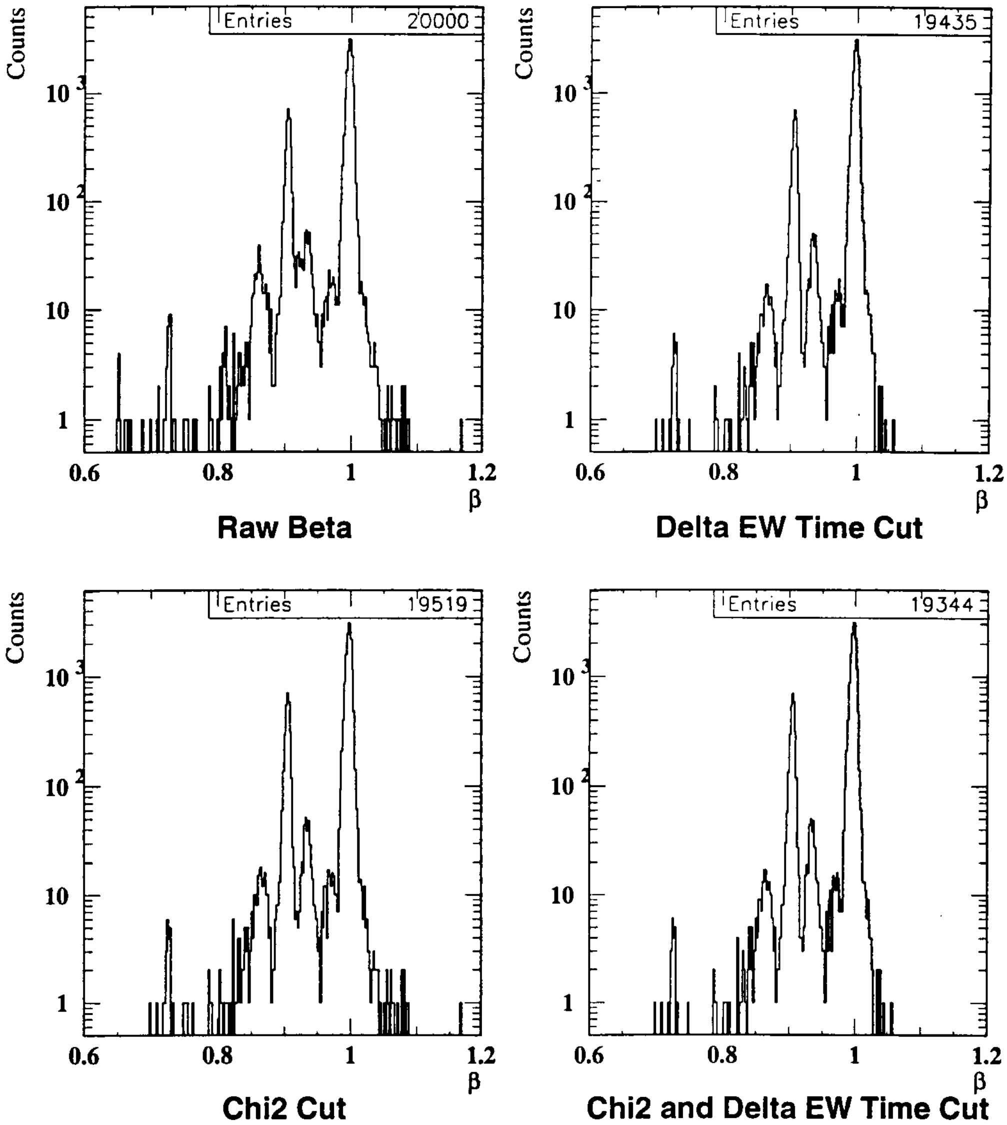

Figure A-5: 2GeV/c beta spectrum showing effects of timing cuts (East time - West time < $\pm$2ns) and velocity fit cuts ($\chi^2 < 0.00064$).

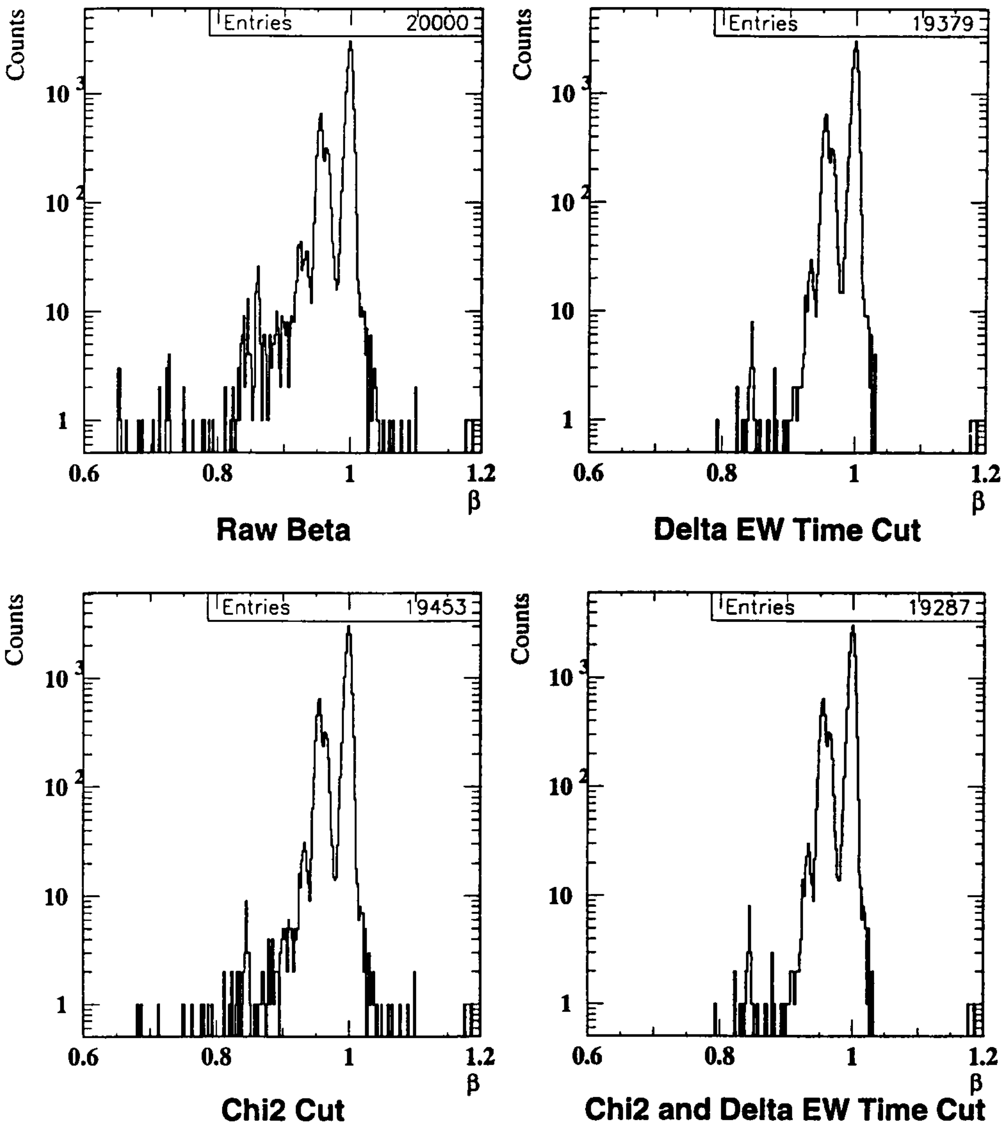

Figure A-6: 3GeV/c beta spectrum showing effects of timing cuts (East time - West time < ±2ns) and velocity fit cuts ($\chi^2 < 0.00064$).

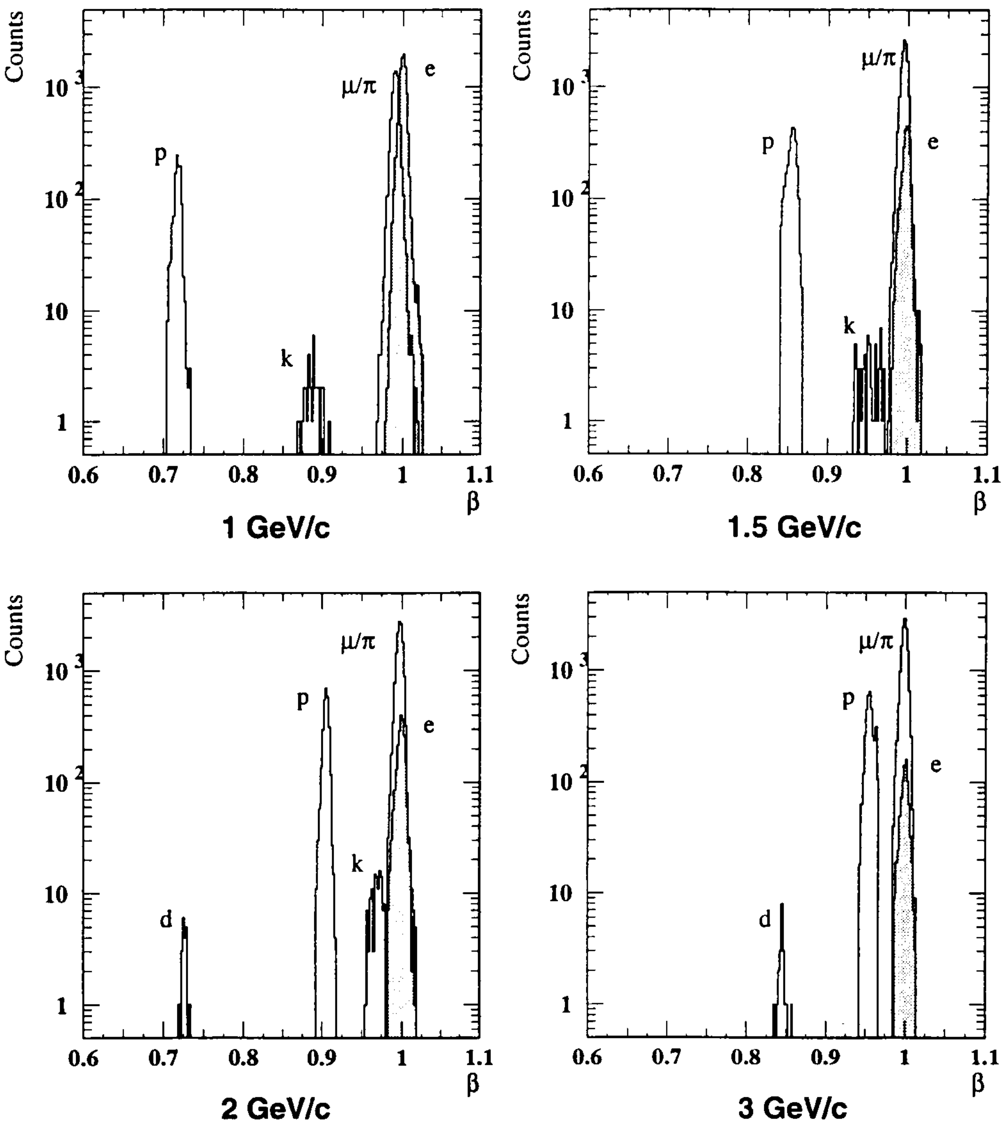

Figure A-7: Beta spectra for minimum bias runs with momentum $\leq$3GeV/c.

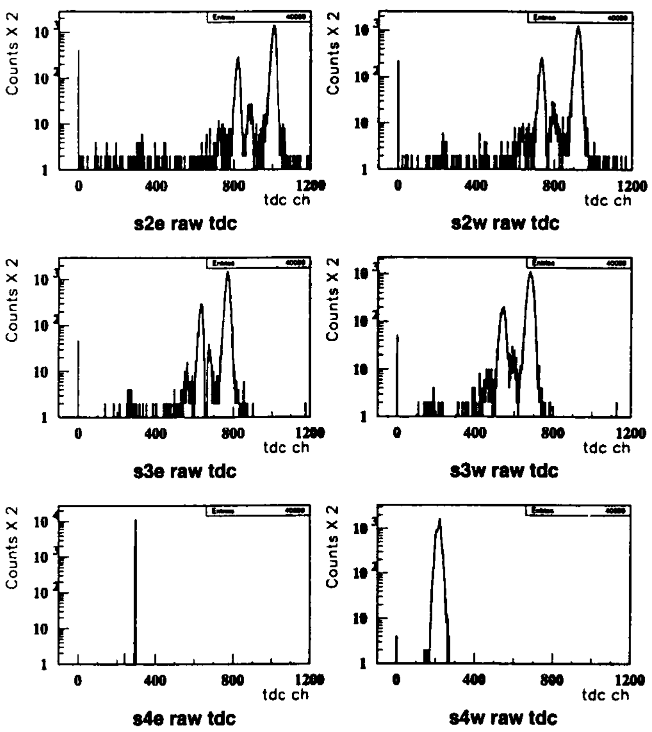

Figure A-8: Raw TDC spectra of the start counters at 2GeV/c.

relationship between B and P is the cyclotron formula

$$P = rqB$$

where q is the charge on the particle and r is the bending radius. B is constant in the run and r is defined by the position of the target and start counters in relation to the magnets. Therefore, the common characteristic of all beam particles is the P/q. All particles under consideration in this experiment have the same magnitude of charge, $\pm e$, so they all have then the same momentum. However, the beam does not limit itself to our considerations and particles with different q may possibly be found in the beam.

For instance, since He_2^4 has twice the charge as a proton, the magnet settings that define a 2GeV/c proton would also define a 4GeV/c helium nucleus, which would give the helium nucleus a β of 0.732. Coincidentally, the same magnet settings would pick out a 2GeV deuterium nucleus having the same β of 0.732 approximately.

Unfortunately, this does not solve the problem; not only because the anomalous peaks lie at different β, but because the production cross sections for these higher mass species make their likelihood prohibitively small. A more likely explanation would be a broadening of the proton spectrum caused by some anomaly in the beam optics that occurs above 1GeV/c. If this is the case, then the error analysis presented in this report would need revision.

Muon-Pion Separation with Time-of-Flight

The last question to answer with time-of-flight as far as RD94 is concerned is to determine if we can use it to distinguish muons from pions. Figure A-9 describes the levels of resolution needed to distinguish muons and pions, given that the momentum of both particles is known and equivalent. The timing resolution in our case was

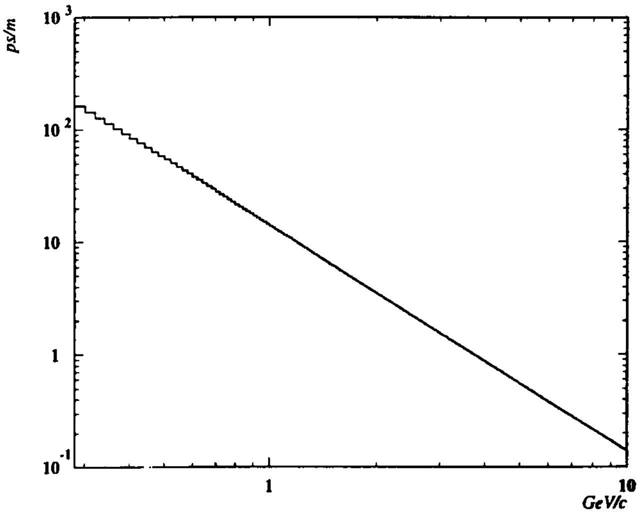

Figure A-9: The minimum TOF resolution needed to separate muons from pions, measured in picoseconds/meter, decreases as momentum increases. This curve is the difference in the inverse βs of muons and pions, divided by c.

determined from the difference in the hit times of two counters, for instance, East and West. We measured 10, 14, and 12 TDC channels, for S2, S3, and S4, respectively. Considering the average width, 12 channels, we have about 240ps over about 27m giving about 9ps/m. Only at 1GeV/c do we have sufficient resolution to distinguish them.

However, in considering the spread in momentum, we find little hope in separating muons and pions at any momentum. Figure A-10 shows the uncertainty in distinguishing muons and pions given various spreads in momenta. The spread in momenta is largely due to inaccuracies with the bending and focusing magnets and we mentioned above that the the error in determining momentum was about 1.7%. Judging from figure A-10, we have about a 90-95% uncertainty in distinguishing muons from pions at 1GeV/c. Figure A-10 is the ratio of the overlap of two gaussian curves to

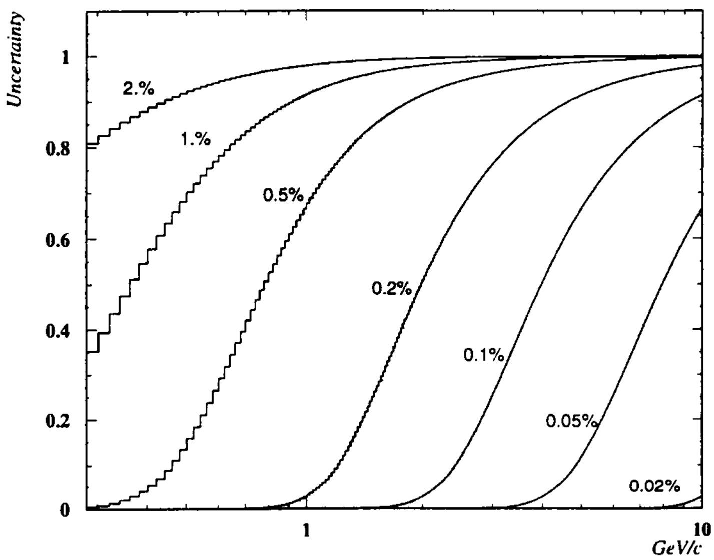

Figure A-10: Uncertainty in identifying muons and pions arising from momentum uncertainty. These curves are calculated by the ratio of the integral of the overlap of 2 gaussian curves to the average integral of both gaussians. As the spread in momentum increases, the gaussians overlap more, causing higher uncertainty in identification.

the average area of the two gaussians. Both gaussians have their means at the β for a muon or pion for a given momentum and their widths are equal (the average of their widths for a given momentum spread).

Appendix B

Pedestal Subtraction

Analysis of the data taken for the μID experiment began shortly after the experiment ended, with the initial goal of determining its quantity and quality. Due to the slow timing characteristics of the Limited Streamer Mode Tube and 70 meter signal cable length to the ADC, the relatively weak (10 pC) signal pulse required an ADC integration time of approximately 200ns. The signal was thus not completely distinguishable from the noise and the initial goal of analysis was to determine if any data was missed (quantity) and how well it could be distinguished from the noise (quality).

In order to determine the quantity of data, a few select ADC channels which were known to work consistently were histogrammed for each event record. If the ADC values held constant values, the run was declared partially or completely lost, depending, of course, on how may events actually had that same, constant value. It was determined that the fast bus 2V power supply was faulty and often in the middle of a run the fast bus simply stopped working. This happened no fewer than five times, rendering five runs partially lost and five subsequent runs completely lost.

After the partially and completely lost runs were completely found, the decision was made to overhaul the analysis package in order to incorporate fortran structures. It was reported that this device worked well in other analysis packages and once learned, their advantages are striking. For instance, because a particular channel had been addressed by a variable designated by the electronics crate number(i.e. c2), slot number(i.e. n13), and channel number(i.e. 5), altogether adc_c2_n13(5), the variable name contained no physical detector information. In using fortran structures that same parameter is stored in the variable m(2).e(5).adc, yielding the detector information M#2, east side, detector #5. Changing the variable from adc_c2_n13(5) to m(2).e(5).adc obviously adds quite a bit of transparency to analysis. For those unfamiliar with the structure statement, they are in a sense, arrays wherein elements need not be the same data type, such as integer or character. Thus, one may build a structure that associates a name with a number with an ADC value with a logical value, and so on.

With an working, modified analysis package, noise measurement began as simple gaussian fits to in- and out- of-beam pedestals. Comparison of these in- and out-of-beam pedestals showed that the in-beam pedestal was wider and the mean shifted, clearly calling for a better method of noise measurement. For channels with good statistics, the in-beam pedestal shifted up compared to the pulser; for channels with low statistics, the in-beam pedestal shifted down. The conclusion was that we needed to accurately determine the in-beam pedestal and, moreover, to pin-point the channel where the data and pedestal merge (hereafter called the threshold). The latest scenario in pedestal measurement uses the in- and out-of-beam pedestals to define a range wherein a pedestal mean and width are chosen, incorporated into a gaussian function and subtracted from the raw data [see fig. B-1]. The remainder above the gaussian's mean is fitted with a poisson curve which is then associated with that mean and width. Nine sets of means and widths within the defined range are chosen and the best associated poisson fit (based on minimum χ^2) then selects the best mean-width set. The method iterates 3 times, with the selected mean-width set defining a new, tighter range. The mean-width set selected at the last iteration then defines the pedestal.

There are two advantages to this method. 1) The threshold is accurately determined. The intersection of the gaussian and poisson fits sits right at the shoulder where the pedestal starts to encroach on the real data. This point, the threshold, provides the best point of separation between pedestal noise and data. 2) Using the fitted functions themselves, a range can be defined about the threshold for minor deviations from it. Presently, the range is defined according to the ratio

$$\frac{poisson(x) - gaussian(x)}{poisson(x) + gaussian(x)}$$

A simple difference divided by sum. The ratio is -1.0 where the poisson function is small (which is at the pedestal mean), 0.0 where the functions are equal (at the threshold), and +1.0 where the gaussian function is small. Since the gaussian is defined for all channels, small is defined as less than 1.

The disadvantage of this method is computation time. Approximately 3 days on a VAXstation 3100 are needed for one run. Another disadvantage is that pedestals are not accurately determined. The pedestal fit is determined by how well a poisson curve fits the raw data. Since the in-beam pedestals broaden a little at their base, the pedestal fit gets shifted up a few channels to align the fit with the edge of this broadening [see fig. B-1]. The result is an accurate threshold measurement but inaccurate pedestal measurement. Since the pulse-heights were much lower than what we worked with in the past (order 50-100mV) leaving much of the signal buried in the pedestal, accurate determination of the threshold is paramount. Figure B-2 compares the hit profiles in nine of the ten active layers of the identifier using two methods of

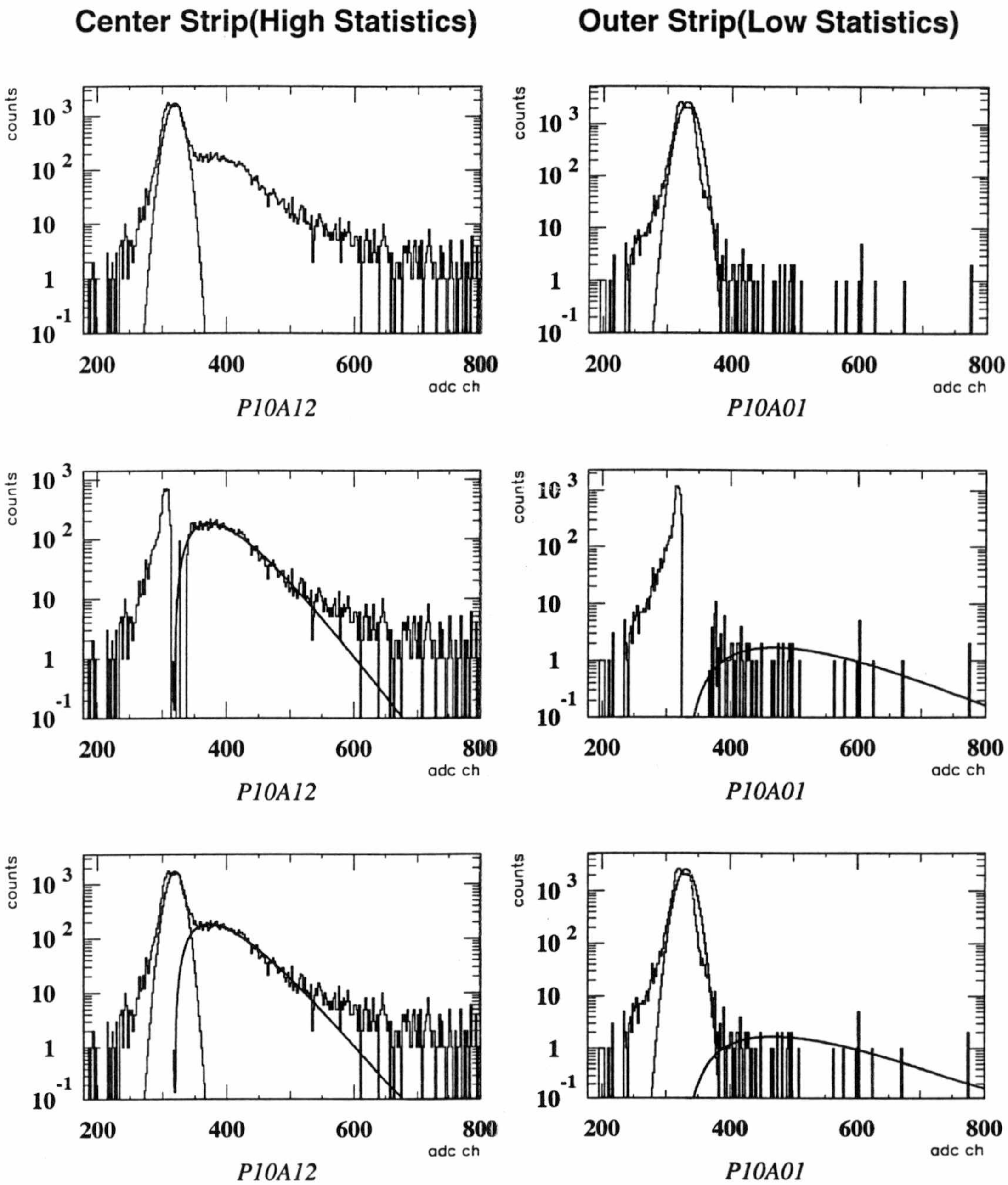

Figure B-1: **Top**: raw data with selected gaussian fit to pedestal. **Middle**: poisson fit to raw data after gaussian fit is subtracted. **Bottom**: raw data with both gaussian and poisson fits superimposed.

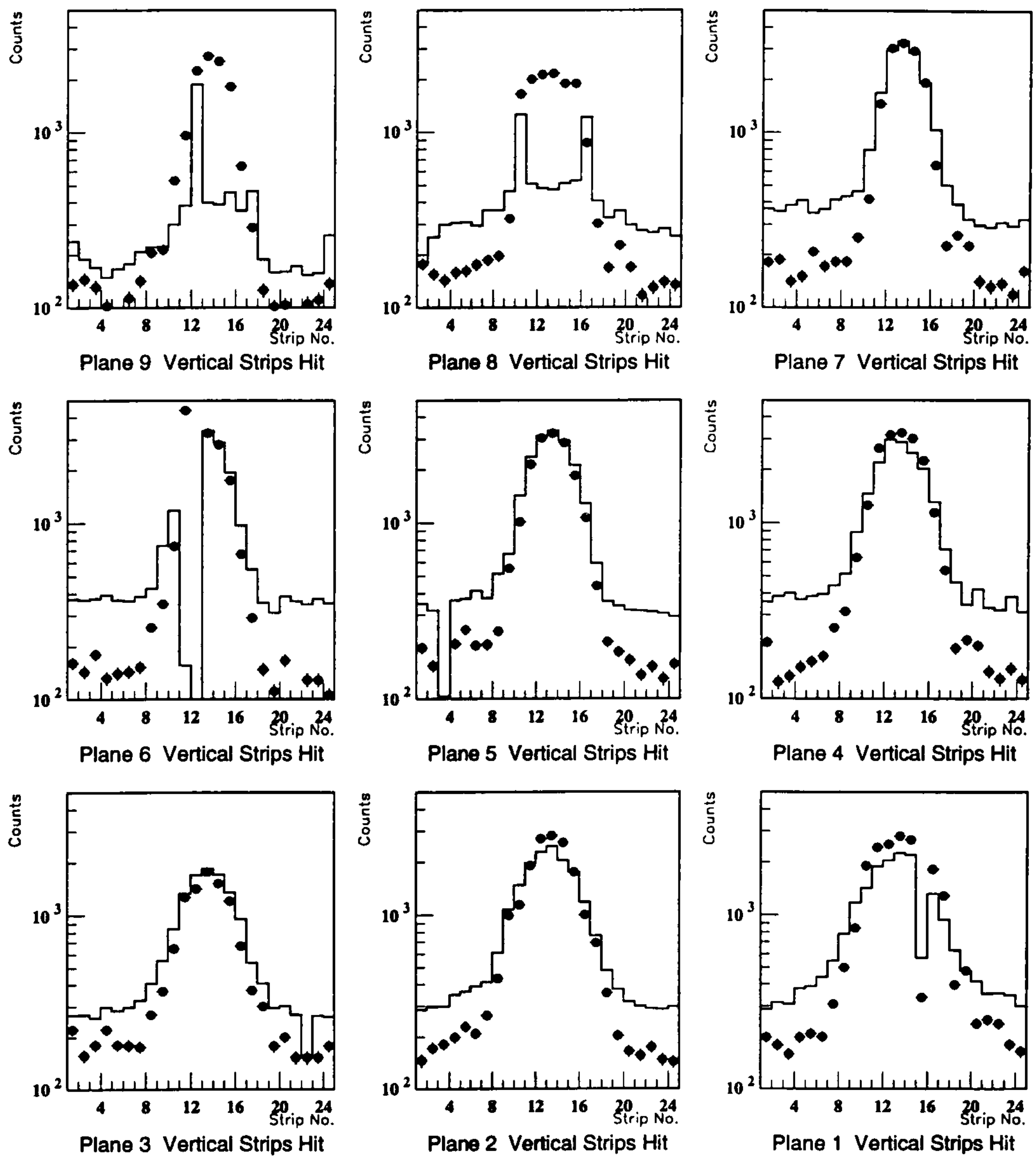

Figure B-2: Hit profiles for each vertical strip in 9 of the 10 LST planes. Method 1, shown by the bar histogram, used gaussian fits to the pedestal. Hits then had to be above the mean plus a constant (here 2.0) times the pedestal width. Method 2, shown by closed circles, used the threshold as determined by the best poisson fit to raw data above a pedestal.

pedestal subtraction. One method, represented by the bar histogram, measured the pedestals by fitting the pedestal with a gaussian, then subtracting the mean value of the gaussian and a constant times the width. Any ADC value greater that that was considered "hit". The second method, represented by the closed circles, measured the threshold, as opposed to the pedestal by the method described above using poisson fits to raw data. Clearly, the second method presents a truer representation of the hit distribution through the identifier.

m

Appendix C

Run Statistics

Included in this appendix are tables of all successful runs in both RD93 and RD94. Each table has three main columns: *Characteristics*, *Events* and *Rates & Averages*. A fourth column simply lists the associated run number. Each table is ordered and delineated by momentum and with particle type listed in the following order: *mb*(min-bias), μ(muon), π(pion), e(electron/positron), *and* p(proton). Each column has the following subcolumns.

- *Characteristics*
  1. **Mom**: The run momentum in units of GeV/c
  2. **ID**: Particle identification
  3. **Time**: Run time in minutes
- *Events*
  1. **#Tot Evts**: Total number of events recorded
  2. **#Phys Evts**: Physics events
  3. **#Puls Evts**: Pulser events

4. **#EoS Evts**: End-of-Spill events
5. **#Unk Evts**: Unknown event type (improper event record length)

- *Rates & Averages*
    1. **Spls/Min**: Number of spills per minute
    2. **Evts/Min**: Number of events per minute
    3. **Phys/Spl**: Number of physics events per Spill

Table C.1: RD93 run statistics with strips installed.

	RD93 Data Statistics (Strips)											
	Characteristics			*Events*					*Rates & Averages*			
Run	Mom (GeV/c)	ID	Time (min)	#Tot Evts	#Phys Evts	#Puls Evts	#EoS Evts	#Unk Evts	Spls/ Min	Evts/ Min	Phys/ Spl
41	+1.0	*mb*	23.30	31357	30097	890	366	2	15.71	1291.72	82.23
42	+1.0	e^+	87.08	32782	28051	3352	1375	2	15.79	322.12	20.40
36	+1.5	*mb*	29.53	48060	46462	1131	464	2	15.71	1573.21	100.13
39	+1.5	e^+	49.45	22024	19338	1902	780	2	15.77	391.06	24.79
40	+1.5	e^+	25.33	9998	8622	974	400	1	15.79	340.34	21.56
19	+2.0	*mb*	32.55	51867	50105	1246	510	4	15.67	1539.32	98.25
23	+2.0	μ^+	9.28	13284	12788	349	144	2	15.51	1377.52	88.81
21	+2.0	π^+	26.90	40192	38733	1032	423	2	15.72	1439.89	91.57
22	+2.0	e^+	59.40	37343	34118	2284	938	1	15.79	574.38	36.37
20	+2.0	p^+	20.88	33406	32277	796	328	2	15.71	1545.59	98.41
44	+3.0	*mb*	24.28	33862	32557	919	371	13	15.28	1340.71	87.75
47	+3.0	μ^+	36.72	39158	37207	1377	563	9	15.33	1013.35	66.09
45	+3.0	π^+	40.87	31411	29621	1259	512	17	12.53	724.82	57.85
48	+3.0	e^+	83.05	31304	26791	3198	1312	1	15.80	322.59	20.42
46	+3.0	p^+	24.52	29105	27790	927	377	10	15.38	1133.51	73.71
49	+4.0	μ^+	47.67	66550	64009	1798	738	4	15.48	1342.85	86.73
50	+4.0	μ^+	28.55	42015	40470	1092	449	2	15.73	1417.51	90.13
28	+4.0	π^+	26.68	36284	34870	998	407	7	15.25	1306.81	85.68
27	+4.0	e^+	73.27	30070	26091	2819	1157	1	15.79	356.11	22.55
29	+4.0	p^+	30.38	40583	38940	1161	475	5	15.63	1281.62	81.98
18	+6.0	e^+	32.77	46278	44505	1253	512	7	15.63	1358.24	86.92
17	+6.0	p^+	24.35	38961	37642	931	381	4	15.65	1545.87	98.80
30	+8.0	*mb*	28.12	43148	41627	1075	442	2	15.72	1480.51	94.18
35	+8.0	μ^+	20.48	31953	30844	783	322	2	15.72	1505.81	95.79
33	+8.0	π^+	19.62	32312	31251	750	308	2	15.70	1593.08	101.46
31	+8.0	e^+	23.53	10730	9454	901	371	2	15.76	401.73	25.48
32	+8.0	e^+	35.33	22395	20472	1362	558	1	15.79	579.40	36.69
34	+8.0	p^+	26.50	43341	41903	1017	417	2	15.74	1581.25	100.49
13	−6.0	*mb*	20.73	31180	30064	784	323	5	15.58	1450.03	93.08
16	−6.0	μ^-	24.80	41642	40265	943	375	18	15.12	1623.59	107.37
14	−6.0	π^+	7.48	11554	11149	282	117	2	15.63	1489.84	95.29
15	−6.0	π^+	25.55	36971	35588	976	400	4	15.66	1392.88	88.97

Table C.2: RD93 run statistics with pads installed.

	RD93 Data Statistics (Pads)											
	Characteristics			*Events*					*Rates & Averages*			
Run	Mom (GeV/c)	ID	Time (min)	#Tot Evts	#Phys Evts	#Puls Evts	#EoS Evts	#Unk Evts	Spls/ Min	Evts/ Min	Phys/ Spl
62	+1.0	*mb*	30.17	46627	44995	1152	476	2	15.78	1491.55	94.53
63	+1.5	*mb*	26.80	42079	40625	1028	423	2	15.78	1515.86	96.04
52	+4.0	*mb*	28.17	41086	39559	1080	443	2	15.73	1404.46	89.30
51	+4.0	μ^+	27.45	34909	33487	1003	412	5	15.01	1219.93	81.28
57	+4.0	μ^+	43.62	62536	60180	1665	683	6	15.66	1379.75	88.11
55	+4.0	π^+	32.10	20259	18539	1211	494	13	15.39	577.54	37.53
56	+4.0	π^+	45.62	70224	67759	1742	719	2	15.76	1485.40	94.24
54	+4.0	e^+	56.17	16387	13344	2155	886	1	15.77	237.58	15.06
53	+4.0	p^+	27.47	37227	35754	1037	421	13	15.33	1301.72	84.93
58	+8.0	*mb*	32.47	51938	50184	1239	511	2	15.74	1545.71	98.21
59	+8.0	*mb*	3.63	5728	5535	133	56	2	15.41	1523.39	98.84
60	+8.0	*mb*	46.30	71766	69254	1777	731	2	15.79	1495.77	94.74

Table C.3: RD94 run statistics with strips installed, positive beam.

RD94 Data Statistics (Strips, +Polarity)

Run	*Characteristics*			*Events*					*Rates & Averages*		
	Mom (GeV/c)	ID	Time (min)	#Tot Evts	#Phys Evts	#Puls Evts	#EoS Evts	#Unk Evts	Spls/ Min	Evts/ Min	Phys/ Spl
177	+1.0	*mb*	41.40	135004	118512	15255	1278	5	30.87	2862.61	92.73
178	+1.0	e^+	19.60	64465	56574	7286	614	2	31.33	2886.43	92.14
179	+1.0	p^+	24.17	59665	50688	8342	704	1	29.13	2097.43	72.00
149	+1.5	*mb*	46.38	115316	100306	13905	1161	5	25.03	2162.54	86.40
152	+1.5	π^+	00.00	60240	50567	8966	755	1	4.01	268.54	66.98
151	+1.5	e^+	26.03	56858	48309	7966	668	3	25.66	1855.66	72.32
150	+1.5	p^+	17.50	59515	52466	6506	549	1	31.37	2998.06	95.57
181	+2.0	*mb*	17.87	59449	52262	6648	559	1	31.29	2925.11	93.49
180	+2.0	μ^+	33.92	61770	49769	11101	940	1	27.71	1467.39	52.95
182	+2.0	π^+	16.30	57057	50505	6049	507	2	31.10	3098.47	99.62
185	+2.0	e^+	10.27	25762	21641	3805	315	2	30.68	2107.89	68.70
183	+2.0	p^+	29.45	62075	50541	10665	895	3	30.39	1716.16	56.47
205	+3.0	*mb*	19.45	67374	59516	7242	608	2	31.26	3059.95	97.89
208	+3.0	μ^+	25.83	63094	52618	9653	808	4	31.28	2036.83	65.12
207	+3.0	π^+	18.63	58164	50861	6750	560	6	30.05	2729.57	90.82
209	+3.0	e^+	27.37	65324	54249	10222	859	3	31.39	1982.30	63.15
206	+3.0	p^+	18.15	62125	54816	6747	568	1	31.29	3020.17	96.51
164	+4.0	*mb*	11.38	39359	34771	4229	354	2	31.10	3054.55	98.22
171	+4.0	μ^+	19.48	60621	52753	7249	604	4	31.00	2707.60	87.34
172	+4.0	μ^+	21.23	67116	58534	7913	667	1	31.41	2756.70	87.76
170	+4.0	π^+	17.50	57027	50241	6263	527	1	30.11	2870.91	95.33
176	+4.0	e^+	39.33	65894	50248	14432	1210	5	30.76	1277.49	41.53
169	+4.0	p^+	16.83	56541	49992	6039	512	0	30.42	2969.82	97.64
186	+5.0	*mb*	20.68	60289	52196	7500	632	2	30.56	2523.58	82.59
190	+5.0	μ^+	34.00	65995	52451	12539	1052	3	30.94	1542.68	49.86
188	+5.0	π^+	17.50	60019	52974	6492	547	2	31.26	3027.09	96.84
192	+5.0	e^+	52.07	58752	37700	19460	1636	6	31.42	724.07	23.04
187	+5.0	p^+	19.77	68393	60417	7353	617	2	31.21	3056.51	97.92
159	+6.0	*mb*	16.47	57593	50942	6129	517	0	31.40	3093.64	98.53
162	+6.0	μ^+	38.83	65736	49973	14532	1228	3	31.62	1286.86	40.69
160	+6.0	π^+	15.87	56471	50076	5894	496	1	31.26	3156.05	100.96
163	+6.0	e^+	38.53	66100	50462	14421	1212	3	31.45	1309.57	41.64
161	+6.0	p^+	16.60	58480	51782	6177	520	1	31.33	3119.40	99.58
193	+7.0	*mb*	18.02	58120	50884	6690	560	3	31.08	2824.27	90.86
195	+7.0	μ^+	37.07	68518	53521	13844	1159	5	31.27	1443.91	46.18
196	+7.0	μ^+	37.50	72041	56870	13999	1176	5	31.36	1516.53	48.36
194	+7.0	π^+	21.80	73604	64813	8120	677	4	31.06	2973.07	95.74
198	+7.0	e^+	33.65	27850	14256	12568	1063	2	31.59	423.66	13.41
197	+7.0	p^+	17.97	58041	50837	6665	560	2	31.17	2829.52	90.78
199	+8.0	*mb*	13.10	43169	37919	4849	408	0	31.15	2894.58	92.94
201	+8.0	μ^+	32.48	65106	51953	12139	1016	5	31.28	1599.37	51.13
200	+8.0	π^+	18.65	64755	57248	6918	578	4	30.99	3069.60	99.04
203	+8.0	e^+	51.93	30469	9425	19435	1629	7	31.37	181.48	5.79
202	+8.0	p^+	20.48	59490	51299	7605	646	0	31.54	2504.43	79.41
154	+9.0	*mb*	18.42	61905	54492	6842	574	2	31.17	2958.84	94.93
157	+9.0	μ^+	25.92	60788	50294	9674	817	1	31.52	1940.60	61.56
156	+9.0	π^+	16.28	57066	50497	6053	595	4	31.01	3101.15	99.99
155	+9.0	e^+	6.13	2474	30	2293	192	1	31.30	4.89	0.16
158	+9.0	p^+	17.82	61838	54639	6634	557	2	31.26	3066.74	98.10

Table C.4: RD94 run statistics with strips installed, negative beam.

RD94 Data Statistics (Strips, −Polarity)

	Characteristics			*Events*					*Rates & Averages*		
Run	Mom (GeV/c)	ID	Time (min)	#Tot Evts	#Phys Evts	#Puls Evts	#EoS Evts	#Unk Evts	Spls/ Min	Evts/ Min	Phys/ Spl
145	−1.5	mb	10.08	32910	29105	3509	296	0	29.36	2886.45	98.33
146	−1.5	e^-	15.62	26935	20731	5808	490	1	31.38	1327.49	42.31
147	−1.5	e^-	19.92	57885	49902	7400	621	2	31.18	2505.54	80.36
219	−2.0	mb	34.87	113756	99697	12960	1094	3	31.38	2859.38	91.13
222	−2.0	μ^-	36.67	116649	101859	13631	1148	3	31.31	2777.97	88.73
220	−2.0	π^-	38.83	115553	99870	14458	1219	4	31.39	2571.76	81.93
221	−2.0	e^-	36.47	118840	104118	13582	1142	5	31.32	2855.16	91.17
210	−3.0	mb	29.22	101009	89204	10890	913	3	31.25	3053.19	97.70
212	−3.0	μ^-	25.73	61197	50806	9609	803	4	31.20	1974.33	63.27
211	−3.0	π^-	18.43	57818	50642	6632	561	1	30.43	2747.31	90.27
213	−3.0	e^-	22.95	61413	52130	8566	723	1	31.50	2271.46	72.10
228	−5.0	μ^-	16.10	25832	19788	5588	477	1	29.63	1229.07	41.48
229	−5.0	μ^-	14.75	25961	20038	5467	466	0	31.59	1358.51	43.00
230	−5.0	μ^-	14.03	25568	19904	5221	440	1	31.35	1418.34	45.24
215	−7.0	mb	33.27	113257	99823	12402	1039	5	31.23	3000.69	96.08
217	−7.0	μ^-	47.08	67903	50262	16335	1377	2	29.25	1067.51	36.50
218	−7.0	μ^-	66.68	20348	12012	7748	656	1	9.84	180.13	18.31
223	−7.0	μ^-	31.83	104225	91361	11860	993	5	31.19	2869.98	92.01
216	−7.0	π^-	36.68	114452	99644	13686	1154	2	31.46	2716.33	86.35
214	−7.0	e^-	50.58	120181	99731	18906	1584	7	31.31	1971.62	62.96
224	−9.0	mb	32.98	112980	99852	12101	1016	4	30.80	3027.35	98.28
225	−9.0	μ^-	17.53	57259	50192	6514	550	0	31.37	2862.66	91.26
226	−9.0	π^-	17.25	59908	52971	6391	541	0	31.36	3070.78	97.91
227	−9.0	e^-	30.47	31423	19394	11100	935	3	30.69	636.56	20.74

Table C.5: RD94 run statistics with pads installed, positive beam.

RD94 Data Statistics (Pads, +Polarity)

	Characteristics			*Events*					*Rates & Averages*		
Run	Mom (GeV/c)	ID	Time (min)	#Tot Evts	#Phys Evts	#Puls Evts	#EoS Evts	#Unk Evts	Spls/ Min	Evts/ Min	Phys/ Spl
119	+1.0	*mb*	18.57	57845	50589	6710	566	1	30.48	2724.72	89.38
120	+1.0	e^+	22.07	58501	50244	7666	645	1	29.23	2276.92	77.90
101	+1.5	*mb*	25.13	60259	49992	9554	764	7	30.40	1989.07	65.43
143	+1.5	*mb*	19.23	61684	54028	7077	600	1	31.20	2809.08	90.05
144	+1.5	π^+	29.15	60600	50517	9339	791	0	27.14	1733.00	63.86
122	+2.0	*mb*	19.13	57761	50253	6958	589	0	30.78	2626.46	85.32
121	+2.0	μ^+	26.22	60303	50231	9325	780	4	29.75	1915.99	64.40
125	+2.0	π^+	11.85	33962	29227	4398	371	0	31.31	2466.41	78.78
126	+2.0	π^+	8.27	26418	23352	2825	242	0	29.27	2824.84	96.50
123	+2.0	e^+	38.35	68938	53829	14026	1180	4	30.77	1403.62	45.62
124	+2.0	p^+	22.78	59824	50732	8424	714	1	31.34	2226.72	71.05
139	+3.0	*mb*	21.58	60278	52101	7584	638	2	29.56	2413.95	81.66
142	+3.0	μ^+	18.38	38139	30710	6853	576	1	31.33	1670.53	53.32
141	+3.0	π^+	19.88	69635	61612	7397	618	3	31.08	3098.68	99.70
140	+3.0	p^+	19.88	58861	50857	7405	626	1	31.48	2557.77	81.24
95	+4.0	*mb*	20.05	58296	49979	7742	625	2	31.17	2492.72	79.97
97	+4.0	μ^+	25.75	61428	51037	9650	780	3	30.29	1982.02	65.43
96	+4.0	π^+	17.73	57595	50201	6855	554	2	31.24	2830.88	90.62
98	+4.0	e^+	39.52	38678	22050	15382	1240	4	31.38	557.99	17.78
100	+4.0	p^+	16.62	49529	42656	6388	516	3	31.05	2567.06	82.67
93	+6.0	*mb*	19.62	59515	51308	7603	614	1	31.30	2615.53	83.56
127	+6.0	*mb*	17.47	58975	51934	6495	546	1	31.26	2973.32	95.12
129	+6.0	μ^+	31.35	61691	49985	10801	900	6	28.71	1594.42	55.54
130	+6.0	π^+	20.68	64995	56978	7417	626	1	30.27	2754.78	91.02
128	+6.0	e^+	56.32	53818	40252	12593	1059	3	18.80	714.74	38.01
92	+6.0	p^+	18.12	59533	51977	7006	564	4	31.13	2869.02	92.16

Table C.6: RD94 run statistics with pads installed, negative beam.

RD94 Data Statistics (Pads, −Polarity)											
	Characteristics			*Events*					*Rates & Averages*		
Run	Mom (GeV/c)	ID	Time (min)	#Tot Evts	#Phys Evts	#Puls Evts	#EoS Evts	#Unk Evts	Spls/ Min	Evts/ Min	Phys/ Spl
115	−1.0	*mb*	20.35	58367	51422	6405	542	2	26.63	2526.88	94.87
116	−1.0	e^-	17.08	57917	51026	6359	532	4	31.14	2986.89	95.91
87	−1.5	*mb*	7.05	24205	21711	2278	219	0	31.06	3079.57	99.14
103	−1.5	*mb*	17.18	56089	49178	6385	536	2	31.19	2861.96	91.75
105	−1.5	π^-	23.47	59553	52340	6660	555	2	23.65	2230.40	94.31
104	−1.5	e^-	17.00	59924	53064	6327	523	5	30.76	3121.41	101.46
111	−2.0	*mb*	16.32	56836	50256	6065	512	0	31.38	3080.04	98.16
114	−2.0	μ^-	17.13	56833	49944	6360	534	2	31.17	2915.02	93.53
113	−2.0	π^-	24.03	57334	50102	6689	560	2	23.30	2084.69	89.47
112	−2.0	e^-	15.80	57216	50830	5890	493	1	31.20	3217.09	103.10
135	−3.0	*mb*	25.35	63328	54040	8631	733	0	28.92	2131.76	73.72
138	−3.0	μ^-	44.40	78928	61550	16146	1356	4	30.54	1386.26	45.39
137	−3.0	π^-	19.85	59597	51634	7380	624	2	31.44	2601.21	82.75
136	−3.0	e^-	43.08	35340	19660	14594	1225	5	28.43	456.32	16.05
83	−4.0	*mb*	6.67	20290	17942	2151	205	1	30.75	2691.30	87.52
85	−4.0	μ^-	5.62	20339	18314	1846	176	1	31.34	3260.65	104.06
86	−4.0	μ^-	8.42	23094	20097	2733	264	0	31.37	2387.76	76.13
109	−4.0	μ^-	17.10	59343	52499	6302	536	1	31.35	3070.12	97.95
108	−4.0	π^-	21.55	29219	20468	8076	677	2	31.42	949.79	30.23
107	−4.0	e^-	19.18	60277	52985	6736	562	4	29.30	2762.03	94.28
88	−6.0	*mb*	19.95	68833	60489	7719	620	4	31.08	3032.03	97.56
90	−6.0	μ^-	21.78	62798	53651	8455	678	4	31.12	2462.94	79.13
89	−6.0	π^-	16.80	57450	50439	6486	523	2	31.13	3002.32	96.44
91	−6.0	e^-	13.88	27004	21196	5370	431	2	31.04	1526.72	49.18
79	−8.0	*mb*	31.98	106784	95309	10488	1002	2	31.33	2979.96	95.12
80	−8.0	*mb*	6.35	19995	17758	2046	193	2	30.39	2796.54	92.01
81	−8.0	μ^-	8.23	21814	18880	2673	254	2	30.85	2293.12	74.33
82	−8.0	μ^-	14.50	26408	21263	4772	454	3	31.31	1466.41	46.83
131	−9.0	*mb*	17.65	59077	51969	6557	550	2	31.16	2944.42	94.49
134	−9.0	μ^-	30.17	62038	49864	11256	945	3	31.33	1652.95	52.77
133	−9.0	π^-	20.63	58942	50666	7675	642	4	31.11	2455.54	78.92
[illegible]	[illegible]	[illegible]	[illegible]	[illegible]	[illegible]	[illegible]	[illegible]	[illegible]	[illegible]	[illegible]	[illegible]

Appendix D

Detailed Trigger Schematics

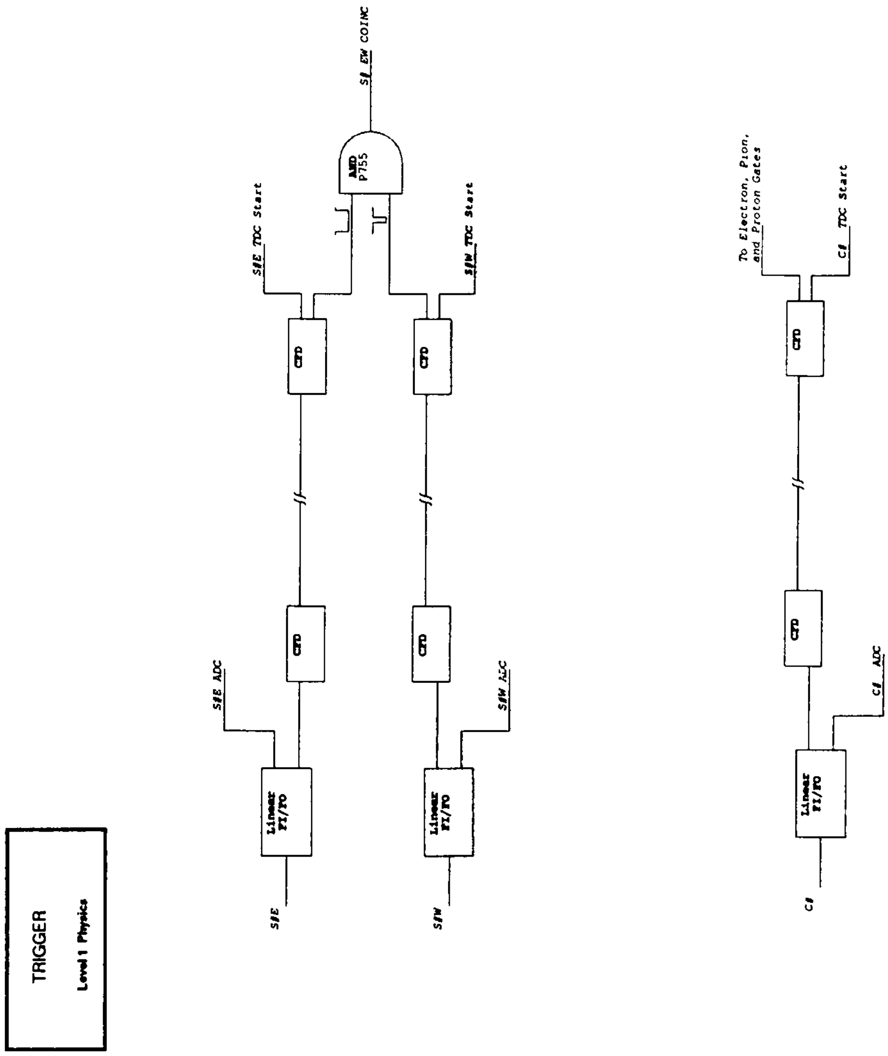

Figure D-1: Detailed Schematic of the Level 1 Physics Circuits.

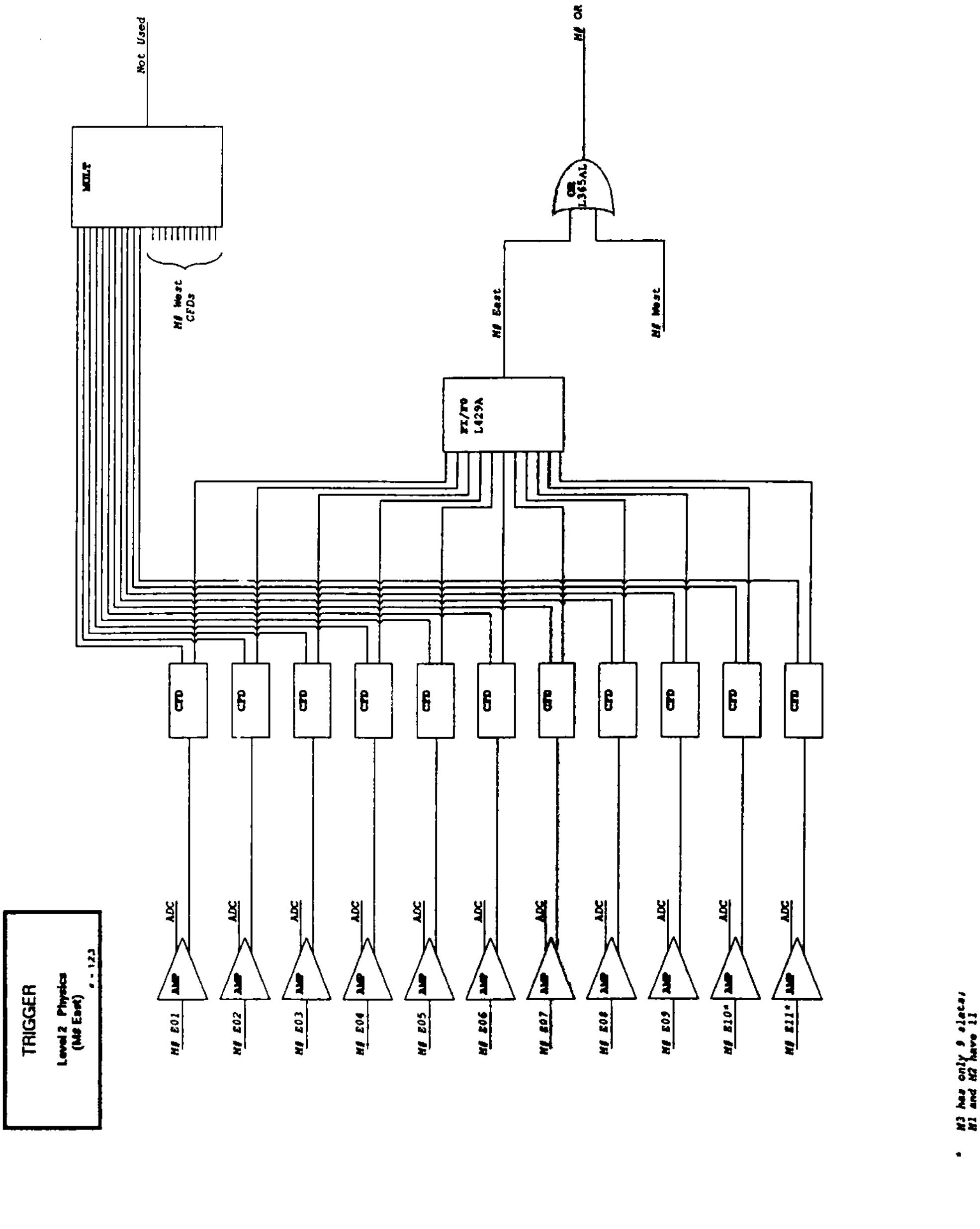

Figure D-2: Detailed Schematic of the Level 2 Physics Circuits.

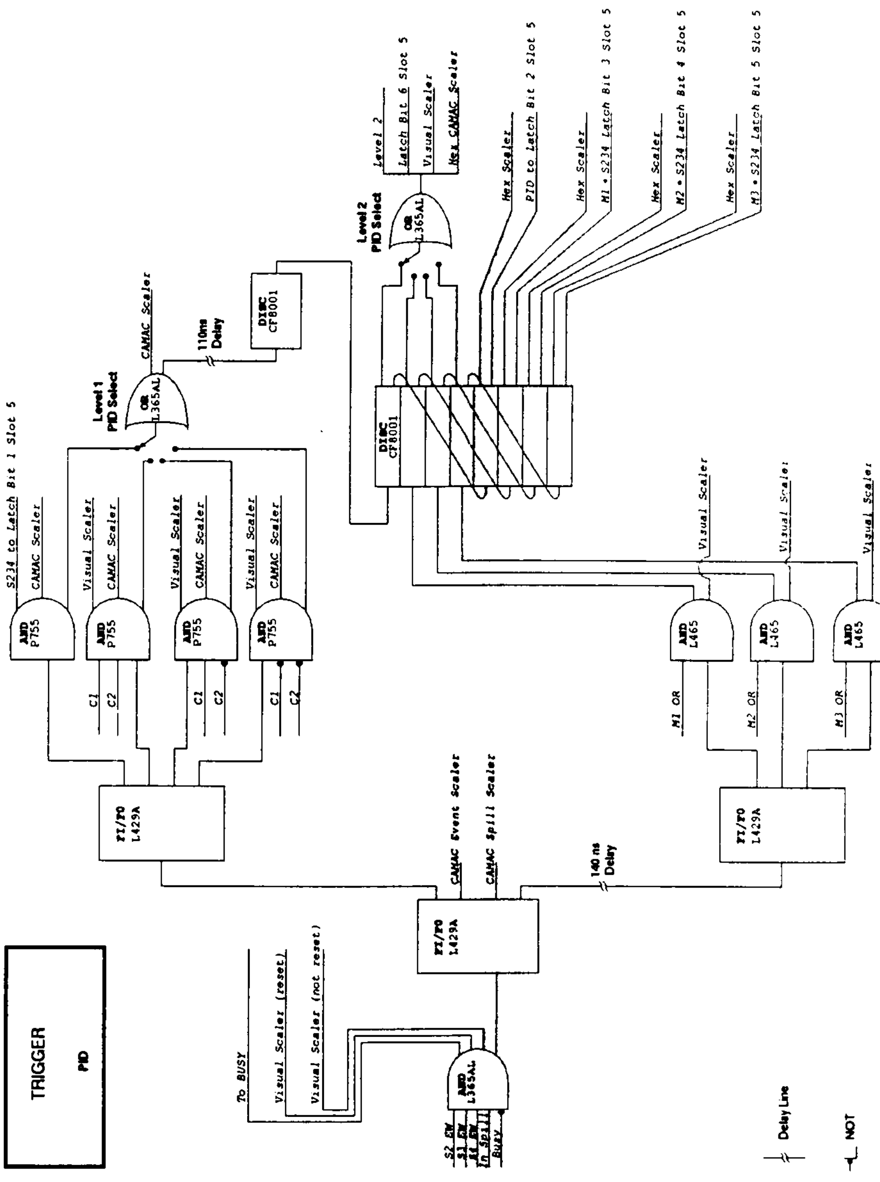

Figure D-3: Detailed Schematic of the Particle ID Circuits.

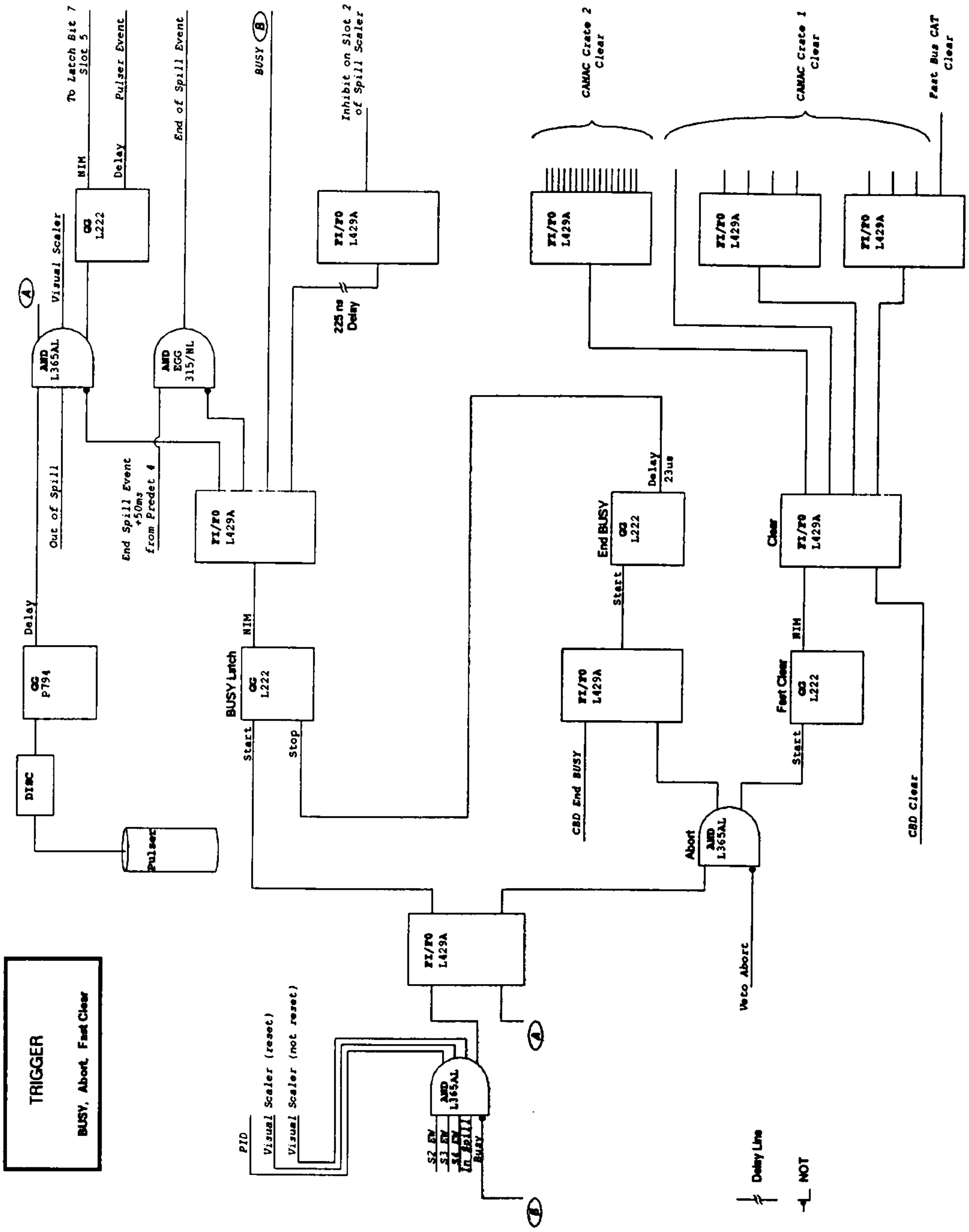

Figure D-4: Detailed Schematic of the BUSY, Abort and Clear Circuits.

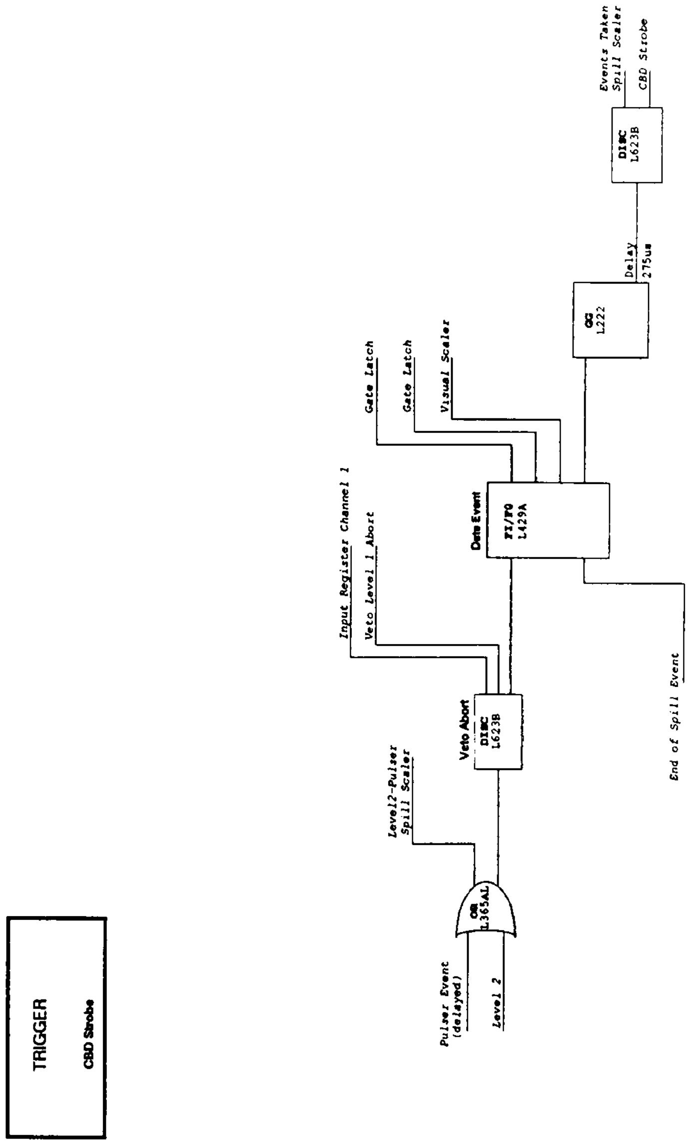

Figure D-5: Detailed Schematic of the CBD Strobe Circuit.

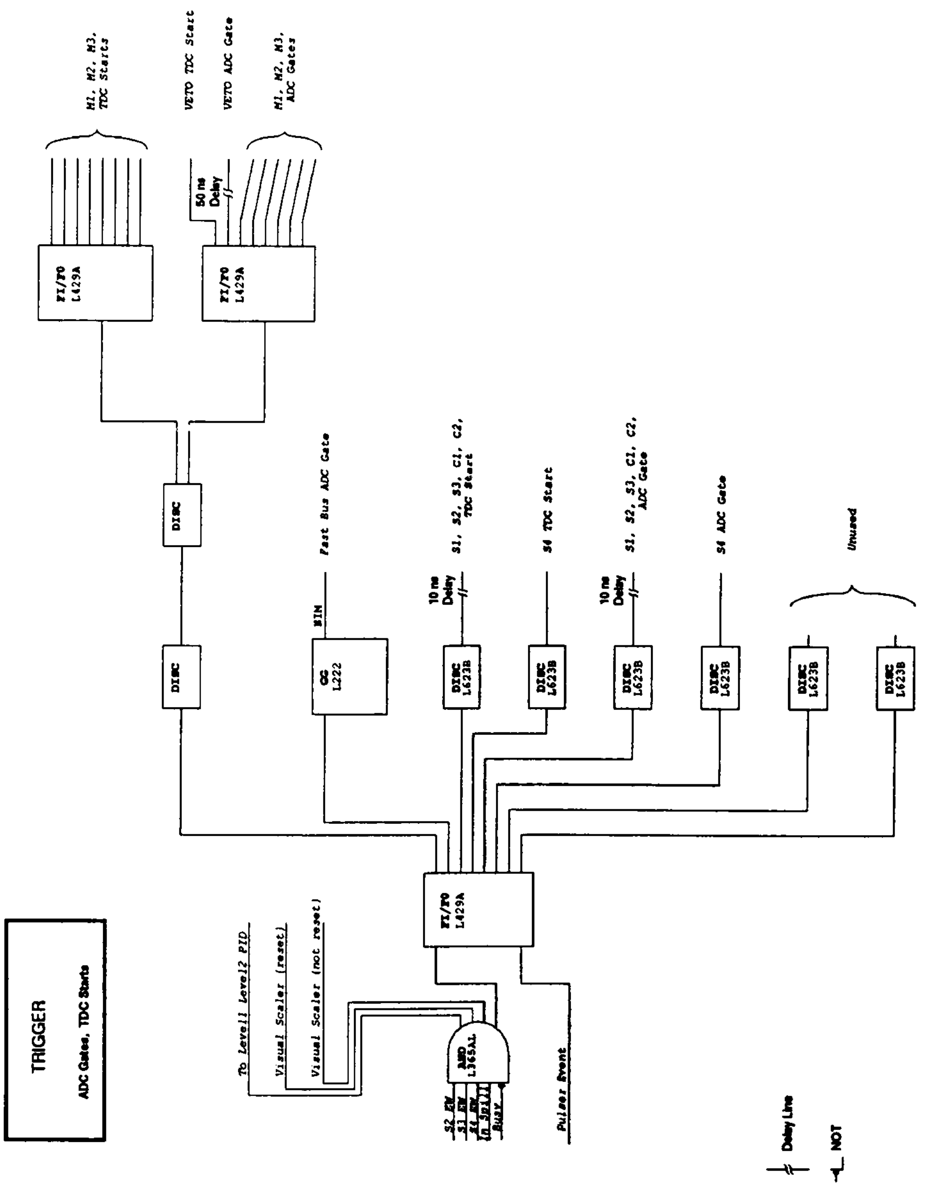

Figure D-6: Detailed Schematic of the ADC gate and TDC start Circuits.

Vita

Joseph G. Kreke was born on July 26, 1959 in Pittsburgh, Pennsylvania. In February, 1979, Joseph enlisted in the U.S. Navy and after two years of Navy schools, including Naval Nuclear Power School, he became a crew member of the USS Richard B. Russell (SSN-687) Fast Attack Submarine and served as an electrician, an electrical operator and shutdown reactor operator for four years.

After leaving the Navy in December, 1984, Joseph attended college at Duquesne University in Pittsburgh and earned a Bachelor of Science Degree in May, 1988, in Physics with a minor in Chemistry, graduating with honors. Joseph gave talks at the Eastern Colleges Science Conference for three consecutive years on Quadrupole Mass Spectrometers and Acoustical Separation of Gases. Joseph was selected as a Ambassador of the University's President, served on University's Computer Committee and was selected as a Student Advisor to the Dean of Liberal Arts.

After graduation from Duquesne University, Joseph attended graduate school at the University of Tennessee, Knoxville where he continued his studies in physics and specialized in the area of Experimental Relativistic Heavy Ion Collisions. Joseph worked at Conseil Europeen pour la Recherche Nucleaire (CERN) in Geneva, Switzerland for several weeks and participated in the WA80 Experiment there. Joseph's thesis experiment was a study of muon-pion separation in the 1-9GeV/c momentum range using sampling calorimeter technology coupled with discriminant analysis. This was primarily a research and development project conducted at Brookhaven National Laboratory for the PHENIX Experiment. Its goal was to define optimum dimensions and minimum segmentations to aid in the design of the PHENIX Muon Identifier at the Relativistic Heavy Ion Collider.